



Subsonic High - Angle - Of - Attack Aerodynamic Characteristics of a Cone and Cyclinder with Triangular Cross Sections and a Cone with a Square Cross Section

Mark H. Clarkson, Gerald N. Malcolm,
Victoria A. Brittain and Paul A. Intemann

(NASA-TM-84377) SUBSONIC
HIGH-ANGLE-OF-ATTACK AERODYNAMIC
CHARACTERISTICS OF A CONE AND CYLINDER WITH
TRIANGULAR CROSS SECTIONS AND A CONE WITH A
SQUARE CROSS SECTION (NASA) 78 p

N84-10019

Unclass
G3/02 42255

August 1983



National Aeronautics and
Space Administration

Subsonic High - Angle - Of - Attack Aerodynamic Characteristics of a Cone and Cyclinder with Triangular Cross Sections and a Cone with a Square Cross Section

Mark H. Clarkson, University of Florida, Gainesville, Florida

Gerald N. Malcolm, NASA Ames Research Center, Moffett Field, California

Victoria A. Brittain and Paul A. Intemann, University of Florida, Gainesville, Florida



National Aeronautics and
Space Administration

Ames Research Center
Moffett Field, California 94035

TABLE OF CONTENTS

	<u>Page</u>
NOMENCLATURE	v
SUMMARY	1
1. INTRODUCTION	1
2. DESCRIPTION OF EXPERIMENTS	3
Test Facility	3
Description of Models	3
Axes and Angular Settings	3
Run Schedules	4
Pressure-Tap Numbering System	4
3. DATA REDUCTION	4
4. DATA PLOTS	5
5. DISCUSSION OF FORCE DATA	5
Square Cross Section	6
Triangular Cross Section	7
6. PRESSURE-DISTRIBUTION PLOTS	7
Models with Square Cross Sections: $\beta = \psi = 0$	7
Models with Square Cross Sections: $\psi = 10^\circ$	8
Models with Triangular Cross Section: $\beta = \psi = 0$	8
Models with Triangular Cross Sections: $\psi = 10^\circ$	9
7. INVERTED TRIANGULAR CYLINDER	9
8. FLOW VISUALIZATION	10
Sublimation Tests	10
Oil-Flow Tests	10
9. CONCLUSIONS	11
REFERENCES	12
TABLES	13
FIGURES	25

PRECEDING PAGE BLANK NOT FILMED

NOMENCLATURE

A_b	base area (see table 5)
A_y	area of the projection of the body onto the x-z plane (see table 5)
A_z	area of the projection of the body onto the x-y plane (see table 5)
C_p	pressure coefficient = $(p_s - p)/q$
C_y	Y/qA_b (same as CY)
\bar{C}_y	total side-force coefficient = Y/qA_y
\hat{C}_y	section side-force coefficient from pressure measurements ($W/h \times ICPY$)
\bar{C}_z	total normal-force coefficient = Z/qA_z
h	height of body in Z-direction at general station along the body x-axis
h_b	height of body at the base
h_j	height of body in z-direction at station $j = 1, 2, \text{ or } 3$
L	length of body used in defining moment coefficients (see table 5)
M	Mach number
P	free-stream static pressure
P_s	local static pressure
q	free-stream dynamic pressure (same as Q)
R_{hb}	Reynolds number = $U_\infty h_b / \nu$
R_{hj}	local Reynolds number = $U_\infty h_j / \nu$, $j = 1, 2, \text{ or } 3$
s	arc length measured from tap 01 around a given cross section
s_o	total arc length around a given section
U_∞	magnitude of the free-stream velocity vector (same as V)
u, v, w	velocity components along the x, y, and z body axes
W_j	maximum width of section at station $j = 1, 2, \text{ or } 3$
X, Y, Z	components of the force vector in the x, y, and z directions

x,y,z	body axes (see fig. 6)
\hat{z}	distance measured in the negative z-direction from the bottom of a section
α	angle of attack = $\tan^{-1}(w/u)$ (see fig. 7)
β	angle of sideslip = $\sin^{-1}(v/U)$ (see fig. 7)
θ	angle between normal to surface and centerline of section
ν	kinematic viscosity
σ	total angle of attack = angle between \vec{U}_∞ and the body x-axis = $\cos^{-1}(u/U_\infty)$ (see fig. 7)
ψ	roll angle about the body x-axis = $\tan^{-1}(v/w)$ (see fig. 7)

Computer printout symbols:

CON	configuration
CRM,CPM,CYM	moment coefficient about the x, y, and z axes, respectively = moment/ $qA_b L$
CX,CY,CZ	force coefficients in the x, y, and z directions = force/ qA_b
ICPY-1,ICPY-2,ICPY-3	section force coefficient in the y-direction (side force) determined from integration of pressures = (force in y-direction/unit length) $_j/qW_j$
ICPZ-1,ICPZ-2,ICPZ-3	section force coefficient in the z-direction determined from integration of pressures = (force in z-direction/unit length) $_j/qW_j$ (the negative of the usual normal-force coefficient)
PS	tunnel static pressure, lb/ft ²
PSI	roll angle = ψ
PT	tunnel total pressure, lb/ft ²
Q	tunnel dynamic pressure, lb/ft ²
RENO	unit Reynolds number (per foot)
SEQ	sequence
TSF	tunnel static temperature, °F
TTF	tunnel total temperature, °F
V	tunnel speed, ft/sec

SUBSONIC HIGH-ANGLE-OF-ATTACK AERODYNAMIC CHARACTERISTICS OF A CONE AND CYLINDER

WITH TRIANGULAR CROSS SECTIONS AND A CONE WITH A SQUARE CROSS SECTION

Mark H. Clarkson,* Gerald N. Malcolm, Victoria A. Brittain,* and Paul A. Intemann*

NASA Ames Research Center

SUMMARY

Experiments were conducted in the 12-Foot Pressure Wind Tunnel at Ames Research Center on three models with noncircular cross sections: a cone having a square cross section with rounded corners and a cone and cylinder with triangular cross sections and rounded vertices. The cones were tested with both sharp and blunt noses. Surface pressures and force and moment measurements were obtained over an angle of attack range from 30° to 90° , and selected oil-flow experiments were conducted to visualize surface flow patterns. Unit Reynolds numbers ranged from $0.8 \times 10^6 \text{ m}^{-1}$ to $13.0 \times 10^6 \text{ m}^{-1}$ at a Mach number of 0.25, except for a few low-Reynolds-number runs at a Mach number of 0.17. Pressure data, as well as force data and oil-flow photographs, reveal that the three-dimensional flow structure at angles of attack up to 75° is very complex and is highly dependent on nose bluntness and Reynolds number. For angles of attack from 75° to 90° the sectional aerodynamic characteristics are similar to those of a two-dimensional cylinder with the same cross section.

1. INTRODUCTION

Continual extension of the flight envelopes of fighter aircraft and missiles in efforts to achieve increased maneuverability results in a sustained interest in high-angle-of-attack aerodynamics. The aerodynamic characteristics of the forebody are important determinants of the flight behavior of such vehicles.

Forebodies with circular cross sections have been studied extensively, especially with regard to the flow phenomena of asymmetric lee-side vortices and the resulting side forces and yawing moments. But noncircular cross sections, although they are used frequently in practice, have not been so broadly investigated. This is particularly true for angles of attack above 45° .

The two-dimensional aerodynamic characteristics of a number of noncircular cylinders have been investigated by Polhamus (ref. 1) and Polhamus et al. (ref. 2) at subsonic speeds over a range of Reynolds numbers. Hasel and Kouyoumjian (ref. 3) measured static pressures and boundary-layer profiles on a series of ogive-cylinder models having noncircular cross sections. The latter tests were all conducted at a Mach number of 2.01 and a Reynolds number of 1.25×10^6 . The angle-of-attack range was -15° to $+15^\circ$, all at zero sideslip. The models tested included both triangular and square cross sections with rounded corners.

Aerodynamic measurements have been made in both static and rotary-balance tests (refs. 4 and 5) in the 12-Foot Pressure Wind Tunnel at Ames Research Center on a

*University of Florida, Gainesville, Florida.

cylindrical model with a square cross section having rounded corners and a blunt nose. This configuration is highly sensitive to Reynolds number, as was observed in the experiments of Polhamus. In particular, when used as a forebody on a rotary-balance model in the Ames 12-Foot Pressure Wind Tunnel (ref. 4), it was shown to produce strong pro-spin moments at low Reynolds numbers and strong antispin moments at high Reynolds numbers at attitudes near 90° . The expectation that the moment at angles of attack of 45° and 60° would be similar to that of $\sigma = 90^\circ$ at lower Reynolds numbers, that is, be pro-spin, was not fulfilled, however. Further investigation (ref. 5) revealed that the net effect of angle of attack was to alter drastically the flow separation behavior at Reynolds numbers well below the critical Reynolds number of 800,000 at $\sigma = 90^\circ$ (where the cross force changed sign). A part of this behavior was attributed to the role of inflexional instabilities (ref. 5) in the laminar boundary layer in promoting transition to turbulent flow in the range $400,000 < R_{hb} < 800,000$. An explanation for the strong negative cross-force coefficient (corresponding to antispin behavior) at $R_{hb} < 400,000$ was given based on a postulated role of the lee vortices.

The present series of tests was designed to determine whether the ideas advanced in reference 5 concerning the role of boundary-layer instability and transition in determining the patterns of flow separation could be applied to more complex shapes. Tests were conducted in the 12-Foot Pressure Wind Tunnel on three basic models. The configurations consisted of a cone with a square cross section and a cylinder and cone with triangular cross sections. The cone models were tested with both sharp and blunt noses.

The cones were selected because they had small axial pressure gradients in potential flow at all total angles of attack σ , and, in particular, so that the influence of variations in local Reynolds number could be readily determined at σ 's near 90° .

Blunt noses were provided for the cones so that the effect of strong axial pressure gradients in this region on the entire flow field could be investigated, and to see if blunting the nose had the same effect of reducing or delaying asymmetries in the flow as had been noted on bodies with circular cross sections.

The triangular cross section was selected because Polhamus (ref. 1) had shown that this section had a negative side force for $R_{hb} < 450,000$ and a positive side force for $R_{hb} > 450,000$; these findings are opposite to those obtained from models with square cross sections, for which the side force changed sign from positive to negative as R_{hb} was increased through 500,000.

Only a portion of the available data has been selected for discussion and plotting in this report. A more comprehensive analysis of the results on the triangular cone is presented in reference 6. Tabulated data are obtainable from Gerald Malcolm at Ames Research Center.

2. DESCRIPTION OF EXPERIMENTS

Test Facility

The experiments were conducted in the 12-Foot Pressure Wind Tunnel at Ames Research Center. This is a variable-pressure, low-turbulence facility with a Mach number capability up to $M = 0.98$ and a maximum unit Reynolds number capability of $29.5 \times 10^6 \text{ m}^{-1}$ at $M = 0.25$. Force and pressure measurements were acquired over a range of free-stream unit Reynolds numbers from $2.6 \times 10^6 \text{ m}^{-1}$ to $13.1 \times 10^6 \text{ m}^{-1}$ at $M = 0.25$. Tests at a unit Reynolds number of $0.8 \times 10^6 \text{ m}^{-1}$ were also run but at $M = 0.17$.

The models were mounted on the Northrop turret support system, as shown in figure 1, with a bent sting installed. A bent sting was used in the angle of attack range 0° to 45° and a straight sting in the range 40° to 90° . The support system could be yawed through an angle of $\pm 90^\circ$ and pitched through a positive range of 45° .

Description of Models

Three basic models were constructed, the principal dimensions of which are shown in figure 2. The geometric details of the triangular cross section are given in non-dimensional form in figure 3.

The nose of the cylinder model is defined by elliptic arcs faired into generators of the cylinder at points 17.78 cm (7 in.) from the tip of the nose as shown, schematically, in figure 4(a).

Two nose sections were available for the cone models, either sharp or blunt. The sharp nose (the forward 40.64 cm (16 in.) of each cone) could be removed and replaced with a 5.08-cm-long blunt nose. Each of these blunt noses was faired into the corresponding main body, using elliptic arcs tangent to the cone generators, as shown in figure 4(b).

The main body of each model was constructed from a single, forged aluminum billet to provide a smooth surface with no mating part lines or screw heads. Each nose was also constructed from a single piece of aluminum. The final external machining was done on a numerically controlled mill and hand finished to a surface variation within 15 to 30 μm .

Each model was provided with 46 pressure taps at each of three axial locations. The axial locations are shown in figure 2, and the circumferential locations are shown in figure 5. Each tap was connected by flexible plastic tubing to one of three 48-port Scanivalves located in the base of the model. The tap orifices were 0.020 in. in diameter.

A 2-in., TASK MARK III-C, six-component force and moment balance was used for all the tests.

Axes and Angular Settings

Body axes have been used throughout; they are defined in figure 6. Note that the origin is located at 40.64 cm (16 in.) from the base of each model. When the

triangular cylinder was tested inverted, it was regarded as another model with the y-z axes rotated 180° about the x-axis from the position shown in figure 6.

With the exception of a few α -sweeps ($\beta = 0$) and β -sweeps (α fixed), the model attitude was defined by the total angle of attack σ and the roll angle ψ . These four angles (α , β , σ , ψ) and the relations between them are defined in figure 7. Note that σ is the angle between the free-stream velocity vector and the body x-axis and that ψ is the roll angle about the body x-axis, clockwise rotation, looking forward, being positive.

Run Schedules

Model configurations were given a numerical designation; these designations are shown in table 1. Data were taken for runs 4 through 279, and these are summarized by Reynolds number and configuration number in table 2. A run summary for flow-visualization tests is given in table 3.

A run schedule showing the configuration number, sequence numbers, tunnel test conditions, and roll angle (PSI) is given in table 4. In general, a sequence number was assigned to each combination of angular settings of the model. In particular, sequence numbers 1, 2, 3, and 4 designate total angles of attack of 45°, 60°, 75°, and 90°, respectively, when the straight sting was being used.

The abbreviations and symbols used on the computer printouts are listed separately in the nomenclature at the beginning of the report.

Pressure-Tap Numbering System

A three-digit number was assigned to each pressure tap on a given model. The first digit on the left of the tap number designated the station. The next two digits denoted the circumferential tap number, starting with 01, bottom centerline, and numbering consecutively, in a clockwise direction looking forward, to tap 46 (see fig. 5 for the two-digit, circumferential tap numbers). For example, the number 224 designated the top tap of each model at station 2.

3. DATA REDUCTION

The force and moment coefficients are referenced to the base area A_b and model length L , respectively (see nomenclature). The moment center is located at the model base. The section side-force coefficient at a given station was found by numerical integration of the following line integral:

$$ICPY_- = - \int_0^{s_0/W} (C_p \sin \theta) d(s/W)$$

where θ is the angle between the normal to the surface and the centerline of the section (see fig. 3). The normal force was found in a similar manner from

$$ICPZ_- = - \int_0^{s_0/W} (C_p \cos \theta) d(s/W)$$

In the above integrals, C_p and θ are functions of s/W . In the pressure distribution plots, which are discussed in section 6, \hat{C}_y is used. For the triangular cross section $\hat{C}_y = h/w$ $ICPY_- = 1.21875$ $ICPY$ (see fig. 3).

To facilitate analysis of the data, two additional force coefficients are used, namely, \bar{C}_y and \bar{C}_z . These are defined in terms of projected side areas and plan view areas so that if the section coefficients were constant at each station $\bar{C}_y = \hat{C}_y = ICPY$ and $\bar{C}_z = ICPZ$. Area ratios for converting from one system to the other are given in table 5.

4. DATA PLOTS

A limited number of cross plots of normal-force and cross-force coefficients have been prepared; they are discussed in the next section.

A number of pressure-distribution plots have also been prepared. In most of them, the emphasis is on the side force produced under various conditions and, hence, C_p 's have been plotted versus z/h so that the sources of the contributions to the side force may be readily seen. The area between the port and starboard curves in a particular plot is proportional to the local side-force coefficient \hat{C}_y . A few plots are included in which C_p has been plotted against nondimensionalized arc length s/s_0 . The values of z/h and s/s_0 for each tap are given in table 6 for the square cross section and in table 7 for the triangular cross section. A brief discussion of these plots is given in section 6.

5. DISCUSSION OF FORCE DATA

The aerodynamic characteristics of bodies at high angles of attack are largely determined by flow separation characteristics. The flow can be divided into two basic regimes: one in which the wake is unsteady and, therefore, where the impulsive flow analogy does not apply, even qualitatively; and a second in which the wake is reasonably steady and the impulsive flow analogy seems to apply, at least in a qualitative sense. For the present test, the first regime extends from $\sigma = 90^\circ$ to just below 75° .

(The impulsive flow analogy (ref. 7) states that there exists a certain analogy between the crossflow at various stations along the body and the development with time of the flow about a cylinder starting from rest. Thus, the flow in the cross plane for the more forward sections should contain a symmetric pair of vortices on the lee side. These vortices should increase in strength with axial distance and, eventually, if the body is long enough, should discharge to form a vortex street as viewed in the moving cross plane. Viewed with respect to the stationary body the shed vortices would appear to be fixed.)

A qualitative explanation of the behavior at $\sigma = 90^\circ$ of the two cross sections tested is shown in figure 8 (and discussed in ref. 5). For the square cross section below a critical Reynolds number, the flow remains attached to the windward corner

and separates from the lee corner, and at Reynolds numbers above critical, the flow remains attached to the lee corner sufficiently long to change the side-force coefficient from positive to negative. The definition of critical Reynolds number is given here as the point at which the side force changes sign; it is restricted to the angle of attack range 75° - 90° .

For the triangular cross section, the flow separates from both corners below the critical Reynolds number but remains attached to the windward corner at supercritical Reynolds numbers to provide a positive side-force coefficient.

Square Cross Section

A cylindrical body with a round nose and a square cross section with corner radii 25% of the width of the section was tested earlier (ref. 4) in the 12-Foot Pressure Tunnel. The variation of side-force coefficient at $\psi = 10^\circ$ with Reynolds number and σ is summarized in figure 9 (triangular symbols). Sublimation tests at $R_{hb} = 400,000$ and $\sigma = 45^\circ$ indicated the presence of small stationary vortices which were attributed to inflexional instabilities in the boundary layer.

The side-force coefficients for the square cone at $\psi = 10^\circ$ are also summarized in figure 9. It should be pointed out that the angle between the bottom face of the cone and the relative wind at $\sigma = 75^\circ$ and $\psi = 0^\circ$ is 82.125° and at $\sigma = 90^\circ$ it is 97.125° , a result of the half-cone angle of 7.125° (measured in the plane of symmetry). Thus, one would expect the results at $\sigma = 75^\circ$ and 90° to be approximately the same. The critical Reynolds number based on the square-cylinder data is about 700,000. Thus, all cross sections of the cones should be below critical for $R_{hb} < 700,000$ since all forward sections have smaller local Reynolds numbers and all cross sections of the cone aft of the nose section (32 in. from the base where $h = 4$ in.) should be supercritical for $R_{hb} > 700,000 \times 3$. If the Reynolds number for the cone were based on a height about two thirds of the base height, the critical points for $\sigma = 75^\circ$ and 90° would agree fairly closely for the cones and for the cylinder, since the cylinder height is two thirds of the height of the base of the cone. The less abrupt change in side-force direction shown for the sharp cone is to be expected, because the forward sections become critical at higher unit Reynolds numbers than the sections nearer the base.

The behavior of the blunt cone at $\sigma = 45^\circ$ and 60° follows reasonably well the trends of the cylinder data, but the large effect of the sharp nose in creating an asymmetric vortex flow field with consequent side-force variations is clearly evident, particularly at $\sigma = 45^\circ$.

Several hysteresis runs were made for the sharp and blunt cones holding β fixed at zero and varying α from 0° to 90° . The results are shown in figure 10 for the sharp cone and in figure 11 for the blunt cone. Surprisingly, very little hysteresis effect was found in either case except at one point. Asymmetric forces occurred at angles of attack between 30° and 60° for the sharp cone and between 60° and 75° for the blunt cone. An example of a hysteresis test in β is shown in figure 12 where the side- and normal-force coefficients are plotted versus β at $\alpha = 30^\circ$. As can be seen, the side force is highly nonlinear in the beta range -6° to $+6^\circ$ for this configuration.

Triangular Cross Section

The triangular cross section is considerably more sensitive than the square cross section to changing flow conditions. The variation with R_{hb} of the cross-force coefficient for $\sigma = 45^\circ$, 75° , and 90° at $\psi = 10^\circ$ is shown in figure 13. Two-dimensional data obtained by Polhamus et al. (ref. 2) in a different tunnel is shown in the $\sigma = 90^\circ$ plot for comparison. The critical Reynolds number for the cylinder at $\sigma = 90^\circ$ is about 0.7×10^6 ; it was 0.4×10^6 in the data of Polhamus et al. The critical Reynolds number for the cone is about 0.85×10^6 .

The comment made earlier concerning the cone-angle effect for the square cone applies here as well, the angle of attack of the bottom face being 83.58° for $\sigma = 75^\circ$ and 98.58° at $\sigma = 90^\circ$. However, the results show a difference between $\sigma = 75^\circ$ and 90° in \bar{C}_y at Reynolds numbers above 10^6 . The large difference in \bar{C}_y between the cone and cylinder at $\sigma = 45^\circ$ is primarily a result of the sharp nose on the cone.

Figure 14 shows \bar{C}_y and \bar{C}_z versus α , $\beta = 0$, for three different Reynolds numbers for the blunt triangular cone. The maximum absolute value of \bar{C}_z occurs near $\sigma = 70^\circ$, and the maximum side-force asymmetry occurs near $\sigma = 60^\circ$.

6. PRESSURE-DISTRIBUTION PLOTS

A brief discussion of the pressure-distribution plots of the form C_p versus \hat{z}/h is given in this section. These plots fall into two categories: (1) α -sweeps with $\beta = \psi = 0$ at a given Reynolds number, and (2) ψ fixed at 10° for $\sigma = 45^\circ$, 60° , 75° , and 90° and at varying Reynolds numbers. In each case, the pressure distributions at the three stations are arranged in order across the page with station 1 being nearest the nose. The cross-hatched lines at the bottom of the figures outline the cross-sectional shape of the model.

Models with Square Cross Sections: $\beta = \psi = 0$

Figure 15 shows an α -sweep for $R_{hb} = 0.8 \times 10^6$ for the sharp square cone. The local Reynolds number at station 2 is close to the critical value, and small changes in α have an appreciable effect, as shown by comparing the results at station 3 for $\alpha = 80^\circ$, 85° , and 90° . For α between 65° and 75° , all three stations have about the same pressure distributions. For α between 40° and 60° , the asymmetries in the flow are quite apparent, with the asymmetry switching sides between $\alpha = 40^\circ$ and $\alpha = 50^\circ$.

The effect of doubling the Reynolds number to 1.6×10^6 for the sharp square cone may be seen by comparing figure 15 with figure 16. For $R_{hb} = 1.6 \times 10^6$, station 1 is near critical, which is evidenced by the erratic behavior at $\alpha = 85^\circ$ and $\alpha = 90^\circ$.

The largest asymmetry occurs at station 2 for both Reynolds numbers: $\hat{C}_y = 0.563$ at $\alpha = 40^\circ$, $R_{hb} = 0.8 \times 10^6$ and $\hat{C}_y = -0.561$ at $\alpha = 50^\circ$, $R_{hb} = 1.6 \times 10^6$.

The effects of blunting the nose are shown in figure 17 for $R_{hb} = 0.8 \times 10^6$ and in figure 18 for $R_{hb} = 1.6 \times 10^6$, where it can be seen that the major asymmetries are virtually eliminated.

Models with Square Cross Sections: $\psi = 10^\circ$

Pressure distributions for the sharp square cone at several Reynolds numbers are shown in figure 19 ($\sigma = 45^\circ$), figure 20 ($\sigma = 60^\circ$), and figure 21 ($\sigma = 90^\circ$); pressure distributions for the blunt cone are shown in figure 22 ($\sigma = 45^\circ$) and figure 23 ($\sigma = 60^\circ$). The results for $\sigma = 90^\circ$ are similar to those of the sharp cone and are not shown. The behavior at $\sigma = 90^\circ$ follows rather closely what one would expect based on the local critical Reynolds number. For example, at $R_{hb} = 1.6 \times 10^6$, all stations show supercritical behavior.

The effect of blunting the nose at $\sigma = 60^\circ$ can be seen by comparing figures 20 and 23. The major difference occurs at $R_{hb} = 1.2 \times 10^6$, where the lee side shows an earlier separation for the sharp cone. Referring to figure 9, it can be seen that the magnitude of the side-force coefficient continues to increase more rapidly with Reynolds numbers for the sharp cone than for the blunt cone. Figures 20 and 23 show that this is so because the lee side of the sharp cone develops higher negative peak pressures at stations 1 and 2 than the blunt cone.

The effect of blunting the cone at $\sigma = 45^\circ$ can be seen by referring to figures 19 and 22. The α -sweep curves for the sharp cone shown in figure 10, where $\psi = 0$, show that one would expect the largest effects of the sharp nose to occur in the range of $30^\circ < \alpha < 50^\circ$. Figure 9, where $\alpha = 45^\circ$ and $\psi = 10^\circ$, shows that this is indeed the case. Generally, it has been found that the major variations in side-force coefficients are due to the behavior around the two bottom corners (facing into the wind). Here, the major effects occur along the sides and near the top corner. The saw-tooth shape of the sharp cone data shown in figure 9 is due to crossings of the lee and windward pressure distribution curves: there is a low negative value when they cross and a high negative value when they do not, as shown in figure 19. For the blunt cone these cross at least once at each Reynolds number as shown in figure 22.

Models with Triangular Cross Section: $\beta = \psi = 0$

Sweeps in angle of attack were performed only for the blunt triangular cone and at three Reynolds numbers. The results for $R_{hb} = 0.76 \times 10^6$ are shown in figure 24. The critical Reynolds number for the triangular cylinder at $\alpha = 90^\circ$ is about 0.7×10^6 . Thus, for $R_{hb} = 0.76 \times 10^6$ all sections should be below critical except, possibly, the base; this is verified by the pressure distributions at all three stations for $\alpha \geq 75^\circ$. For $40^\circ < \alpha < 65^\circ$, a flat peak, typical of blunt noses at the lower Reynolds numbers, is evident.

Figure 25 shows the results for $R_{hb} = 1.1 \times 10^6$. The results are somewhat similar to those at $R_{hb} = 0.76 \times 10^6$ for station 1 for $45^\circ < \alpha < 60^\circ$, but are different at station 2. Figure 26 shows the results for $R_{hb} = 1.6 \times 10^6$. Here it is supposed that inflexional instabilities produce a turbulent boundary layer for $45^\circ < \alpha < 65^\circ$ at the forward station. For $75^\circ < \alpha < 90^\circ$, station 1 is in the subcritical range,

station 2 is in the transitional range, and station 3 is above the critical range. Figures 27 and 28 show the large asymmetries that can be produced by the sharp nose for $\sigma = 45^\circ$ and 60° , respectively, at $\psi = 0$.

Models with Triangular Cross Sections: $\psi = 10^\circ$

For tests with the model rolled about the x-axis, σ was limited to 45° , 60° , and 90° . Pressure distribution plots (for the triangular cylinder) at several Reynolds numbers with $\psi = 10^\circ$, are shown in figure 29 ($\sigma = 40^\circ$), figure 30 ($\sigma = 60^\circ$), and figure 31 ($\sigma = 90^\circ$). Similar plots for the sharp triangular cone are shown in figures 32-34. The blunt triangular cone was tested only at $\psi = 0^\circ$.

The data for the triangular cylinder at $\sigma = 45^\circ$ and 60° in figures 29 and 30 at the lower Reynolds numbers show the flat peak at the forward stations that seems to be typical of blunt-nosed bodies at angles of attack in this range (see, e.g., the pressure distributions on the blunt cones in figs. 17 and 24).

Another noteworthy feature of the cylinder data is that at the two forward stations for $\sigma = 45^\circ$ and 60° , shown in figures 29 and 30, the peak negative pressure occurs on the lee corner for all Reynolds numbers tested, whereas, at $\sigma = 90^\circ$ (fig. 31), the peak negative pressure occurs on the windward corner at all Reynolds numbers tested.

Referring to figure 13, $\sigma = 90^\circ$, it can be seen that the critical R_{hb} for triangular cross sections is about 0.8×10^6 . The pressure distributions in figure 31 at $R_{hb} = 0.8 \times 10^6$ reflect this proximity to the critical Reynolds number, with station 2 exhibiting subcritical and stations 1 and 3 supercritical behavior. For $R_{hb} > 0.8 \times 10^6$ the forward two stations exhibit supercritical behavior.

The main feature of the sharp triangular cone data at $\sigma = 45^\circ$ and $\psi = 10^\circ$ shown in figure 32 is the similarity in pressure distributions to the $\psi = 0^\circ$ case in figure 27. In other words, the asymmetry that developed at $\psi = 0^\circ$ had about the same effect as rolling the body 10° about the x-axis. By coincidence, the asymmetry happened to be in the same direction.

For the sharp cone at $\sigma = 90^\circ$ (fig. 34), the pressure distributions depend on the local Reynolds number, R_{hj} . For example, at $R_{hb} = 2.0 \times 10^6$, $R_{h_1} = 0.83 \times 10^6$, $R_{h_2} = 1.25 \times 10^6$, and $R_{h_3} = 1.83 \times 10^6$, with R_{hj} near the critical value of 800,000. It is thought that the peak at station 2 is larger than that at station 3 because of the gap between the fairing and the model. Model support dynamics prevented runs at higher Reynolds numbers for this configuration and angle of attack.

7. INVERTED TRIANGULAR CYLINDER

A brief investigation was carried out on the triangular cylinder in the inverted position, that is, with the apex toward the flow. Side-force coefficients for $\psi = 10^\circ$ are plotted against Reynolds number in figure 35 for $\sigma = 45^\circ$, 60° , 75° , and 90° . The two-dimensional data taken from reference 2 are shown by the broken line ($\sigma = 90^\circ$). The shapes of the curve at different σ 's are somewhat similar, with

the change in sign of $\overline{C_y}$ occurring at higher Reynolds numbers with increasing σ . The corresponding pressure distributions are shown in figure 36 ($\sigma = 45^\circ$), figure 37 ($\sigma = 60^\circ$), and figure 38 ($\sigma = 90^\circ$).

In the inverted position, the peak negative pressures, as calculated using two-dimensional potential theory, occur on the windward corner, which is opposite to findings for the upright case.

At $\sigma = 90^\circ$ (see fig. 38), at the lowest Reynolds number tested, the flow separates very early on the windward downstream corner. However, the lee side has a less severe adverse pressure gradient, and a peak negative pressure develops that does not change much within the Reynolds number range tested. As R_{hb} reaches 1.33×10^6 , the windward corner develops a large negative peak that tends to dominate.

At $\sigma = 45^\circ$, the effect of the blunt nose at low Reynolds numbers is evident at the two forward stations, at $R_{hb} = 0.4 \times 10^6$. For $R_{hb} \geq 0.67 \times 10^6$, the flow around the windward corner develops a dominant negative peak at all three stations.

The flow about the lee corner appears to separate early at station 3 for the entire range of Reynolds numbers tested.

8. FLOW VISUALIZATION

Sublimation tests to determine the state of the boundary layer and oil-flow tests to record skin-friction lines were conducted. A run schedule for these tests is shown in table 3, and the effect on $\overline{C_y}$ and $\overline{C_z}$ of the change in surface conditions is given in table 8.

Sublimation Tests

The principal objective of the sublimation tests was to determine the conditions for the appearance of inflexional instabilities in the laminar boundary layer. In previous tests (ref. 4), a solution of biphenyl crystals ($C_6H_5C_6H_5$) dissolved in petroleum ether was sprayed on the model; it left a white surface that was then smoothed to a glossy finish with ordinary writing paper.

Because of safety concerns of using petroleum ether in the 12-ft tunnel, trichloroethane (CH_3CCl_3) was used as a solvent in the present tests. Whether this change in solvent was responsible or not, the telltale striations that are evidence of the presence of small vortices in the boundary layer were not observed. Another possibility for their absence is that the model support system was too flexible and the periodic movement of the model smeared the surface patterns.

Oil-Flow Tests

Both oil smears and oil dots were run. In the former, a mixture of motor oil and black oxide was smeared over the model by hand. The tunnel was brought up to run condition and held until the pattern had stabilized. The tunnel was then shut down and photographs taken of the model. Brown wrapping paper was then pressed around the

model and an imprint was left on the paper; thus an "unwrapped" view of the pattern was obtained.

The flow pattern obtained on the blunt triangular cone at $\sigma = 45^\circ$ and a Reynolds number of 1.1×10^6 is shown in figure 39. Oil-flow patterns on the sharp triangular cone at the same Reynolds number are shown in figure 40 for $\sigma = 45^\circ$ and in figure 41 for $\sigma = 60^\circ$.

In the oil-dot experiments, small dots of the mixture used in the smear tests were placed on the model with a draftsman's ruling pen; the dots were placed in rows (about 3 cm apart) parallel to the base, with a spacing about 1 cm apart around the body. Generally, the dot technique affected the flow more than either the sublimation or the oil-smear technique. For example (see table 8), the dots on the sharp triangular cone (configuration 51), at $\sigma = 60^\circ$, $\psi = 10^\circ$, and $R_{hb} = 1.6 \times 10^6$, change the side-force coefficient $\overline{C_y}$ from -0.0989 for the clean condition to 0.5378 in one run and to 0.5487 in another. Because of the discrepancy in data between the clean and the oil dot configurations, the oil dot flow patterns are not shown.

9. CONCLUSIONS

Wind-tunnel tests were carried out on a cone and a cylinder with triangular cross sections and a cone with a square cross section. Both cones were furnished with sharp and blunt noses. Test variables ranged over a wide range of Reynolds numbers and angles of attack to 90° .

Results show that the flows on such bodies are very complex and are highly dependent on Reynolds number and on angle of attack. In general, it was found that the pressure distributions and forces for the angle of attack range from 75° to 90° are fairly predictable from results on two-dimensional cylinders of the same cross section when using the local Reynolds number (based on local section height) to correlate the data. At angles of attack below about 75° , nose effects dominate and the body cannot be considered as a cylinder in two-dimensional crossflow.

The sharp-nosed cones showed large asymmetries and very complex surface flow patterns at $\sigma = 45^\circ$ and 60° , $\psi = 0^\circ$. The asymmetries were removed, or greatly reduced by blunting the nose.

Force data taken during oil-flow runs showed large differences in the side-force coefficients between the clean and the dirty configurations under certain conditions. The sensitivity to surface roughness of these bodies with the noncircular cross sections is not surprising, and a careful experimental study of the effects of roughness on the aerodynamic characteristics at high angles of attack would be very desirable.

REFERENCES

1. Polhamus, E. C.: Effect of Flow Incidence and Reynolds Number on Low-Speed Aerodynamic Characteristics of Several Noncircular Cylinders with Applications to Directional Stability and Spinning. NACA TN-4176, 1958.
2. Polhamus, E. C.; Geller, E. W.; and Grunwald, K. H.: Pressure and Force Characteristics of Noncircular Cylinders as Affected by Reynolds Number with a Method Included for Determining the Potential Flow about Arbitrary Shapes. NASA TR-R46, 1959.
3. Hasel, L. E.; and Kouyoumjian, W. L.: Investigation of Static Pressures and Boundary Layer Characteristics on the Forward Parts of Nine Fuselages of Various Cross-Sectional Shapes at $M_\infty = 2.01$. NACA RML-56113, 1957.
4. Clarkson, M. H.; Malcolm, G. N.; and Chapman, G. T.: Experimental Post-Stall Rotary Aerodynamic Coefficients for Airplane-Like Configurations. J. Aircraft, vol. 13, Aug. 1976, pp. 565-570.
5. Clarkson, M. H.; Malcolm, G. N.; and Chapman, G. T.: A Subsonic, High-Angle-of-Attack Flow Investigation at Several Reynolds Numbers. AIAA J., vol. 16, no. 1, Jan. 1978, pp. 53-60.
6. Clarkson, M. H.; Malcolm, G. N.; and Brittain, V. A.: Aerodynamic Characteristics of Bodies with Noncircular Cross Sections at High Angles of Attack. AIAA Paper 82-0056, 1982.
7. Allen, H. J.; and Perkins, E. W.: Characteristics of Flow over Inclined Bodies of Revolution. NACA RM-A50L07, 1951.

TABLE 1.- MODEL/STING COMBINATIONS

Configuration No. ^a	Model	Type of data	Sting ^b
10	Cone, square cross section, sharp nose	Force and pressure	Straight
110	Cone, square cross section, sharp nose	Force and pressure	Bent
111	Cone, square cross section, sharp nose	Force and flow visualization	Bent
20	Cone, square cross section, blunt nose	Force and pressure	Straight
120	Cone, square cross section, blunt nose	↓	Bent
30	Cylinder, triangular cross section, upright	↓	Straight
40	Cylinder, triangular cross section, inverted	↓	Straight
140	Cylinder, triangular cross section, inverted	↓	Bent
50	Cone, triangular cross section, sharp nose	↓	Straight
51	Cone, triangular cross section, sharp nose	Force and flow visualization	↓
60	Cone, triangular cross section, blunt nose	Force and pressure	↓
61	Cone, triangular cross section, blunt nose	Force and flow visualization	↓

^aThe triangular cone models were all tested in the upright position with the flat bottom facing into the wind.

^bBent sting $0^\circ \leq \sigma \leq 45^\circ$; straight sting $40^\circ \leq \sigma \leq 90^\circ$.

TABLE 2.- RUN SUMMARY

Configuration	Reynolds number, million													
	0.25	0.4	0.6	0.8	1.0	1.2	1.4	1.6	2.0	2.4	2.8	3.2	3.6	4.0
030	25-30	31-36		37-42		43-47		4-9	48-52	53-57	58-62	24 63-66	18-23	10-17
040			67-68		69-70	101-102	71-72		99-100		97-98		95-96	
140			74-75		76-77		78-79							
130		89-91				92-94			86-88		83-85		80-82	
050	103-107	108-112		113-117 159		118-122 161		123-127 160	128-132		135	134	133	
051						145-148 151-152		136-144 149-150						
060				156		158 162,164		157 163						
061														
010	172-174	175-177		165 178-179		166-168 180-181		169-171	197-199	194-196	191-193	188-190	185-187	182-184
020	200-202	203-205		206-208	209-211	212-216		235-237	232-234	229-231	226-228	223-225	220-222	217-219
120	242-244			245-247				239-241		254-256		251-253		248-250
110	268-270			271-273		266-267		263-265		260-262		257-259		274-276
111						278-279								

Configuration key: Hundred's digit: 0 (high AoA range), 1 (low AoA range); ten's digit: 1 (square cone, sharp nose), 2 (square cone, blunt nose), 3 (triangular cylinder, upright), 4 (triangular cylinder, inverted), 5 (triangular cone, sharp nose), 6 (triangular cone, blunt nose); one's digit: 0 (force and pressure data), 1 (flow visualization).

ORIGINAL PAGE IS
OF POOR QUALITY

TABLE 3.- RUN SUMMARY: FLOW VISUALIZATION

Configuration No.	Angles, deg		Run number					
			Sublimation		Oil smear		Oil dot	
	σ	ψ	1.2 ^a	1.6 ^a	1.2 ^a	1.6 ^a	1.2 ^a	1.6 ^a
51	45	0			146			
	60	0			147			
	45	10	151	140	145		148	
	60	10	152	136, 137		142-144		149
	75	10				150		
61	45	0			162		164	
	60	0				163		
111	35	0			278			
	40	0			279			

^aUnit Reynolds number, million.

ORIGINAL PAGE IS
OF POOR QUALITY

TABLE 4.- RUN SCHEDULE

ORIGINAL PAGE IS
OF POOR QUALITY

Run No.	Run sequence Nos. (from)	Run sequence Nos. (to)	Configuration code	Mach No.	Tunnel unit Reynolds No.	Free-stream dynamic pressure, lb/ft ²	Free-stream static pressure, lb/ft ²	Roll angle, deg
4	5	8	30	0.249	1.626	87.7	2015.2	0.00
5	1	4		.248	1.599	86.7	2016.1	4.90
6	↓	4		.249	1.594	87.7	2014.7	9.91
7		4		.249	1.585	87.4	2015.2	9.91
8		8		.250	1.600	88.4	2014.2	14.81
9	↓	4		.249	1.599	87.8	2015.2	19.77
10	12	15		.248	3.951	214.6	5001.9	.04
11	1	5		.251	3.958	218.5	5012.3	4.85
12	↓	7		.251	3.994	223.6	5070.7	9.68
13		3		.250	4.002	223.9	5122.6	9.79
14		3		.249	3.988	222.8	5129.2	14.66
15	↓	2		.249	3.970	221.5	5122.0	19.82
16	7	8		.248	3.984	215.6	5014.5	14.70
17	1	2		.249	3.991	218.2	5021.4	19.68
18	↓	2		.249	3.612	197.3	4542.9	.01
19		2		.250	3.604	198.2	4545.6	4.80
20		4		.249	3.584	197.2	4540.6	9.69
21		3		.249	3.574	197.1	4533.1	9.76
22		3		.249	3.564	196.8	4524.7	14.52
23		3		.249	3.546	195.6	4515.6	19.67
24	↓	2		.246	3.204	174.0	4107.6	-.01
25	5	8		.147	.248	7.8	515.1	.02
26	1	4		.147	.254	8.0	528.2	4.95
27	↓	↓		.148	.257	8.2	534.1	9.99
28				.149	.262	8.4	539.0	9.98
29				.147	.261	8.3	544.1	14.89
30				.148	.264	8.4	548.4	19.85
31		↓		.251	.398	21.3	482.5	.03
32				.252	.401	21.6	487.6	4.95
33		5		.251	.405	21.8	493.8	10.00
34		4		.251	.409	22.1	499.2	9.98
35		4		.251	.412	22.2	504.7	14.86
36	↓	4		.251	.418	22.6	510.9	19.80
37	8	11		.251	.819	43.2	976.5	.00
38	1	4		.250	.816	43.4	988.0	4.96
39	↓	↓		.252	.821	44.1	996.5	10.00
40				.250	.820	44.0	1005.4	9.99
41				.250	.824	44.4	1013.1	14.90
42				.250	.825	44.8	1021.1	19.84
43				.249	1.215	66.5	1531.8	.02
44				.251	1.240	68.4	1553.7	4.90
45				.249	1.246	68.4	1574.2	10.18
46				.248	1.264	69.4	1608.5	14.83
47	↓	↓		.250	1.214	67.1	1536.3	19.79
48	7	10		.249	1.998	109.8	2532.8	.00
49	1	4	↓	.250	2.010	111.2	2551.7	4.87

TABLE 4.- Continued.

ORIGINAL PAGE IS
OF POOR QUALITY

Run No.	Run sequence Nos. (from)	Run sequence Nos. (to)	Config-uration code	Mach No.	Tunnel unit Reynolds No.	Free-stream dynamic pressure, lb/ft ²	Free-stream static pressure, lb/ft ²	Roll angle, deg
50	1	4	30	0.249	2.002	110.8	2547.5	9.89
51	↓	↓	↓	.250	1.998	110.8	2541.3	14.75
52	↓	↓	↓	.250	1.994	110.8	2535.5	19.72
53	↓	↓	↓	.249	2.406	134.8	3096.6	.04
54	↓	↓	↓	.250	2.429	136.3	3103.2	4.88
55	↓	↓	↓	.250	2.422	135.8	3095.2	9.81
56	↓	↓	↓	.250	2.412	135.2	3080.8	14.73
57	↓	↓	↓	.251	2.411	135.6	3071.3	19.71
58	↓	3	↓	.249	2.801	157.4	3622.4	-.01
59	↓	4	↓	.250	2.821	158.9	3623.8	4.83
60	↓	4	↓	.251	2.816	158.8	3609.3	10.16
61	↓	4	↓	.250	2.790	156.9	3586.5	14.68
62	↓	3	↓	.250	2.786	156.9	3575.0	19.73
63	↓	4	↓	.249	3.214	180.7	4181.0	4.80
64	↓	4	↓	.250	3.229	182.7	4162.8	9.79
65	↓	3	↓	.250	3.218	181.7	4149.6	14.70
66	↓	3	↓	.250	3.206	180.9	4138.1	19.73
67	7	11	40	.253	.620	33.4	745.8	.04
68	1	4	↓	.255	.625	34.2	751.8	10.00
69	↓	↓	↓	.251	.992	54.3	1228.0	.04
70	↓	↓	↓	.253	1.005	55.4	1234.8	10.01
71	↓	↓	↓	.252	1.380	76.5	1722.6	.03
72	↓	↓	↓	.252	1.383	76.5	1726.1	9.99
74	4	6	140	.248	.614	32.3	751.1	.00
75	1	2	↓	.248	.604	32.1	743.6	10.02
76	↓	3	↓	.249	1.016	55.0	1264.2	.06
77	↓	2	↓	.251	1.037	56.5	1280.7	9.96
78	↓	3	↓	.250	1.407	77.9	1778.2	.02
79	↓	2	↓	.252	1.435	79.8	1791.4	9.91
80	11	13	130	.249	3.586	196.6	4532.0	.04
81	1	3	↓	.250	3.588	199.0	4536.1	10.15
82	↓	↓	↓	.250	3.565	198.1	4535.6	20.04
83	↓	↓	↓	.249	2.798	154.5	3554.4	.11
84	↓	↓	↓	.250	2.799	155.8	3549.5	10.05
85	↓	↓	↓	.250	2.787	155.2	3544.2	20.04
86	↓	↓	↓	.248	1.986	108.7	2521.1	.04
87	↓	↓	↓	.249	1.988	109.6	2520.7	10.11
88	↓	↓	↓	.250	1.987	109.9	2517.8	19.99
89	↓	↓	↓	.250	.392	20.9	478.6	.04
90	↓	↓	↓	.252	.396	21.4	483.2	10.04
91	↓	↓	↓	.251	.397	21.5	488.1	19.95
92	↓	↓	↓	.250	1.199	66.2	1518.7	.05
93	↓	↓	↓	.250	1.216	67.1	1537.1	10.11
94	↓	↓	↓	.250	1.222	67.6	1541.6	19.95
95	6	9	40	.250	3.659	199.1	4542.5	.03
96	1	5	40	.251	3.647	201.4	4567.9	10.00

TABLE 4.- Continued.

ORIGINAL PAGE IS
OF POOR QUALITY

Run No.	Run sequence Nos. (from)	Run sequence Nos. (to)	Config-uration code	Mach No.	Tunnel unit Reynolds No.	Free-stream dynamic pressure, lb/ft ²	Free-stream static pressure, lb/ft ²	Roll angle, deg
97	1	4	40	0.247	2.763	150.6	3522.3	0.00
98	↓	↓	↓	.251	2.794	155.9	3527.4	10.01
99	↓	↓	↓	.251	1.998	110.8	2522.9	.01
100	↓	↓	↓	.253	2.009	113.3	2526.7	10.01
101	↓	↓	↓	.251	1.211	67.0	1518.7	.00
102	↓	↓	↓	.251	1.213	67.4	1524.5	9.99
103	19	22	50	.145	.249	7.7	522.7	.05
104	1	4	↓	.146	.252	7.9	526.4	4.99
105	↓	↓	↓	.146	.253	7.9	532.0	10.07
106	↓	↓	↓	.146	.255	8.0	537.4	15.00
107	↓	↓	↓	.146	.258	8.1	542.3	10.00
108	↓	↓	↓	.251	.399	21.4	487.1	.02
109	↓	↓	↓	.250	.400	21.6	493.0	4.98
110	↓	↓	↓	.249	.402	21.7	498.7	10.04
111	↓	↓	↓	.249	.405	21.8	504.0	14.93
112	↓	↓	↓	.249	.409	22.1	508.6	19.94
113	↓	↓	↓	.251	.805	44.3	1002.5	.00
114	↓	↓	↓	.251	.809	44.5	1006.9	4.94
115	↓	↓	↓	.250	.809	44.3	1011.5	9.98
116	↓	↓	↓	.250	.811	44.3	1015.7	14.85
117	↓	↓	↓	.250	.815	44.7	1019.9	19.87
118	↓	↓	↓	.251	1.203	66.7	1516.1	.04
119	↓	↓	↓	.250	1.221	67.3	1534.0	4.88
120	↓	↓	↓	.250	1.232	67.8	1549.4	9.89
121	↓	↓	↓	.250	1.246	68.6	1564.1	14.72
122	↓	↓	↓	.250	1.255	69.1	1580.3	19.75
123	↓	↓	↓	.251	1.590	88.2	2006.0	.01
124	↓	↓	↓	.250	1.598	88.2	2008.0	4.83
125	↓	↓	↓	.251	1.604	88.5	2009.5	9.79
126	↓	↓	↓	.251	1.605	88.5	2012.6	14.60
127	↓	↓	↓	.250	1.604	88.4	2016.4	19.66
128	↓	2	↓	.248	1.983	108.1	2514.5	-.09
129	↓	2	↓	.250	1.994	110.1	2514.7	4.65
130	↓	4	↓	.252	2.001	111.4	2511.1	9.71
131	↓	4	↓	.250	1.982	109.6	2503.1	14.51
132	↓	4	↓	.250	1.979	109.4	2494.1	19.56
133	5	5	↓	.245	3.534	188.6	4485.8	19.50
134	1	1	↓	.243	3.161	167.4	4038.4	19.54
135	1	2	↓	.245	2.736	147.0	3485.8	19.35
136	5	5	51	.248	1.617	87.3	2028.9	9.83
137	3	5	↓	.246	1.597	86.2	2028.7	9.83
138	↓	5	↓	.247	1.600	86.9	2028.2	9.87
139	↓	5	↓	.249	1.603	88.1	2027.2	9.94
140	↓	4	↓	.249	1.628	88.1	2027.0	9.41
141	↓	3	↓	.249	1.645	88.0	2028.2	9.91

TABLE 4.- Continued.

Run No.	Run sequence Nos. (from)	Run sequence Nos. (to)	Config-uration code	Mach No.	Tunnel unit Reynolds No.	Free-stream dynamic pressure, lb/ft ²	Free-stream static pressure, lb/ft ²	Roll angle, deg
142	3	5	51	0.250	1.651	88.7	2027.9	9.83
143	4	4	↓	.236	1.603	79.8	2039.5	9.80
144	3	3	↓	.237	1.563	80.3	2038.2	9.85
145	↓	3	↓	.169	1.125	41.3	2078.1	9.73
146	↓	3	↓	.187	1.240	50.8	2066.3	-.33
147	↓	3	↓	.186	1.233	50.3	2066.1	.04
148	↓	4	↓	.187	1.257	50.8	2066.0	9.87
149	↓	4	↓	.250	1.665	88.6	2027.6	9.69
150	1	2	↓	.250	1.667	88.9	2026.6	9.74
151	3	5	↓	.161	1.117	37.7	2081.2	9.74
152	3	3	↓	.154	1.062	34.5	2086.3	9.96
156	9	19	60	.250	.763	40.4	918.7	.04
157	1	11	60	.250	1.600	87.0	1980.0	.02
158	2	12	60	.165	1.108	89.6	2080.1	.04
159	13	23	50	.250	.810	42.8	979.5	-.04
160	1	11	50	.251	1.628	89.5	2034.8	-.05
161	1	11	50	.166	1.101	40.0	2086.2	-.03
162	7	7	61	.165	1.111	39.5	2086.3	.06
163	3	4	61	.247	1.620	86.7	2035.9	.02
164	3	4	61	.164	1.104	39.9	2085.5	.06
165	11	32	10	.250	.811	43.1	985.9	.03
166	1	22	↓	.250	1.249	68.1	1560.1	.03
167	1	21	↓	.250	1.206	66.2	1513.7	Vary
168	1	21	↓	.250	1.165	64.5	1472.5	Vary
169	4	25	↓	.251	1.606	89.2	2020.4	-.01
170	1	4	↓	.251	1.605	88.8	2020.6	5.01
171	1	4	↓	.250	1.599	88.1	2021.0	10.05
172	3	6	↓	.146	.238	7.4	495.8	.04
173	1	5	↓	.147	.240	7.6	500.7	4.99
174	↓	4	↓	.147	.243	7.7	506.1	10.08
175	↓	↓	↓	.251	.411	22.1	501.6	.03
176	↓	↓	↓	.251	.414	22.4	507.2	4.99
177	↓	↓	↓	.251	.418	22.7	514.8	10.08
178	↓	↓	↓	.251	.798	44.1	1000.4	5.00
179	↓	↓	↓	.251	.817	44.9	1021.6	10.06
180	↓	5	↓	.251	1.209	67.2	1528.4	5.03
181	↓	4	↓	.250	1.233	68.1	1551.0	10.10
182	↓	↓	↓	.250	4.001	220.7	5036.3	.11
183	↓	↓	↓	.250	3.979	220.4	5041.7	5.12
184	↓	↓	↓	.250	3.966	220.7	5039.4	10.36
185	↓	↓	↓	.251	3.594	198.6	4508.1	.06
186	↓	↓	↓	.250	3.566	197.8	4510.9	5.11
187	↓	↓	↓	.251	3.557	198.1	4504.3	10.32
188	↓	↓	↓	.250	3.210	177.0	4039.1	.02
189	↓	↓	↓	.251	3.198	177.6	4040.7	5.05

TABLE 4.- Continued.

ORIGINAL PAGE 1.
OF POOR QUALITY

Run No.	Run sequence Nos. (from)	Run sequence Nos. (to)	Configuration code	Mach No.	Tunnel unit Reynolds No.	Free-stream dynamic pressure, lb/ft ²	Free-stream static pressure, lb/ft ²	Roll angle, deg
190	1	4	10	0.251	3.187	177.4	4036.0	10.18
191	↓	↓	↓	.250	2.804	154.8	3538.6	.03
192	↓	↓	↓	.250	2.793	154.9	3536.0	5.04
193	↓	↓	↓	.251	2.792	155.6	3528.7	10.18
194	↓	↓	↓	.252	2.402	133.1	3001.7	.01
195	↓	↓	↓	.252	2.392	133.7	3005.3	5.05
196	↓	↓	↓	.251	2.373	132.7	3006.0	10.17
197	↓	↓	↓	.250	1.989	110.2	2527.6	.04
198	↓	↓	↓	.250	1.982	110.8	2530.0	5.04
199	↓	↓	↓	.250	1.976	111.0	2530.0	10.15
200	7	10	20	.144	.246	7.5	512.5	.03
201	1	4	↓	.144	.246	7.5	516.7	5.01
202	↓	↓	↓	.144	.248	7.6	522.7	10.06
203	↓	↓	↓	.249	.401	21.2	486.8	.04
204	↓	↓	↓	.250	.405	21.6	492.8	5.03
205	↓	↓	↓	.249	.408	21.7	501.3	10.09
206	↓	23	↓	.250	.818	44.7	1023.1	.03
207	↓	4	↓	.251	.840	46.2	1050.4	4.97
208	↓	↓	↓	.250	.778	42.6	977.3	10.03
209	↓	↓	↓	.252	.983	54.7	1235.9	.03
210	↓	↓	↓	.251	1.009	55.8	1265.7	4.99
211	↓	↓	↓	.251	1.035	57.3	1295.7	10.06
212	↓	22	↓	.250	1.188	65.1	1493.7	.03
213	↓	21	↓	.248	1.220	66.4	1548.9	Vary
214	↓	21	↓	.250	1.195	65.7	1503.8	Vary
215	↓	4	↓	.252	1.236	68.5	1545.5	4.98
216	↓	4	↓	.251	1.253	69.3	1570.5	10.07
217	3	6	↓	.250	3.982	221.1	5034.1	.08
218	1	4	↓	.252	3.975	223.1	5036.5	5.01
219	↓	↓	↓	.252	3.967	223.8	5030.8	10.13
220	↓	↓	↓	.250	3.593	200.5	4580.5	.04
221	↓	↓	↓	.251	3.597	202.5	4574.2	5.02
222	↓	↓	↓	.250	3.562	199.7	4565.6	10.11
223	↓	↓	↓	.251	3.204	179.2	4070.4	.04
224	↓	↓	↓	.250	3.182	177.9	4065.2	5.00
225	↓	↓	↓	.250	3.171	177.4	4055.0	10.10
226	↓	↓	↓	.250	2.787	155.4	3544.4	.04
227	↓	↓	↓	.254	2.813	159.2	3532.3	4.96
228	↓	↓	↓	.248	2.743	152.0	3529.1	10.10
229	↓	5	↓	.251	2.399	133.9	3039.1	.04
230	↓	4	↓	.251	2.389	134.2	3039.7	4.99
231	↓	↓	↓	.250	2.367	132.8	3039.0	10.08
232	↓	↓	↓	.250	2.001	111.9	2559.3	.04
233	↓	↓	↓	.250	1.991	112.0	2561.3	5.00
234	↓	↓	↓	.250	1.981	111.7	2560.4	10.09
235	↓	↓	↓	.250	1.593	89.7	2043.9	4.99

TABLE 4.- Concluded.

ORIGINAL PAGE 13
OF POOR QUALITY

Run No.	Run sequence Nos. (from)	Run sequence Nos. (to)	Config-uration code	Mach No.	Tunnel unit Reynolds No.	Free-stream dynamic pressure, lb/ft ²	Free-stream static pressure, lb/ft ²	Roll angle, deg
236	1	4	20	0.250	1.587	89.6	2047.8	10.09
237	↓	22	20	.250	1.588	88.7	2034.4	.02
239	↓	5	120	.249	1.634	87.7	2025.8	.00
240	↓	4	↓	.246	1.590	86.2	2027.2	4.99
241	↓	4	↓	.246	1.577	85.8	2027.7	9.85
242	↓	5	↓	.145	.246	7.7	519.2	-.06
243	↓	4	↓	.144	.252	7.8	539.7	4.97
244	↓	4	↓	.143	.259	8.0	559.9	9.90
245	↓	5	↓	.249	.820	44.7	1031.7	.01
246	↓	4	↓	.256	.843	46.3	1060.2	4.97
247	↓	4	↓	.256	.860	47.5	1080.8	9.88
248	↓	5	↓	.249	4.015	223.4	5139.0	-.05
249	↓	4	↓	.249	3.999	222.4	5137.2	4.95
250	↓	4	↓	.249	3.998	223.2	5133.7	9.92
251	↓	5	↓	.249	3.175	175.7	4045.1	-.06
252	↓	4	↓	.249	3.162	175.9	4047.8	4.97
253	↓	4	↓	.249	3.155	175.7	4041.8	9.90
254	↓	5	↓	.249	2.383	130.7	3022.4	-.07
255	↓	4	↓	.251	2.399	133.8	3024.8	4.95
256	↓	4	↓	.249	2.369	131.4	3027.9	9.91
257	8	12	110	.250	3.200	175.4	4022.3	-.11
258	1	4	↓	.250	3.183	175.8	4030.1	5.12
259	↓	4	↓	.250	3.177	175.8	4032.0	10.22
260	↓	5	↓	.250	2.390	130.9	3001.1	-.07
261	↓	4	↓	.250	2.381	131.5	3007.1	5.14
262	↓	4	↓	.250	2.373	131.0	3004.5	10.08
263	↓	5	↓	.250	1.667	88.6	2028.3	.00
264	↓	4	↓	.250	1.655	88.6	2028.3	5.11
265	↓	4	↓	.235	1.553	79.6	2087.9	10.22
266	3	21	↓	.250	1.138	61.0	1397.1	.03
267	1	21	↓	.250	1.145	62.4	1427.4	Vary
268	↓	5	↓	.144	.238	7.4	507.1	-.06
269	↓	4	↓	.144	.239	7.4	512.0	4.97
270	↓	4	↓	.143	.239	7.4	516.1	9.84
271	↓	5	↓	.249	.796	43.5	1000.8	-.06
272	↓	4	↓	.249	.823	45.0	1036.2	5.00
273	↓	4	↓	.250	.805	44.2	1013.2	9.95
274	↓	5	↓	.249	3.988	222.9	5133.1	-.12
275	↓	4	↓	.236	3.778	202.4	5137.0	5.24
276	↓	6	↓	.178	2.855	Vary	5145.4	10.06
278	5	5	111	.244	1.225	64.0	1542.6	.00
279	3	4	111	.260	1.269	70.6	1490.9	-.26

TABLE 5.- MODEL GEOMETRIC DATA
[Length in cm, areas in cm²]

ORIGINAL PAGE IS
OF POOR QUALITY

Model	Config- uration No.	A _b	L	A _y /A _b	A _z /A _b	h ₁ /h _b	h ₂ /h _b	h ₃ /h _b
Sharp, square cone	10	879.16	121.92	2.11	2.11	0.459	0.615	0.958
Blunt, square cone	20	879.16	121.92	1.89	1.89	.459	.615	.958
Triangular cylinder	30,40	374.84	86.36	4.61	5.62	1.0	1.0	1.0
Sharp, triangular cone	50	835.16	121.92	2.22	2.71	.417	.625	.917
Blunt, triangular cone	60	835.16	121.92	2.00	2.44	.417	.625	.917

Example: $\overline{C}_y = CY \div 4.61$, triangular cylinder

$\overline{C}_z = CZ \div 5.62$, triangular cylinder

TABLE 6.- \hat{z}/h AND s/s_0 VERSUS TAP NUMBER:
SQUARE CROSS SECTION

Port side C _p symbol =			Starboard side C _p symbol =		
Tap No.	\hat{z}/h	s/s_0	Tap No.	\hat{z}/h	s/s_0
01	0	0	24	1.0000	0.5000
02	0	.0247	25	1.0000	.5376
03	0	.0510	26	.9972	.5804
04	.0028	.0804	27	.9837	.5956
05	.0163	1.0956	28	.9599	.6130
06	.0402	.1130	29	.9268	.6250
07	.0732	.1250	30	.8859	.6371
08	.1141	.1371	31	.8387	.6544
09	.1613	.1544	32	.7871	.6696
10	.2129	.1696	33	.7332	.6846
11	.2669	.1846	34	.6340	.7124
12	.3660	.2124	35	.5000	.7500
13	.5000	.2500	36	.3660	.7876
14	.6340	.2876	37	.2669	.8154
15	.7332	.3154	38	.2129	.8304
16	.7871	.3304	39	.1613	.8456
17	.8387	.3456	40	.1141	.8630
18	.8859	.3630	41	.0732	.8750
19	.9268	.3750	42	.0402	.8871
20	.9599	.3871	43	.0163	.9044
21	.9837	.4044	44	.0028	.9196
22	.9972	.4196	45	0	.9490
23	1.0000	.4624	46	0	.9753
24	1.0000	.5000	01	0	1.0000

TABLE 7.- \hat{z}/h AND s/s_0 VERSUS TAP NUMBER:
TRIANGULAR CROSS SECTION

ORIGINAL PAGE 6
OF POOR QUALITY

Port side C_p symbol =			Starboard side C_p symbol =		
Tap No.	\hat{z}/h	s/s_0	Tap No.	\hat{z}/h	s/s_0
01	0	0	25	0.9968	0.5134
02	0	.0344	26	.8874	.5268
03	0	.0739	27	.9719	.5399
04	.0002	.1072	28	.9508	.5533
05	.0110	.1251	29	.5246	.5663
06	.0361	.1423	30	.8939	.5794
07	.0731	.1588	31	.8220	.6048
08	.1195	.1753	32	.7484	.6285
09	.1730	.1918	33	.6450	.6619
10	.2311	.2082	34	.5365	.6969
11	.2911	.2254	35	.4528	.7237
12	.3502	.2433	36	.3502	.7567
13	.4528	.2763	37	.2911	.7746
14	.5365	.3031	38	.2311	.7918
15	.6450	.3381	39	.1730	.8083
16	.7484	.3715	40	.1195	.8247
17	.8220	.3952	41	.0731	.8412
18	.8939	.4206	42	.0361	.8577
19	.9246	.4337	43	.0110	.8749
20	.9508	.4467	44	.0002	.8928
21	.9719	.4601	45	0	.9261
22	.9874	.4731	46	0	.9656
23	.9968	.4865	01	0	1.0000
24	1.0000	.5000			

TABLE 8.- CROSS FORCE AND NORMAL FORCE COEFFICIENTS FOR FLOW-VISUALIZATION TESTS
COMPARED WITH THE CLEAN CONDITION

Configuration	Run No.	Sequence No.	$R_{hb} \times 10^{-6}$	σ	ψ	Test condition	\overline{C}_y	\overline{C}_z
50	118	1	1.2	45	0	Clean	0.5926	-0.8997
51	146	3	↓	45	0	Oil smear	.8071	-.8092
50	118	2	↓	60	0	Clean	-.5006	-1.0368
51	147	3	↓	60	0	Oil smear	-.0029	-.9515
50	120	1	↓	45	10	Clean	.9145	-.9580
51	151	3	↓	↓	↓	Sublimation	.9007	-.9469
		4	↓	↓	↓	Sublimation	.8983	-.9482
		5	↓	↓	↓	Sublimation	.9515	-.9657
51	145	3	↓	↓	↓	Oil smear	.8377	-.8812
51	148	3	↓	↓	↓	Oil dots	.1636	-.6844
		4	↓	↓	↓	Oil dots	.2053	-.6865
50	125	1	1.6	↓	↓	Clean	.8227	-.8134
51	140	3	1.6	↓	↓	Sublimation	.7639	-.8212
		4	1.6	↓	↓	Sublimation	.7627	-.7418
50	120	2	1.2	60	↓	Clean	-.5583	-1.0307
51	152	3	(1.06)	↓	↓	Sublimation	.0526	-1.0847
50	125	2	1.6	↓	↓	Clean	-.0989	-.9170
51	136	5	↓	↓	↓	Sublimation	.0428	-.9246
	137	3	↓	↓	↓	Sublimation	.1962	-.8722
		4	↓	↓	↓	Sublimation	.0845	-.9023
		5	↓	↓	↓	Sublimation	.1210	-.9011
51	142	3	↓	↓	↓	Oil smear	.1007	-.9094
		4	↓	↓	↓	Oil smear	.0598	-.9131
		5	↓	↓	↓	Oil smear	.0342	-.9127
	143	4	↓	↓	↓	Oil smear	.0677	-.9266
	144	3	↓	↓	↓	Oil smear	-.1470	-.9206
51	149	3	↓	↓	↓	Oil dots	.5378	-.9496
		4	↓	↓	↓	Oil dots	.5487	-.9437
50	125	3	↓	75	↓	Clean	.6604	-.8912
51	150	1	↓	75	↓	Oil smear	.5226	-.8223
		2	↓	75	↓	Oil smear	.5208	-.8337
60	158	3	1.2	45	0	Clean	-.0292	-.6130
61	162	7	1.2	45	↓	Oil smear	-.0354	-.5546
	164	3	1.2	45	↓	Oil dots	.0242	-.4890
61		4	1.2	45	↓	Oil dots	.0386	-.4825
60	157	5	1.6	60	↓	Clean	.1754	-.6928
61	163	3	1.6	60	↓	Oil smear	-.0191	-.6077
		4	1.6	60	↓	Oil smear	.0480	-.5850
110	266	10	1.2	35	↓	Clean	-.2412	-.5848
111	278	5	↓	35	↓	Oil smear	-.3063	-.5883
110	266	12	↓	40	↓	Clean	.2940	-.6784
111	279	3	↓	40	↓	Oil smear	.3313	-.7135
		4	↓	40	↓	Oil smear	.3325	-.7095

ORIGINAL PAGE IS
OF POOR QUALITY

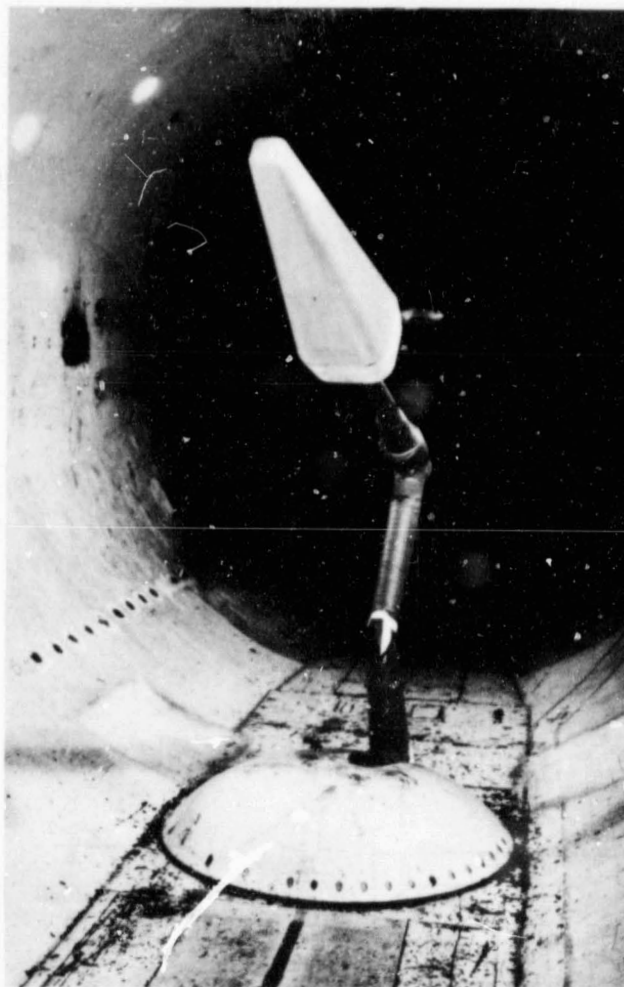


Figure 1.- Model installed in 12-ft wind tunnel.

ORIGINAL PAGE IS
OF POOR QUALITY

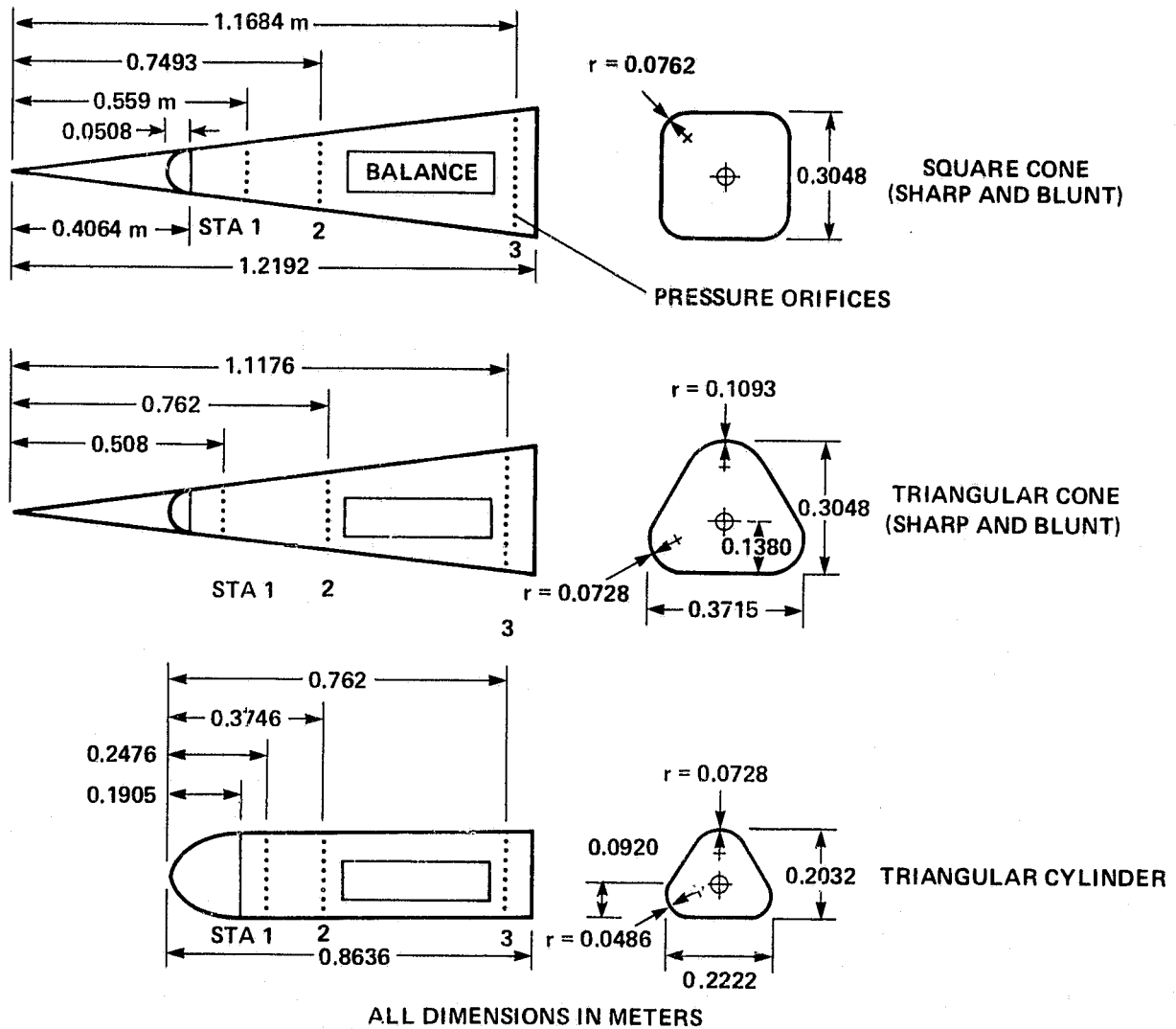


Figure 2.- Model geometry and dimensions.

ORIGINAL PAGE IS
OF POOR QUALITY

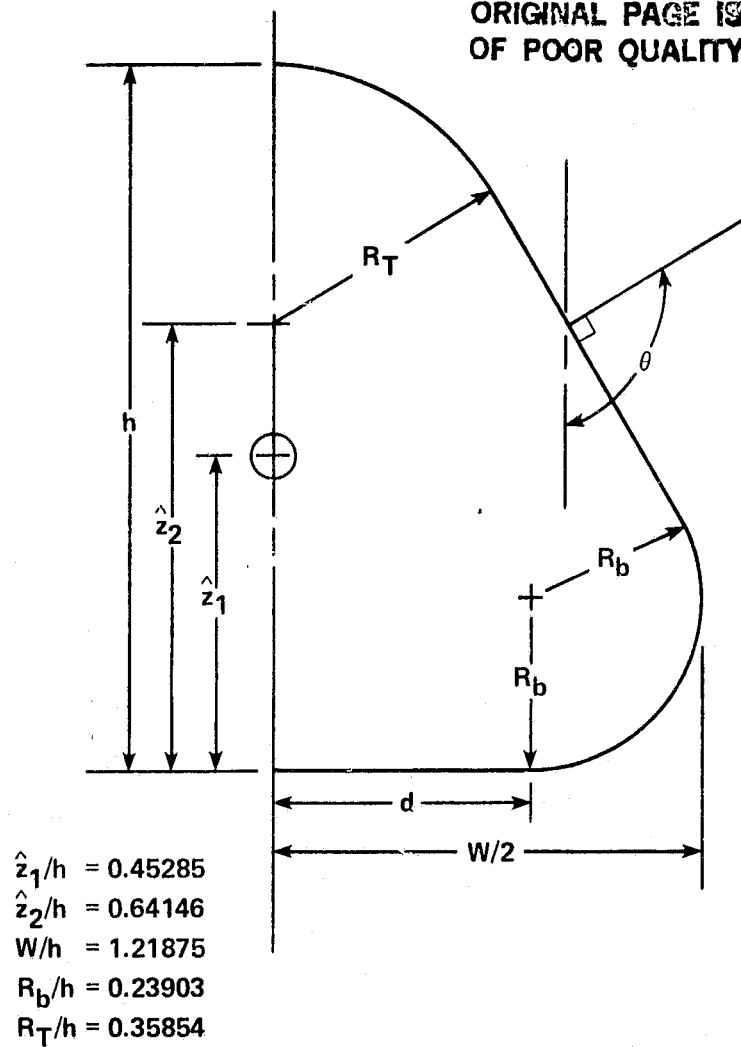
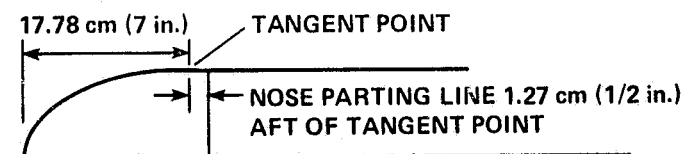
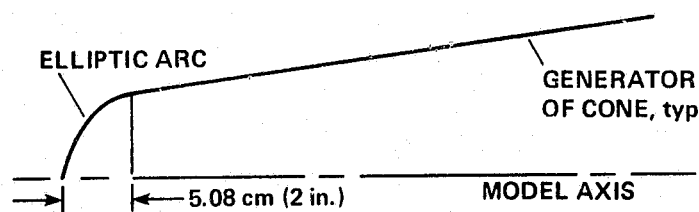


Figure 3.- Geometry of triangular cross section.



(a) Cylinder



(b) Cones

Figure 4.- Blunt-nose fairings.

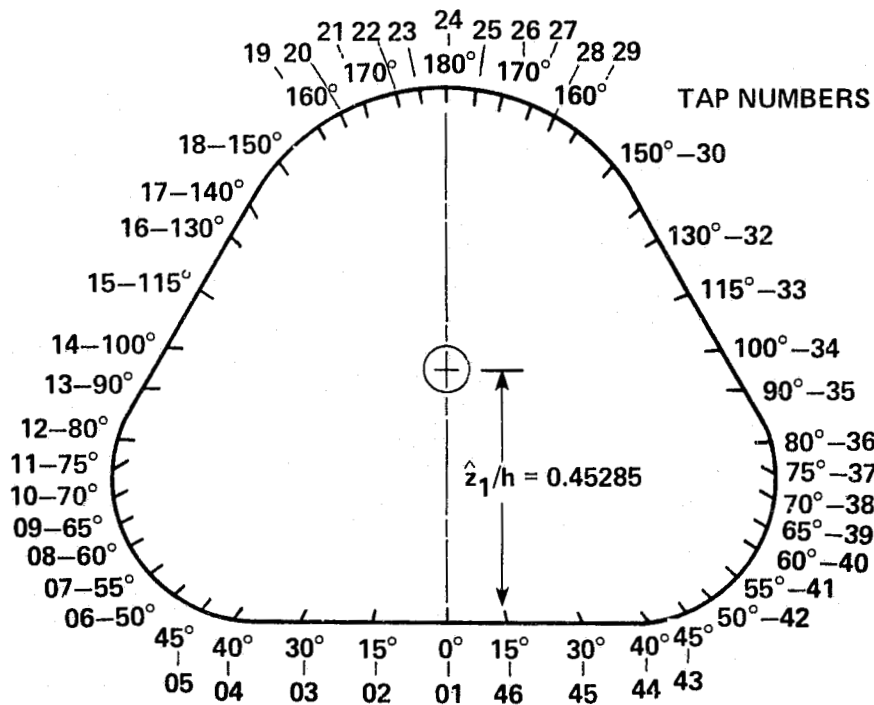
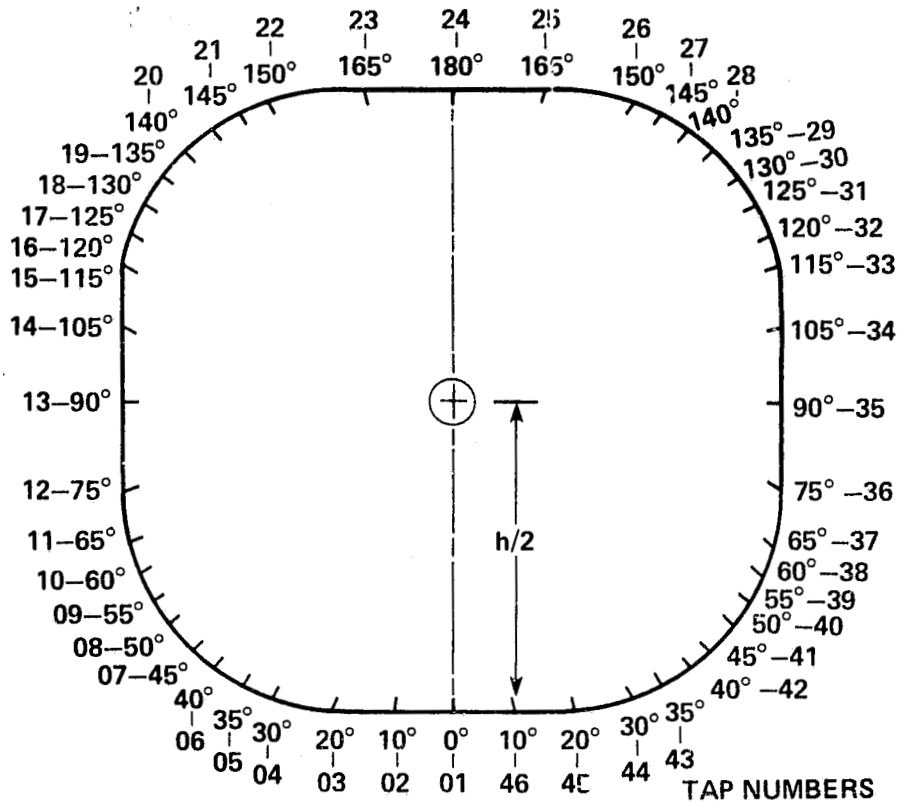


Figure 5.- Tap numbers and locations (view looking forward); typical of each station and model.

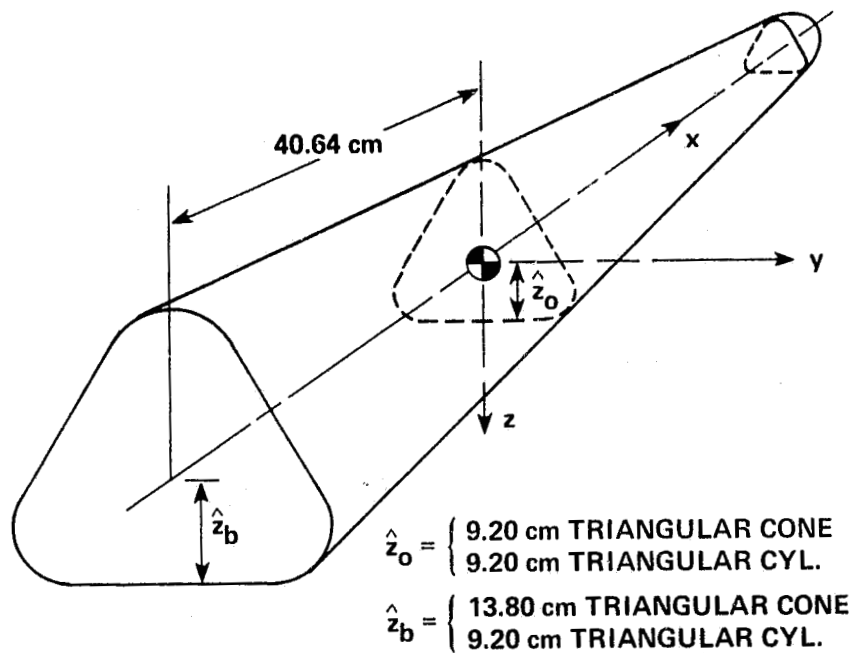


Figure 6.- Definition and location of body axes.

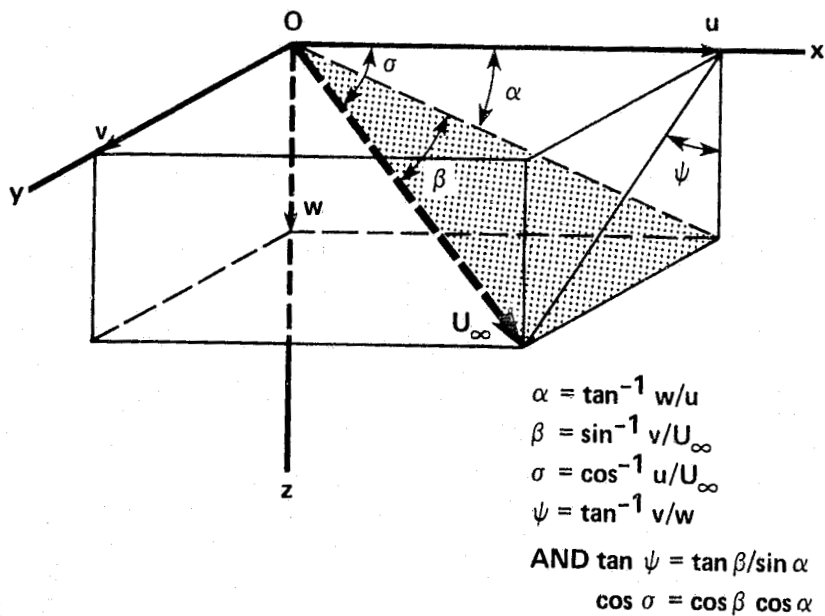


Figure 7.- Definition of position angles.

ORIGINAL PAGE IS
OF POOR QUALITY

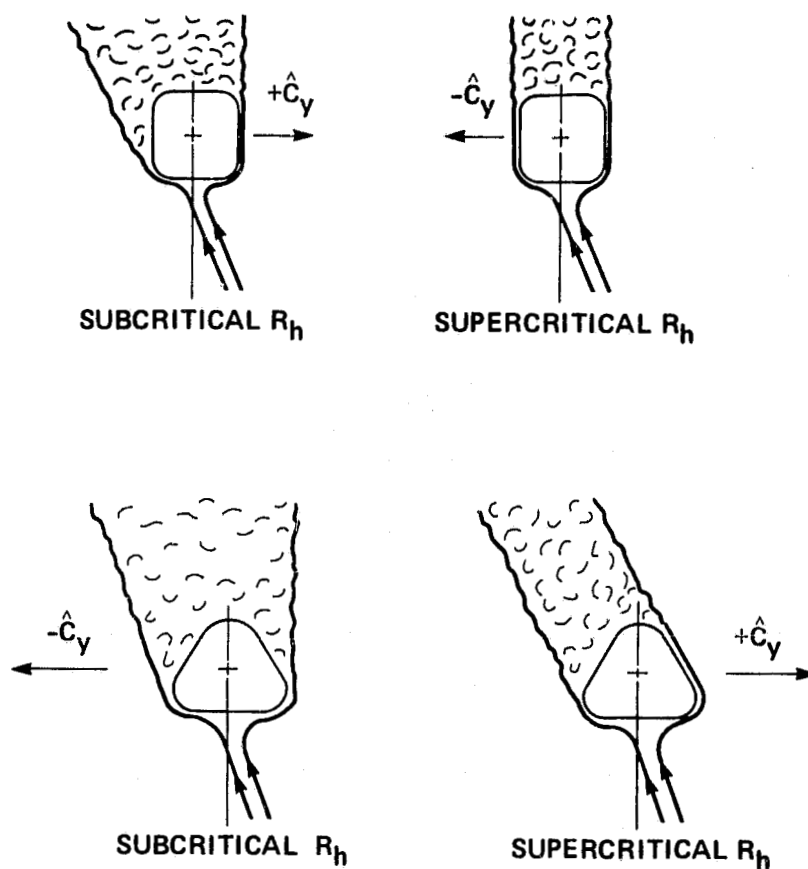


Figure 8.- Two-dimensional flow characteristics on cylinders with noncircular cross sections.

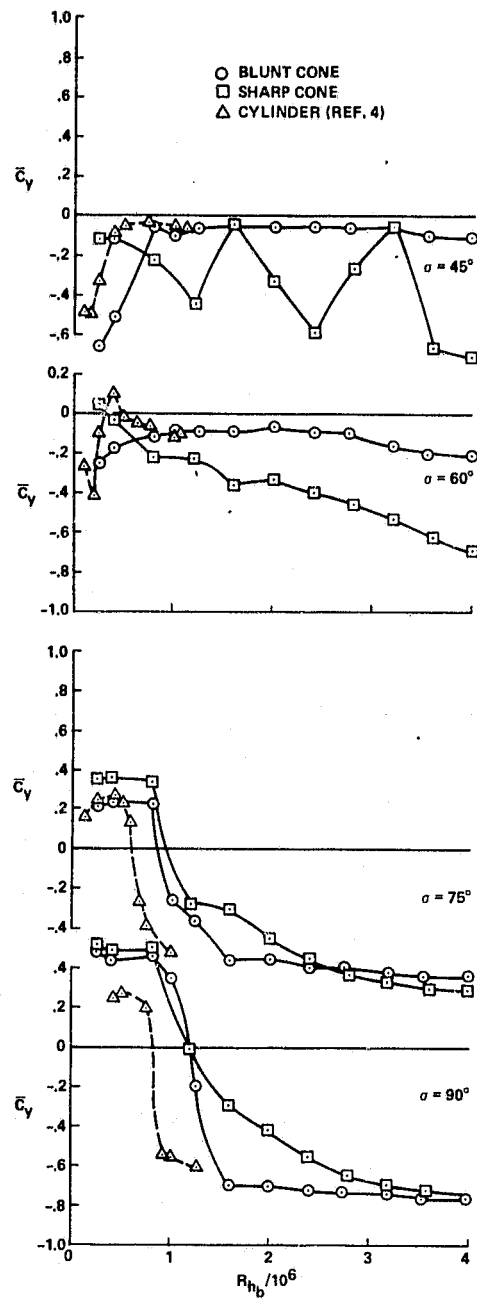


Figure 9.- Side-force coefficients for bodies with square cross sections: $\psi = 10^\circ$.

ORIGINAL PAGE IS
OF POOR QUALITY

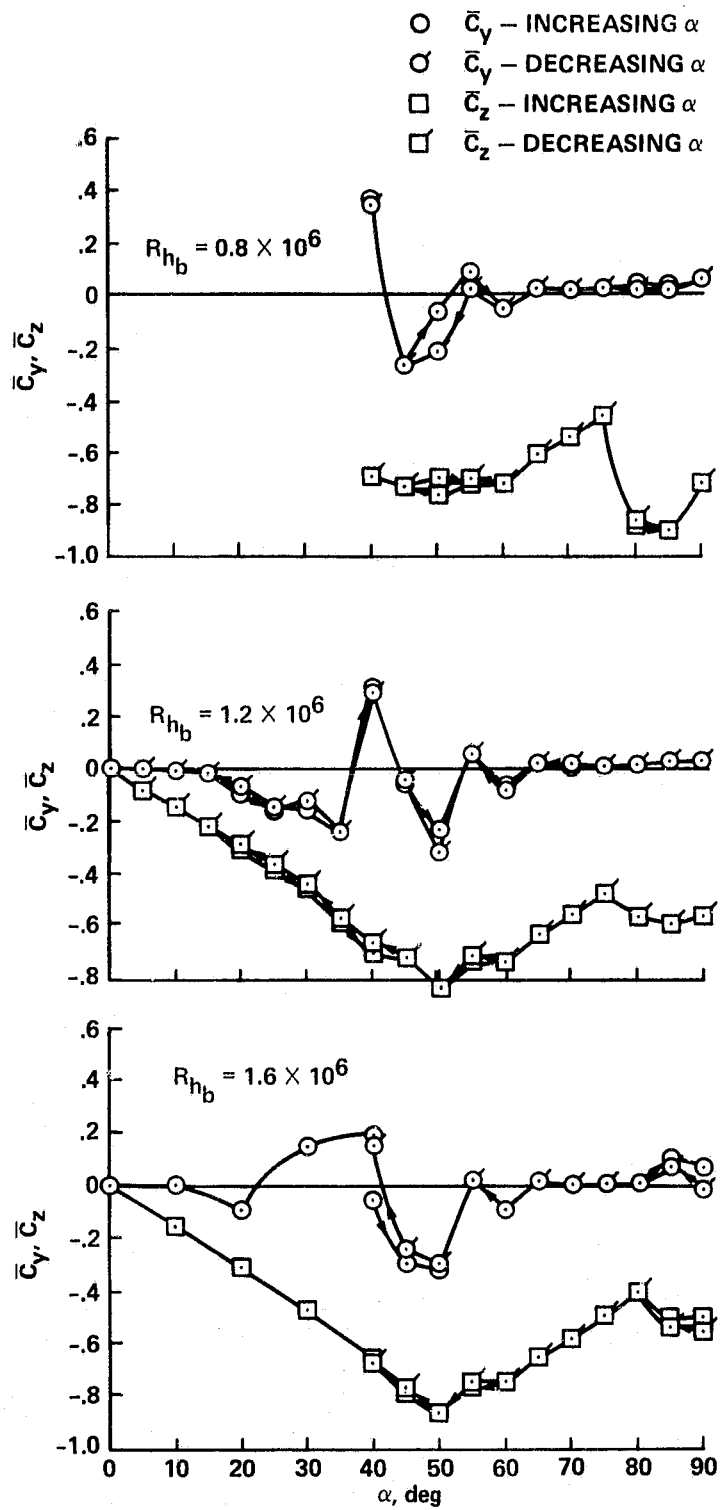


Figure 10.- Side- and normal-force coefficients for sharp square cone: $\psi = 0^\circ$.

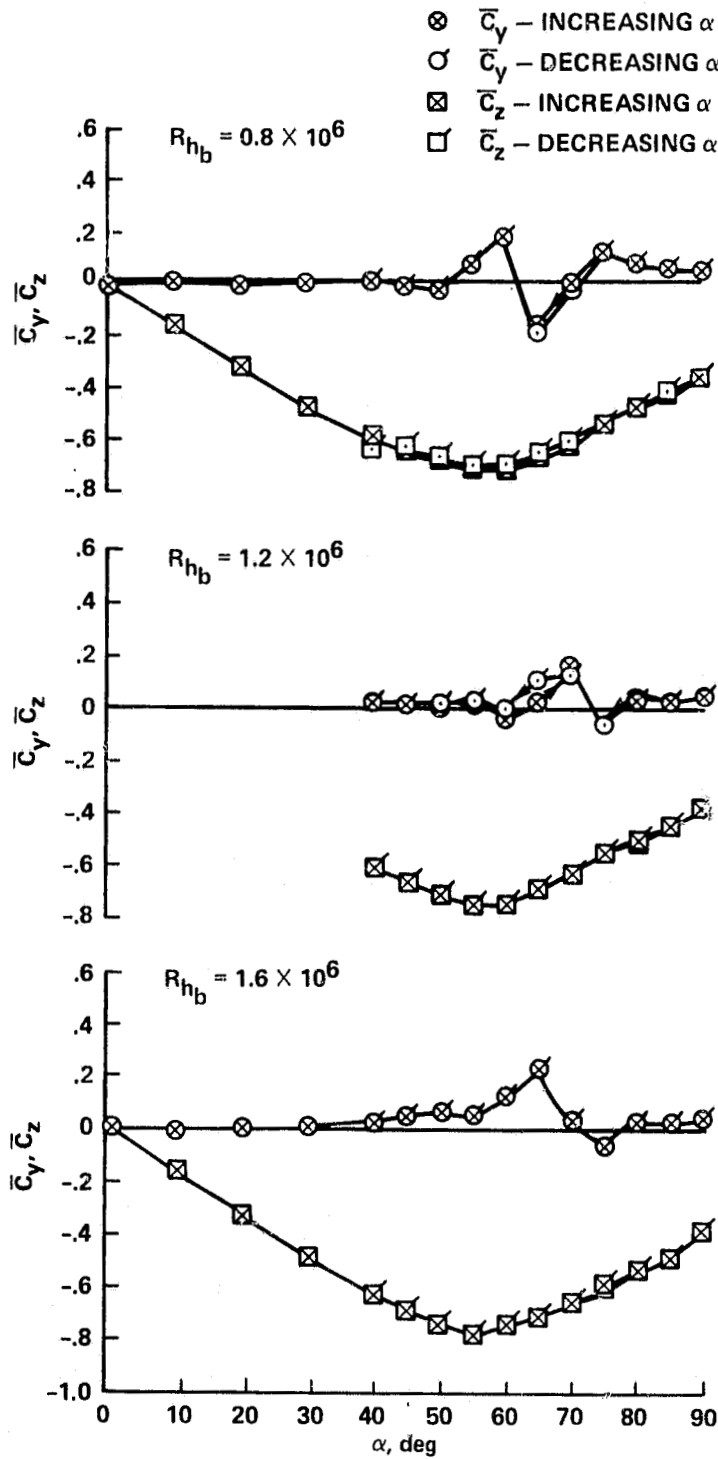


Figure 11.- Side- and normal-force coefficients for blunt square cone: $\psi = 0^\circ$.

ORIGINAL PAGE IS
OF POOR QUALITY

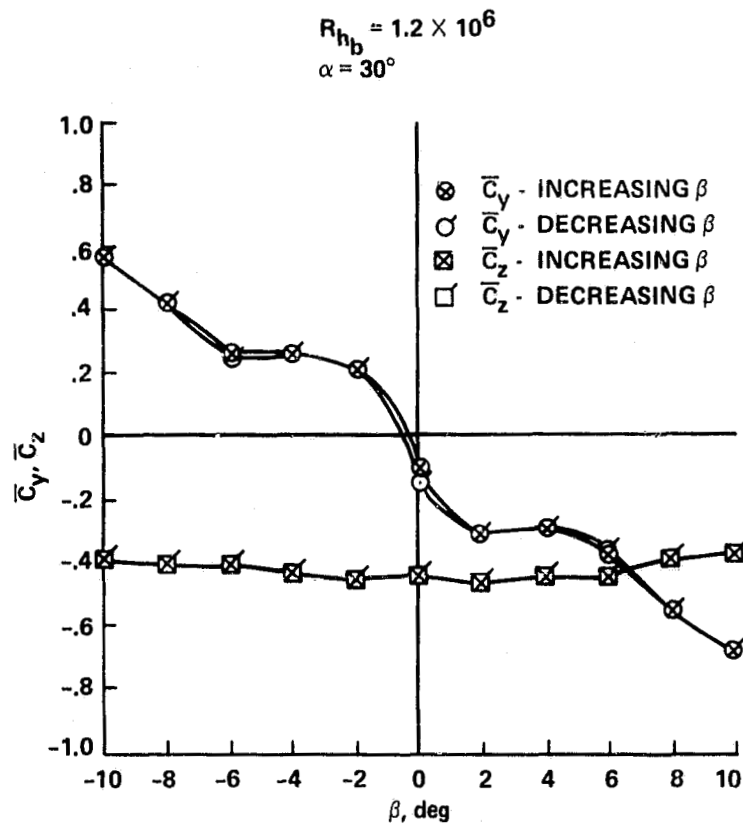


Figure 12.- β -sweep for sharp square cone: $\alpha = 30^\circ$, $R_{hb} = 1.2 \times 10^6$.

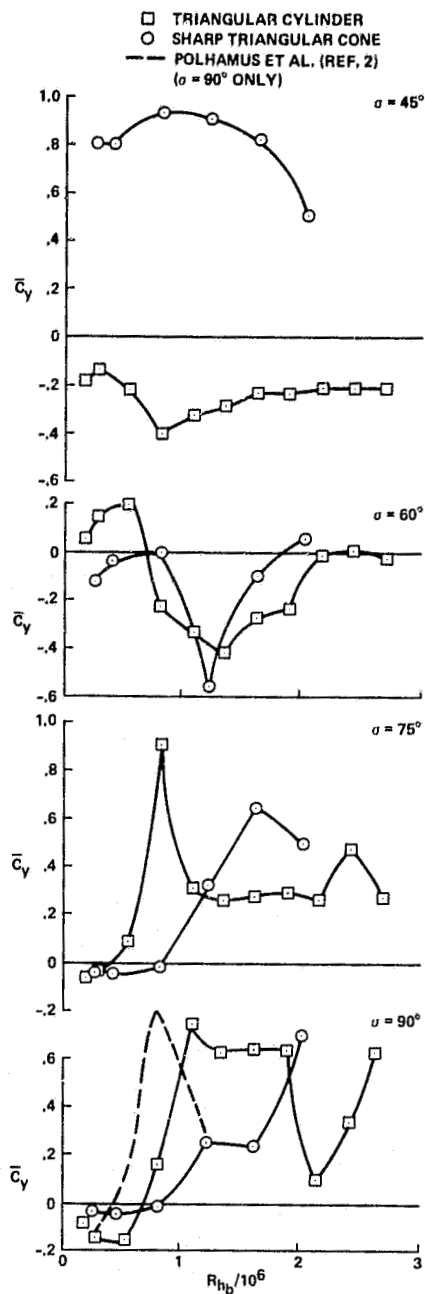


Figure 13.- Side-force coefficient for triangular cylinder and sharp triangular cone:
 $\psi = 10^\circ$.

ORIGINAL PAGE IS
OF POOR QUALITY

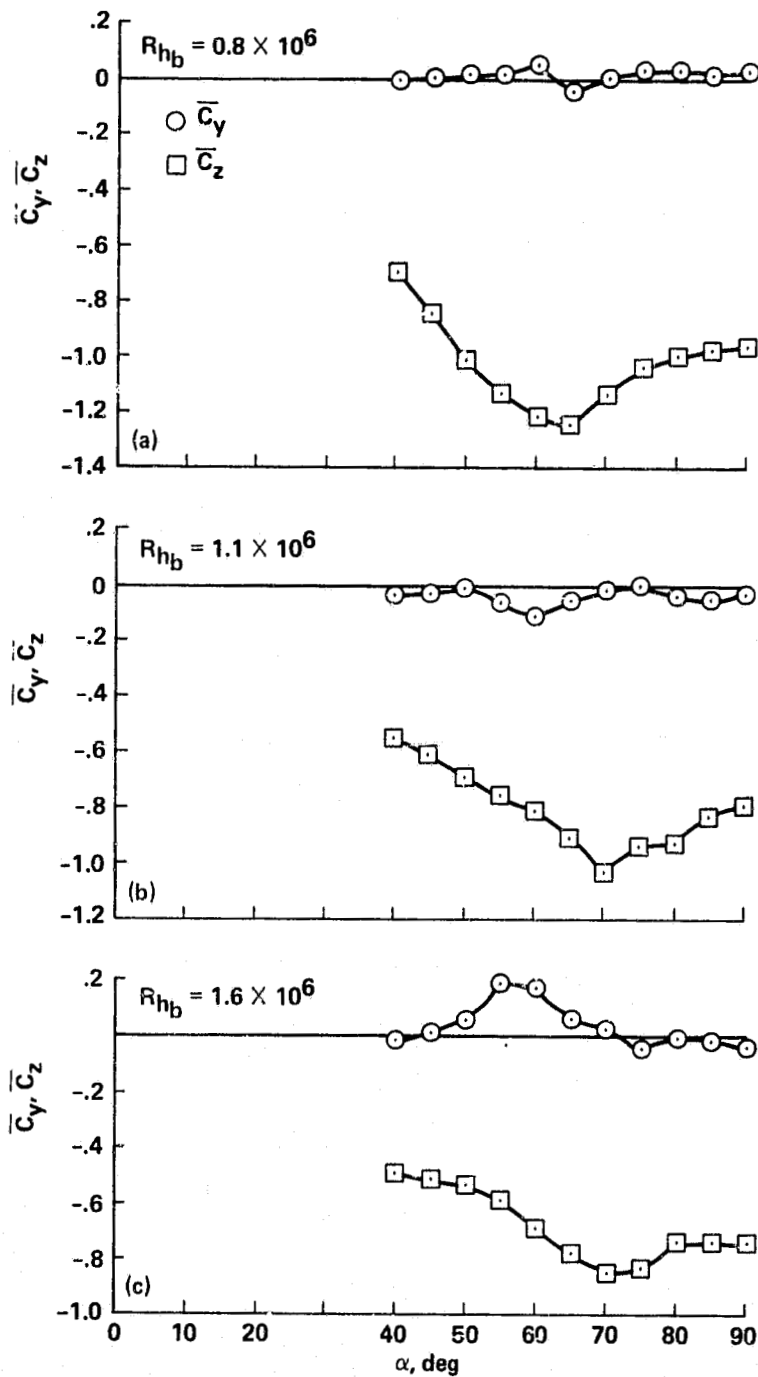
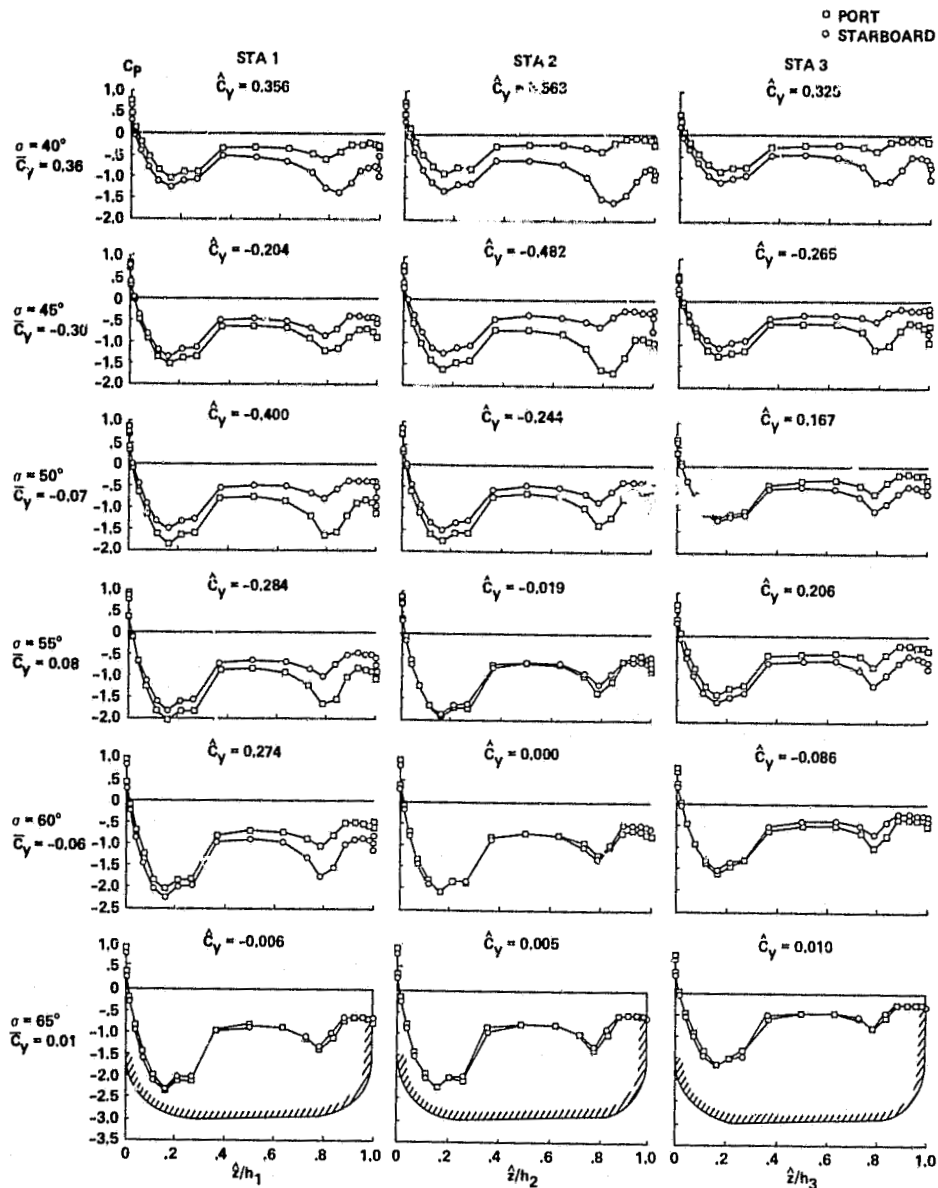


Figure 14.- Side- and normal-force coefficients for blunt triangular cone: $\psi = 0^\circ$.

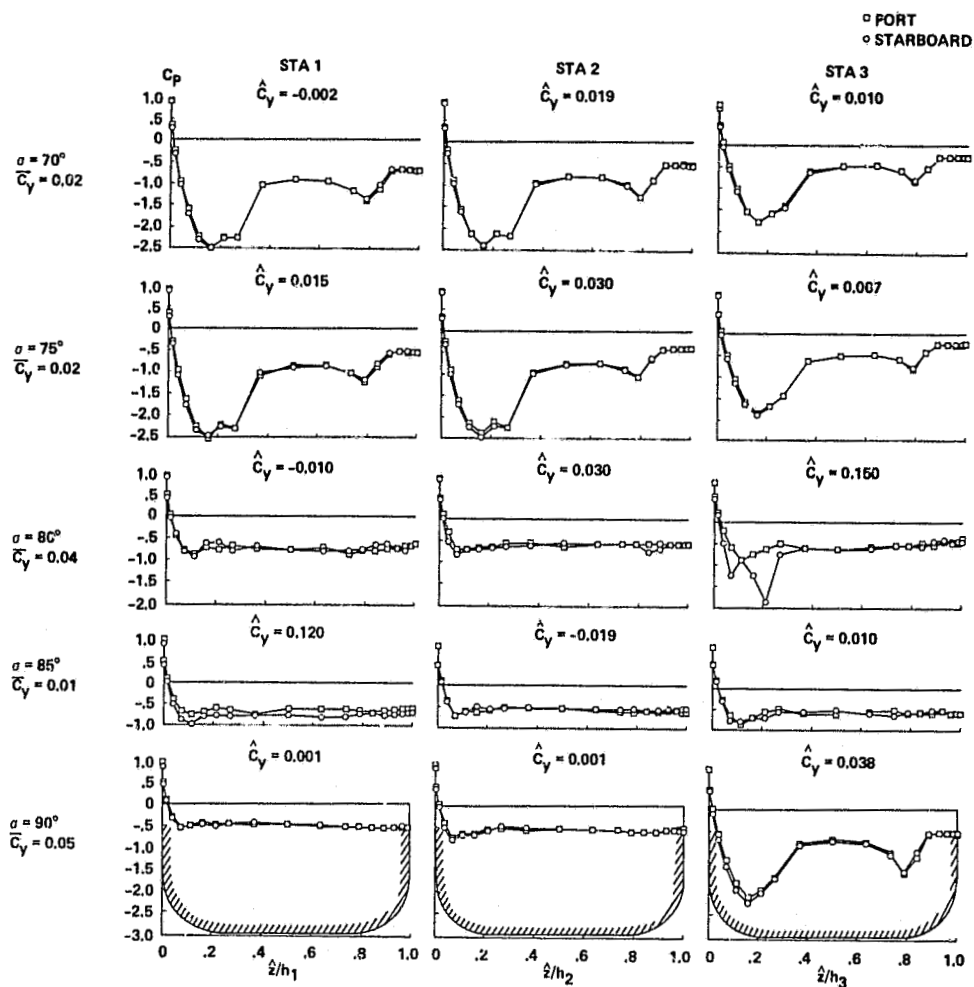
ORIGINAL PAGE IS
OF POOR QUALITY



(a) $\sigma = 40^\circ, 45^\circ, 50^\circ, 55^\circ, 60^\circ$, and 65° .

Figure 15.- Pressure distribution for the sharp square cone at various angles of attack: $R_{hb} = 0.8 \times 10^6$, $\psi = 0^\circ$.

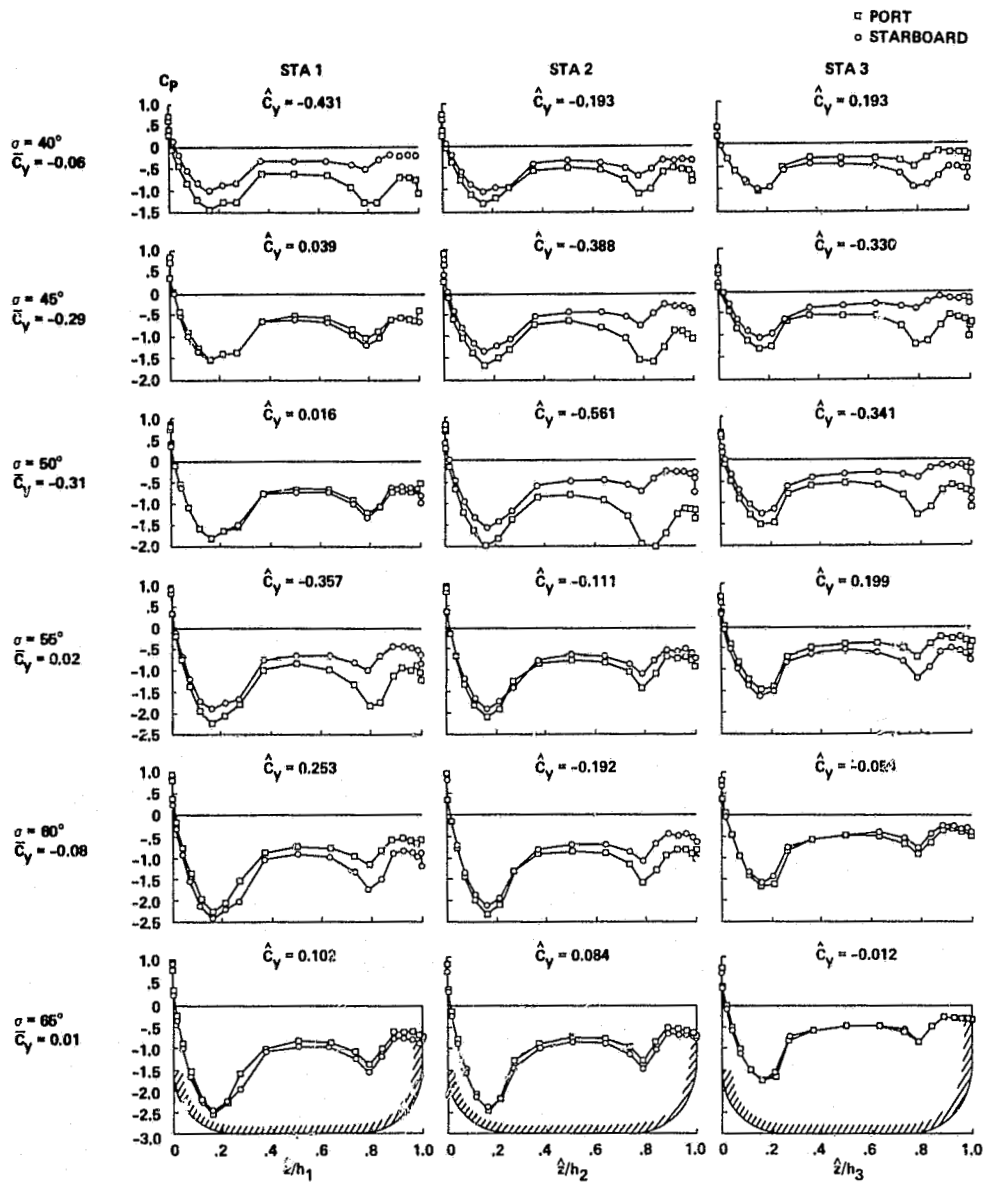
ORIGINAL PAGE IS
OF POOR QUALITY



(b) $\sigma = 70^\circ, 75^\circ, 80^\circ, 85^\circ$, and 90° .

Figure 15.- Concluded.

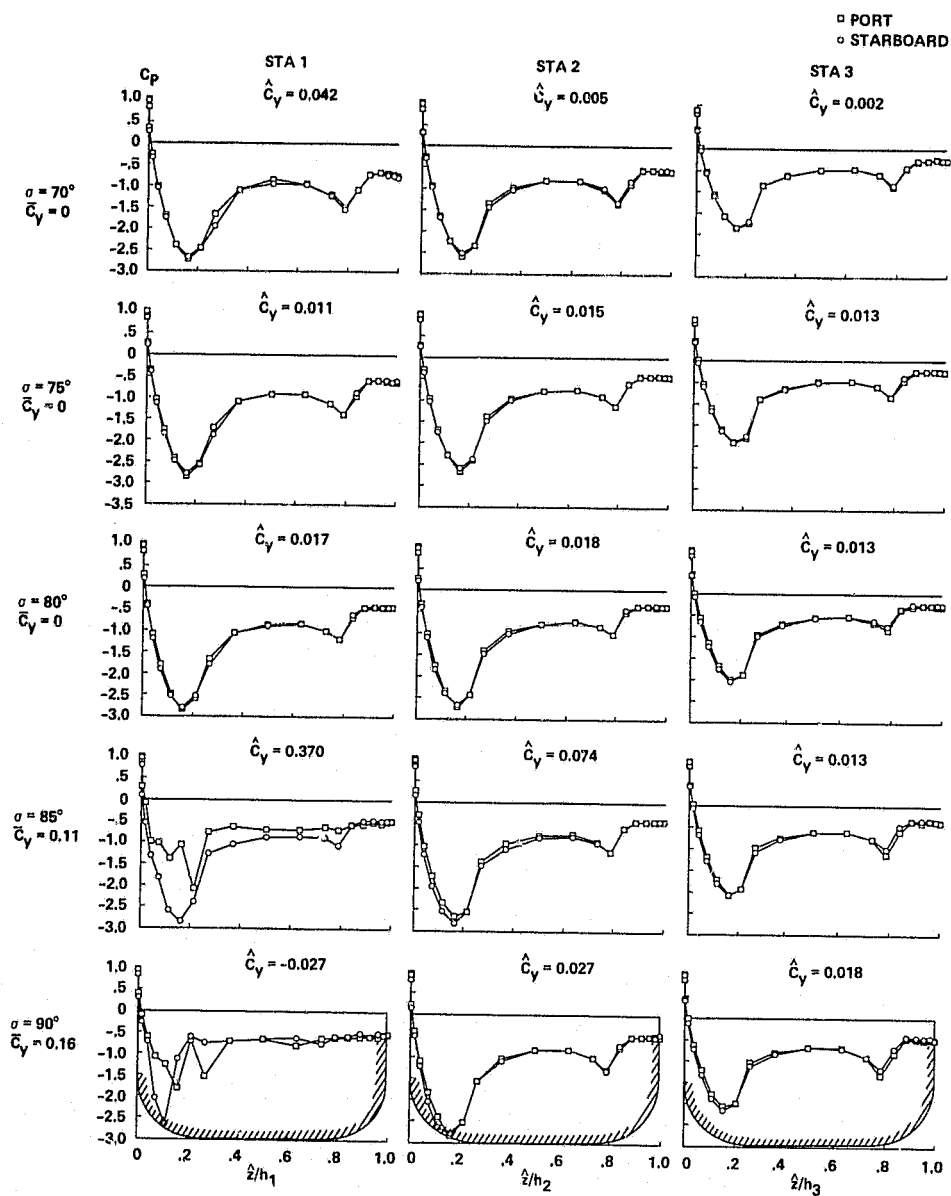
ORIGINAL PAGE IS
OF POOR QUALITY



(a) $\sigma = 40^\circ, 45^\circ, 50^\circ, 55^\circ, 60^\circ$, and 65° .

Figure 16.- Pressure distributions for the sharp square cone at various angles of attack: $R_{hb} = 1.6 \times 10^6$, $\psi = 0^\circ$.

ORIGINAL PAGE IS
OF POOR QUALITY



(b) $\sigma = 70^\circ, 75^\circ, 80^\circ, 85^\circ, \text{ and } 90^\circ$.

Figure 16.- Concluded.

ORIGINAL PAGE IS
OF POOR QUALITY

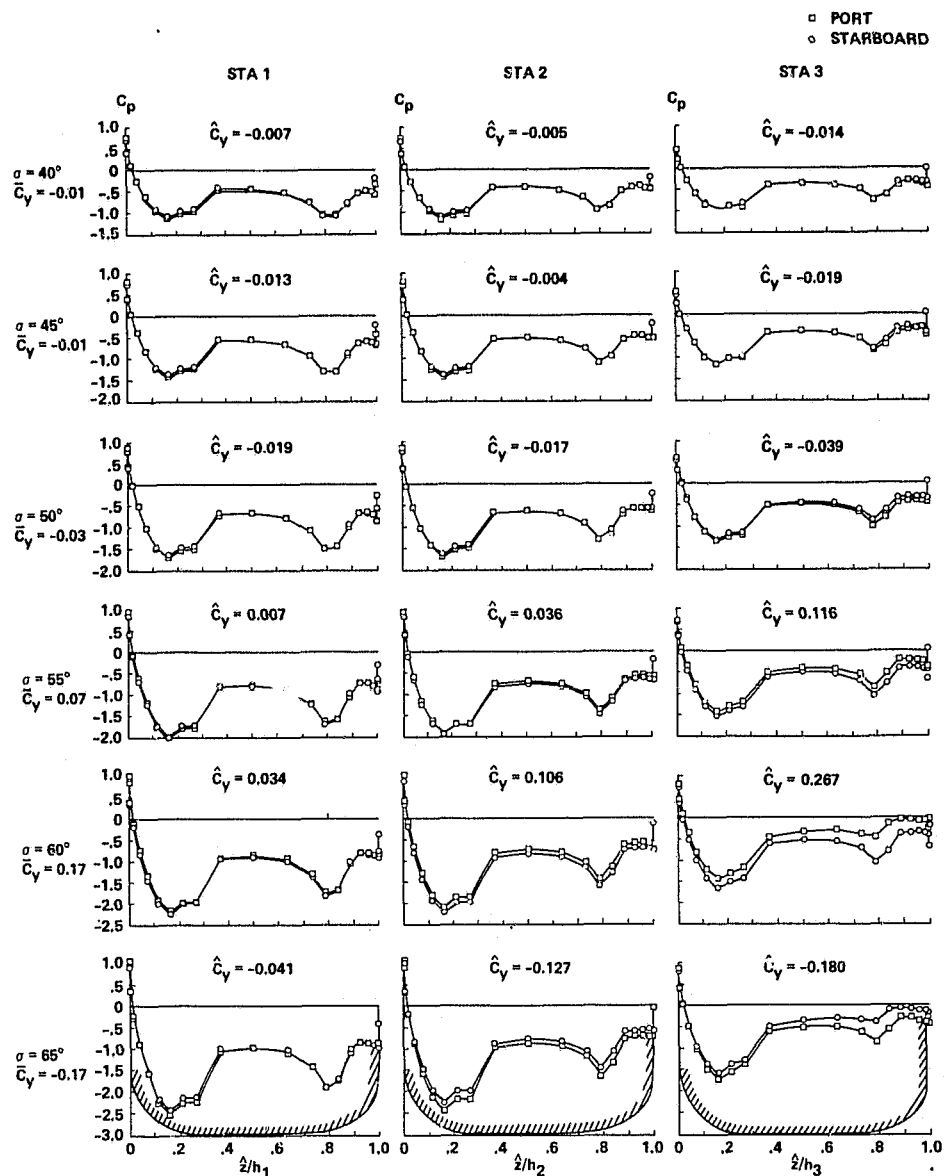
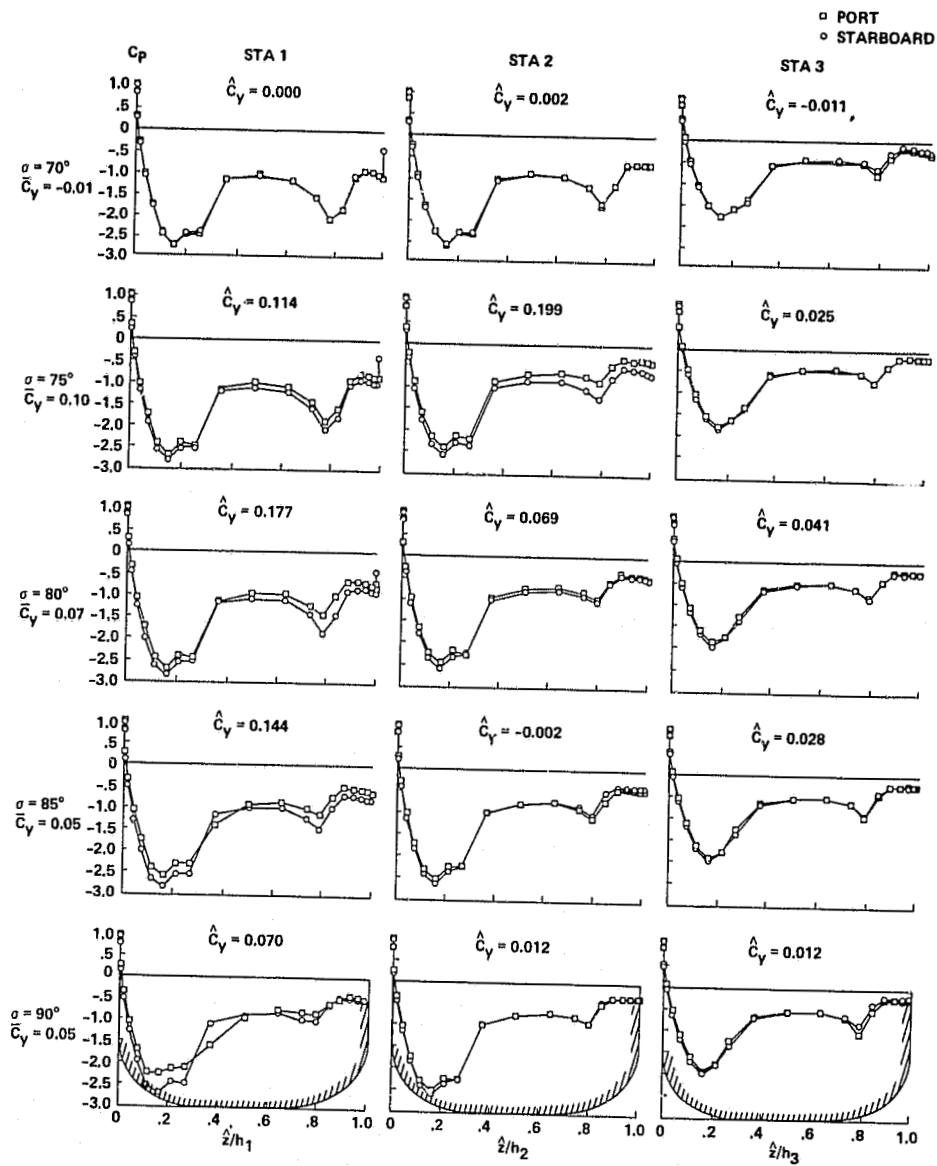


Figure 17.- Pressure distributions for the blunt square cone at various angles of attack: $R_{hb} = 0.8 \times 10^6$, $\psi = 0^\circ$.

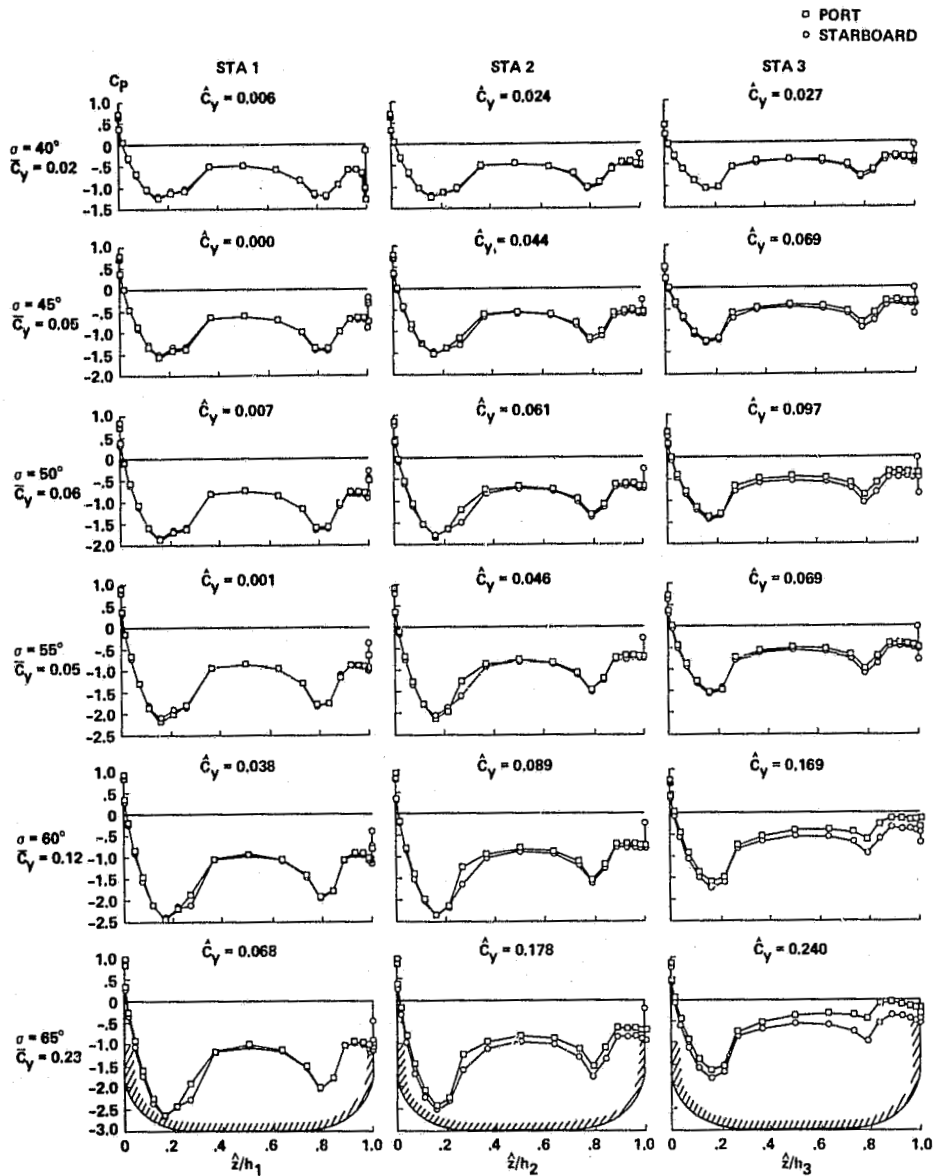
ORIGINAL PAGE IS
OF POOR QUALITY



(b) $\sigma = 70^\circ, 75^\circ, 80^\circ, 85^\circ$, and 90° .

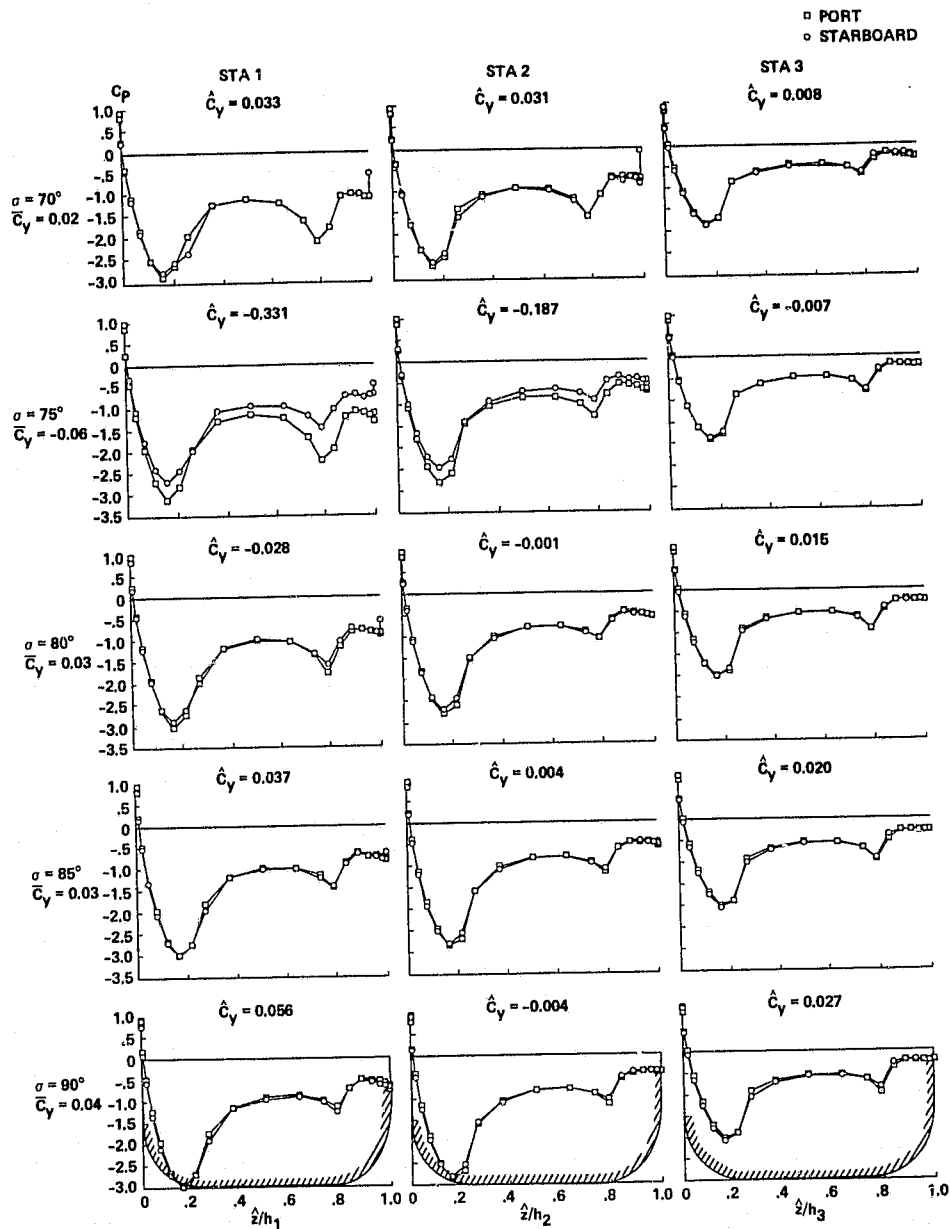
Figure 17.- Concluded.

ORIGINAL PAGE IS
OF POOR QUALITY



(a) $\sigma = 40^\circ, 45^\circ, 50^\circ, 55^\circ, 60^\circ$, and 65° .

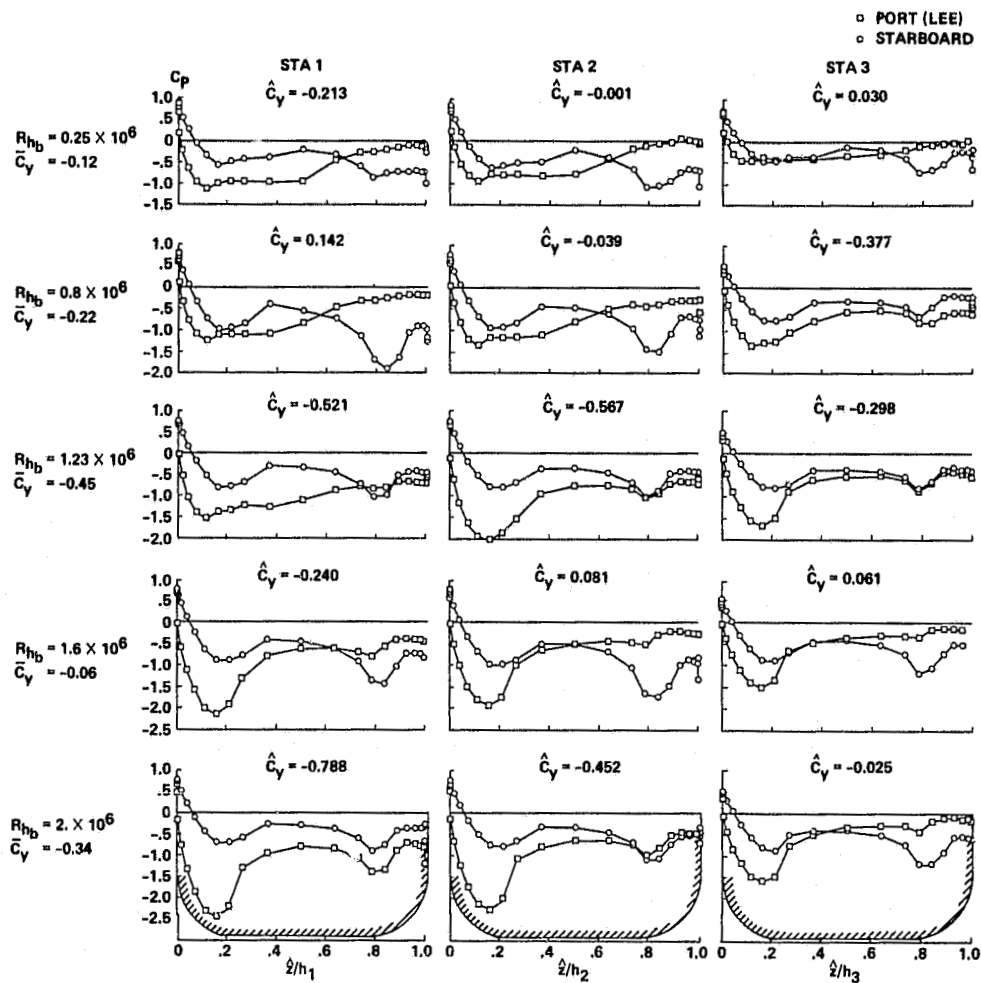
Figure 18.- Pressure distributions for the blunt square cone at various angles of attack: $R_{hb} = 1.6 \times 10^6$, $\psi = 0^\circ$.



(b) $\sigma = 70^\circ, 75^\circ, 80^\circ, 85^\circ, \text{ and } 90^\circ$.

Figure 18.- Concluded.

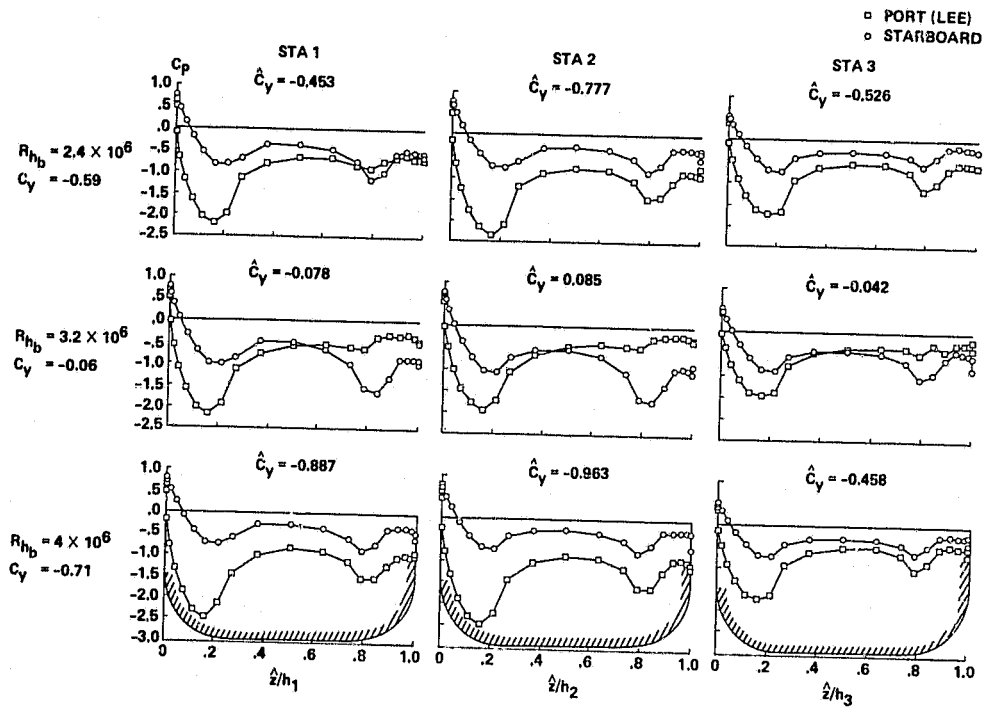
ORIGINAL PAGE IS
OF POOR QUALITY



(a) $R_{hb} = 0.25, 0.8, 1.23, 1.6, \text{ and } 2 (\times 10^6)$.

Figure 19.- Pressure distributions for the sharp square cone at various Reynolds numbers: $\sigma = 45^\circ$, $\psi = 10^\circ$.

ORIGINAL PAGE IS
OF POOR QUALITY



(b) $R_{hb} = 2.4, 3.2, \text{ and } 4 (\times 10^6)$.

Figure 19.- Concluded.

ORIGINAL PAGE 13
OF POOR QUALITY

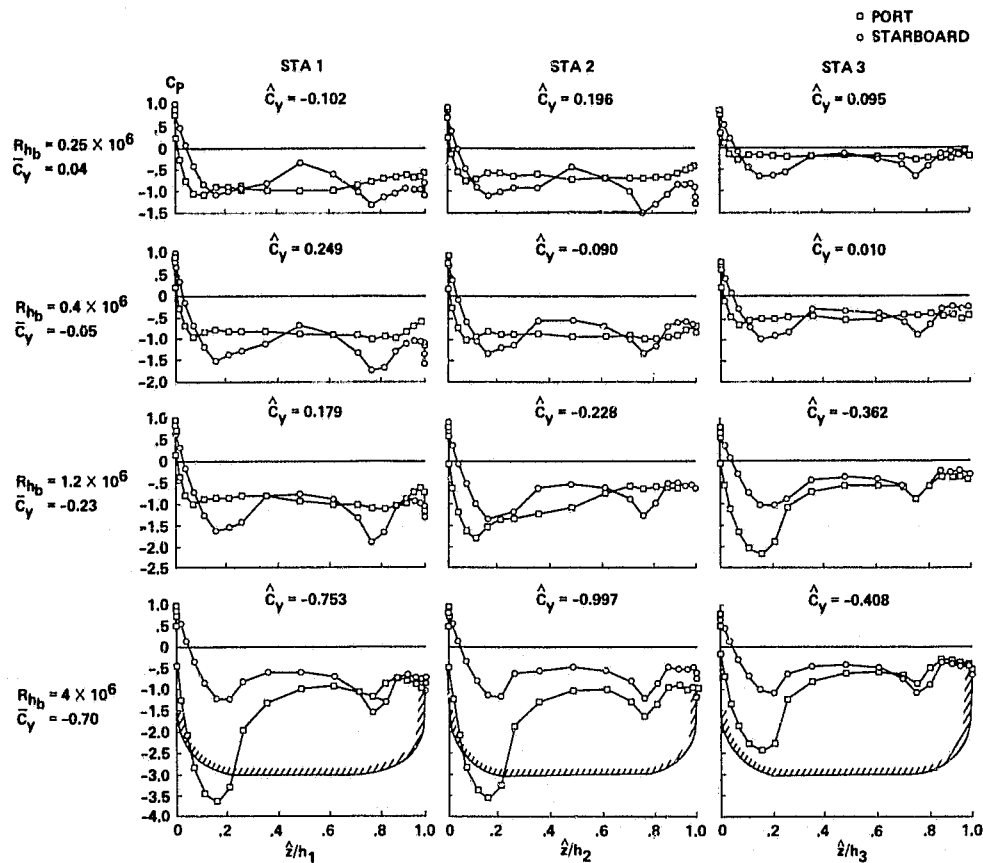


Figure 20.- Pressure distributions for the sharp square cone for various Reynolds numbers: $\sigma = 60^\circ$, $\psi = 10^\circ$.

ORIGINAL PAGE 13
OF POOR QUALITY

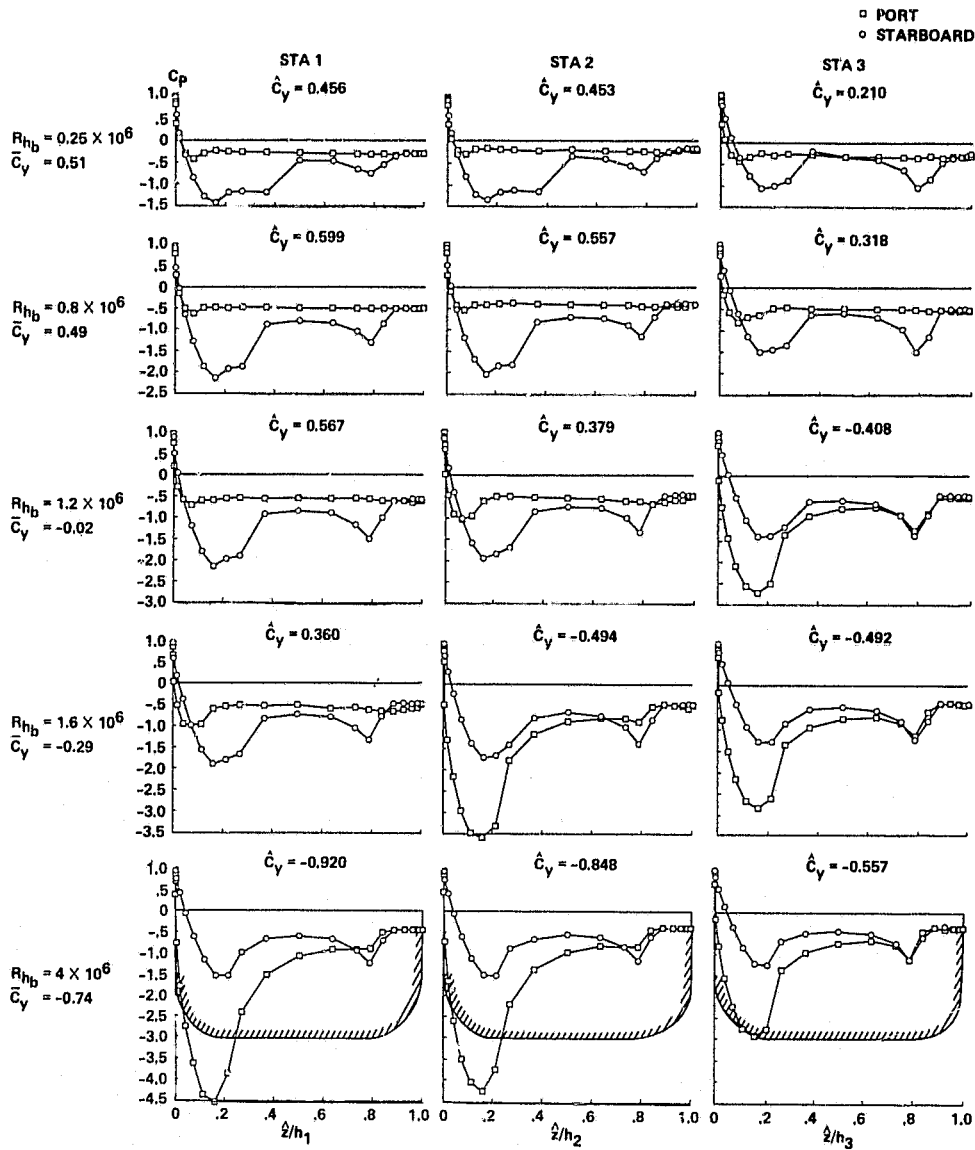


Figure 21.- Pressure distributions for the sharp square cone for various Reynolds numbers: $\sigma = 90^\circ$, $\psi = 10^\circ$.

ORIGINAL PAGE IS
OF POOR QUALITY

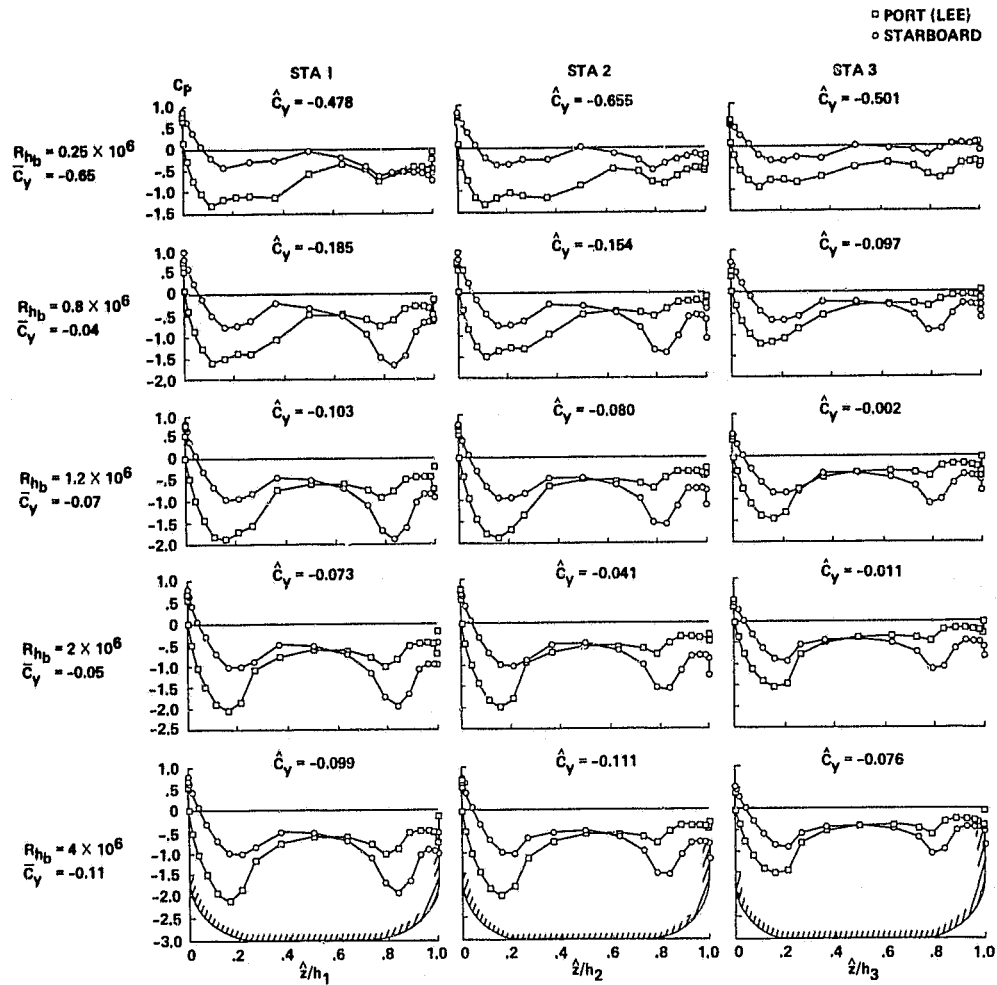


Figure 22.- Pressure distributions for the blunt square cone for various Reynolds numbers; $\sigma = 45^\circ$, $\psi = 10^\circ$.

ORIGINAL PAGE IS
OF POOR QUALITY

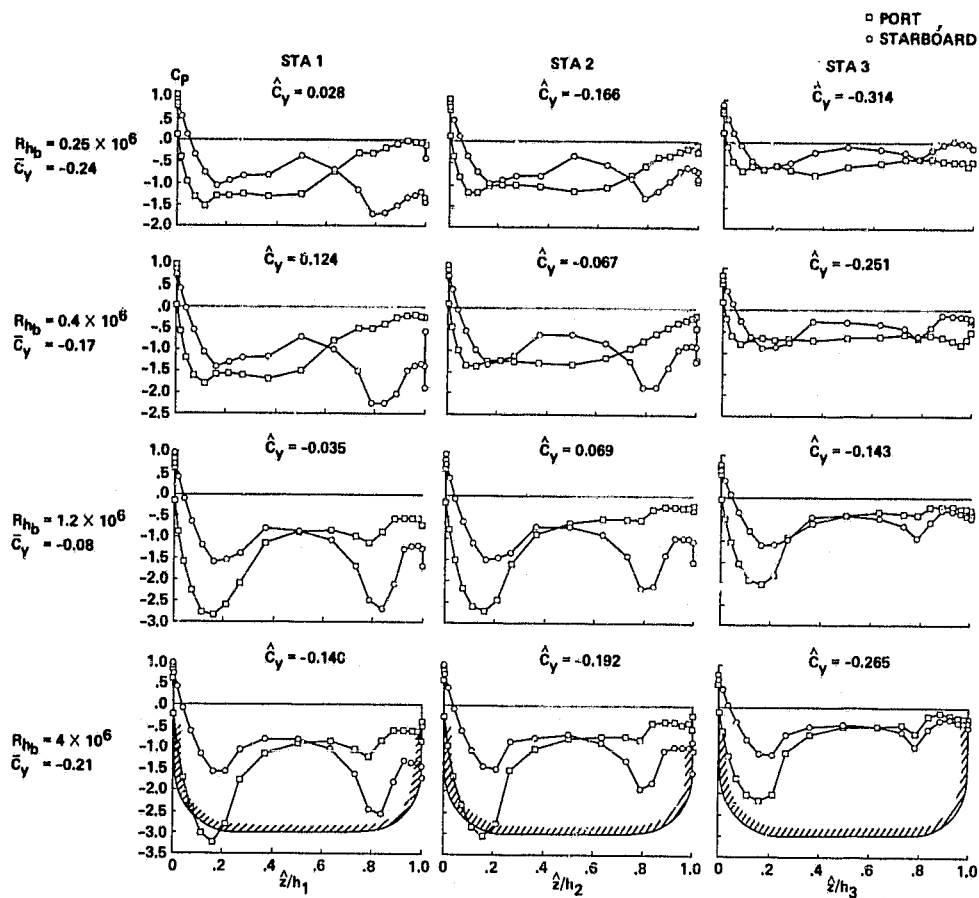
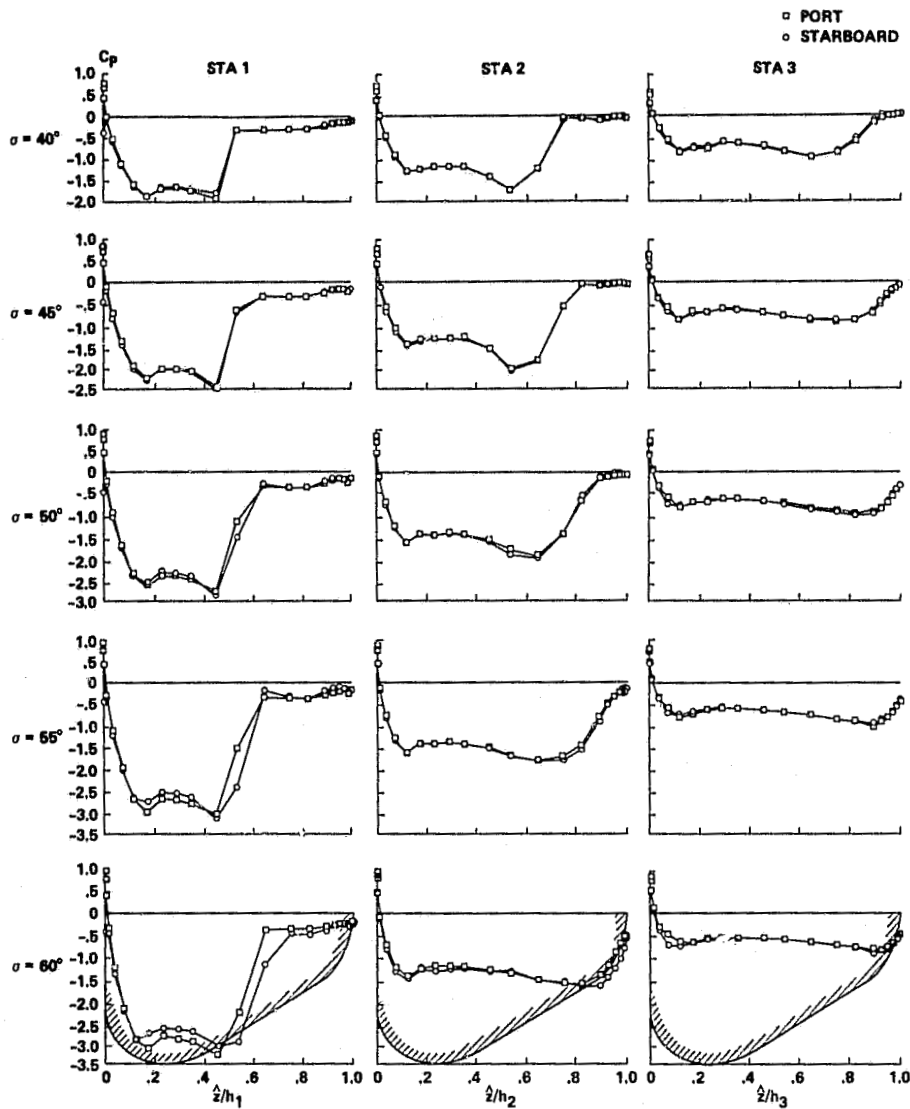


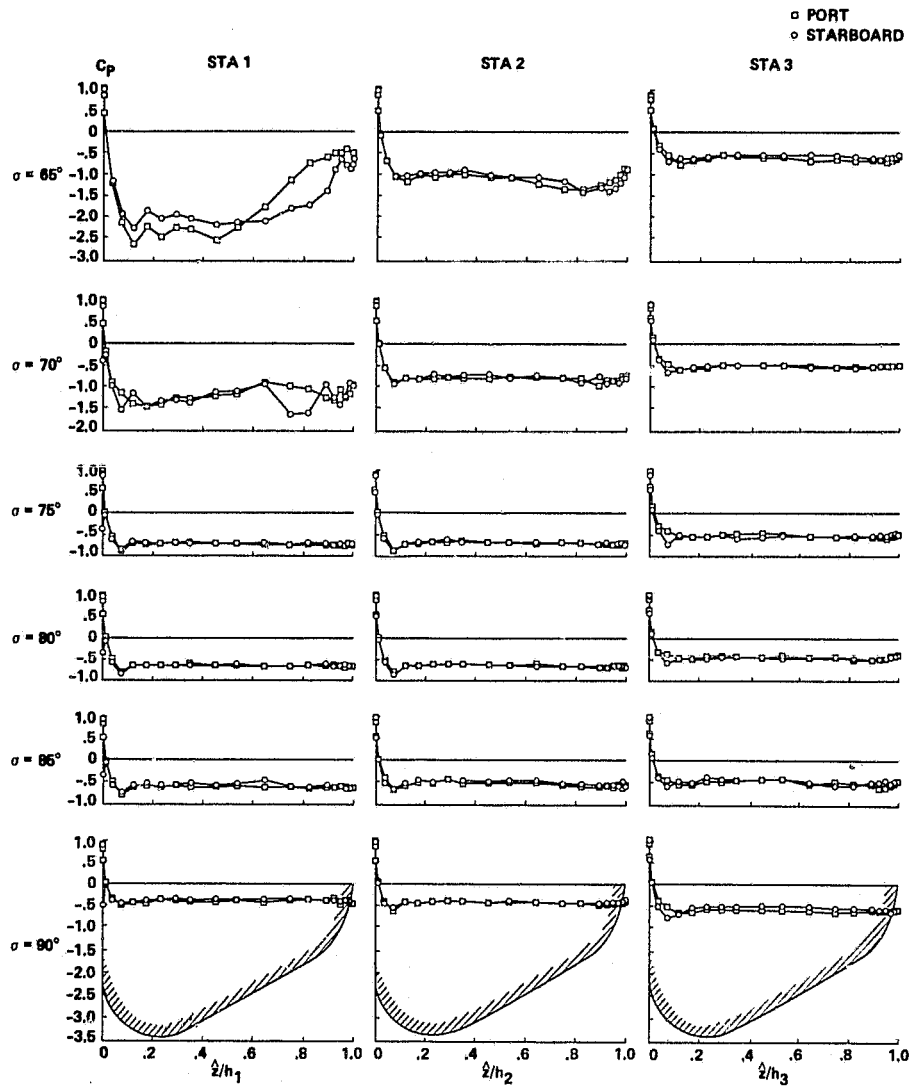
Figure 23.- Pressure distributions for the blunt square cone for various Reynolds numbers: $\sigma = 60^\circ$, $\psi = 10^\circ$.

ORIGINAL PAGE IS
OF POOR QUALITY



(a) $\sigma = 40^\circ, 45^\circ, 50^\circ, 55^\circ, \text{ and } 60^\circ$.

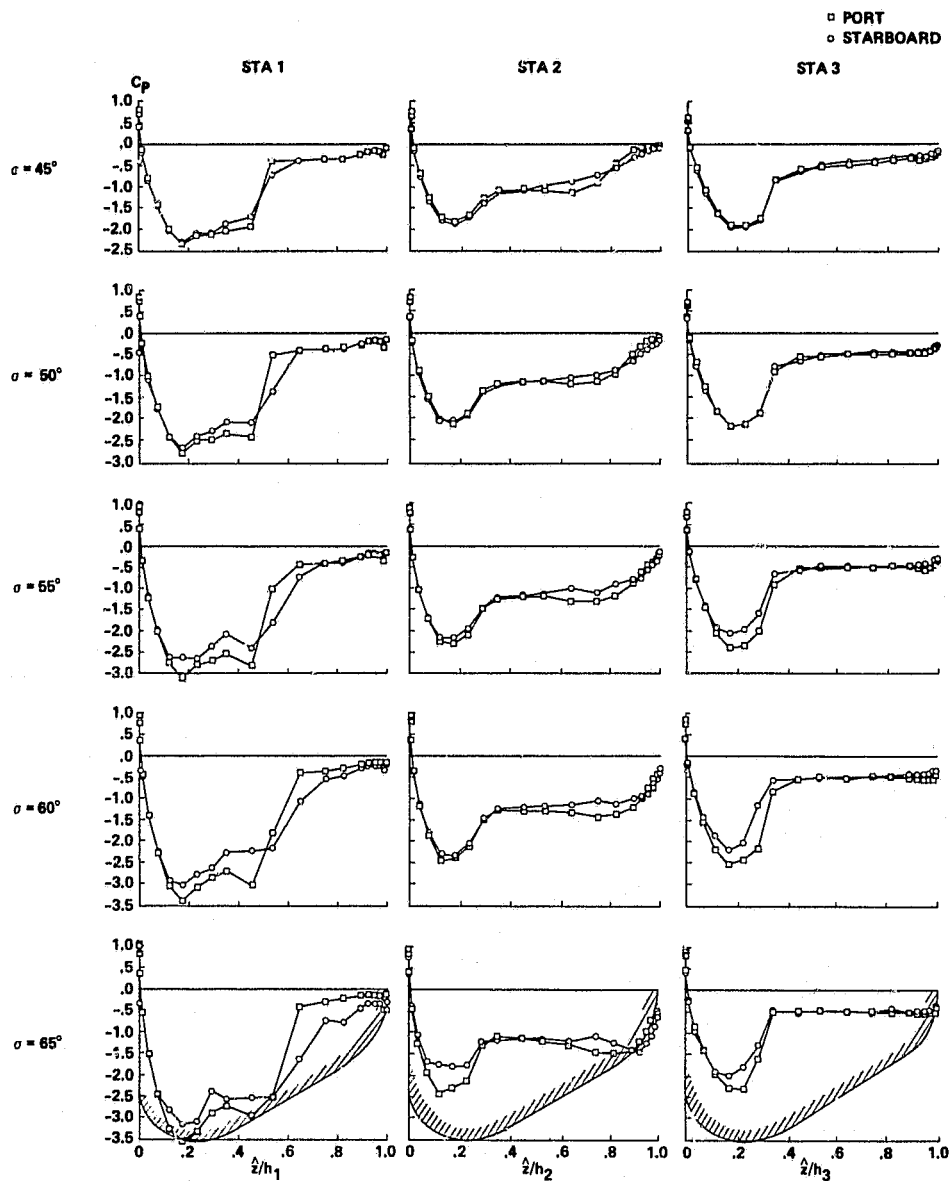
Figure 24.- Pressure distributions for the blunt triangular cone at various angles of attack: $R_{hp} = 0.76 \times 10^6$, $\psi = 0^\circ$.



(b) $\sigma = 65^\circ, 70^\circ, 75^\circ, 80^\circ, 85^\circ, \text{ and } 90^\circ$.

Figure 24.- Concluded.

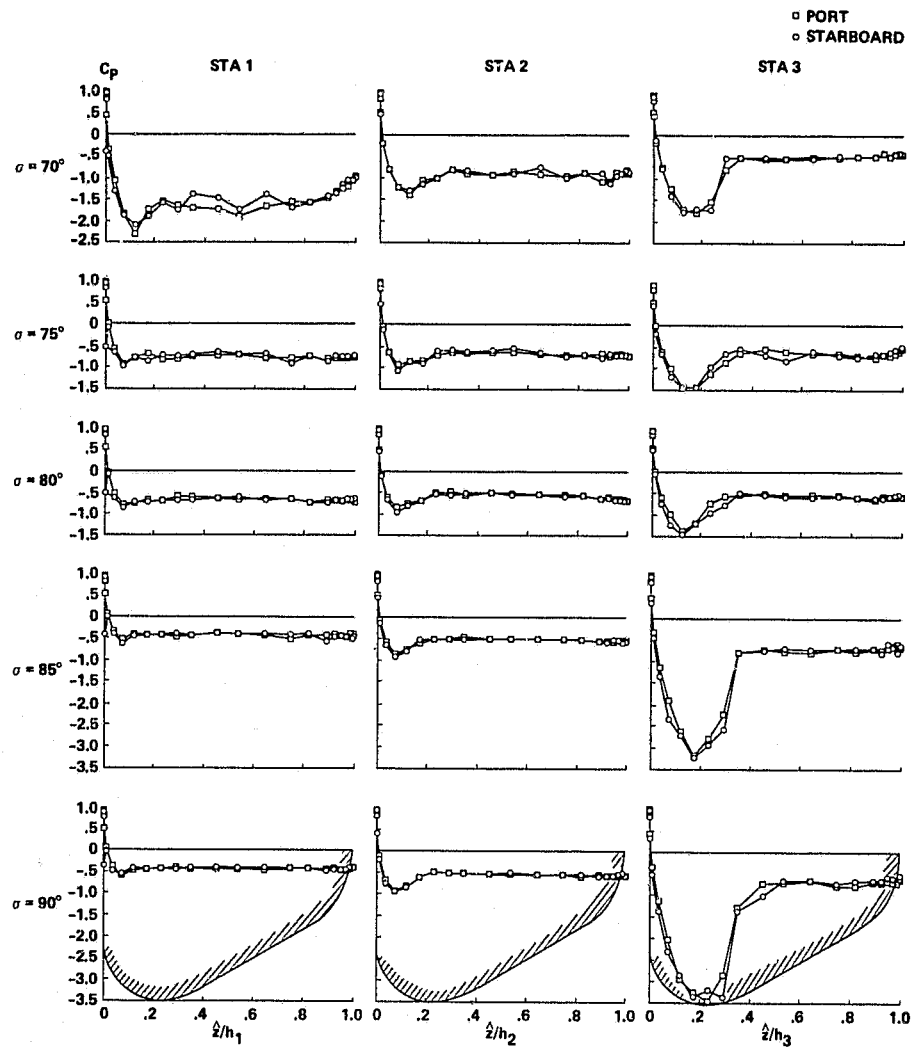
ORIGINAL PAGE IS
OF POOR QUALITY



(a) $\sigma = 45^\circ, 50^\circ, 55^\circ, 60^\circ, \text{ and } 65^\circ$.

Figure 25.- Pressure distribution for blunt triangular cone at various angles of attack: $R_{hb} = 1.1 \times 10^6$, $\psi = 0^\circ$.

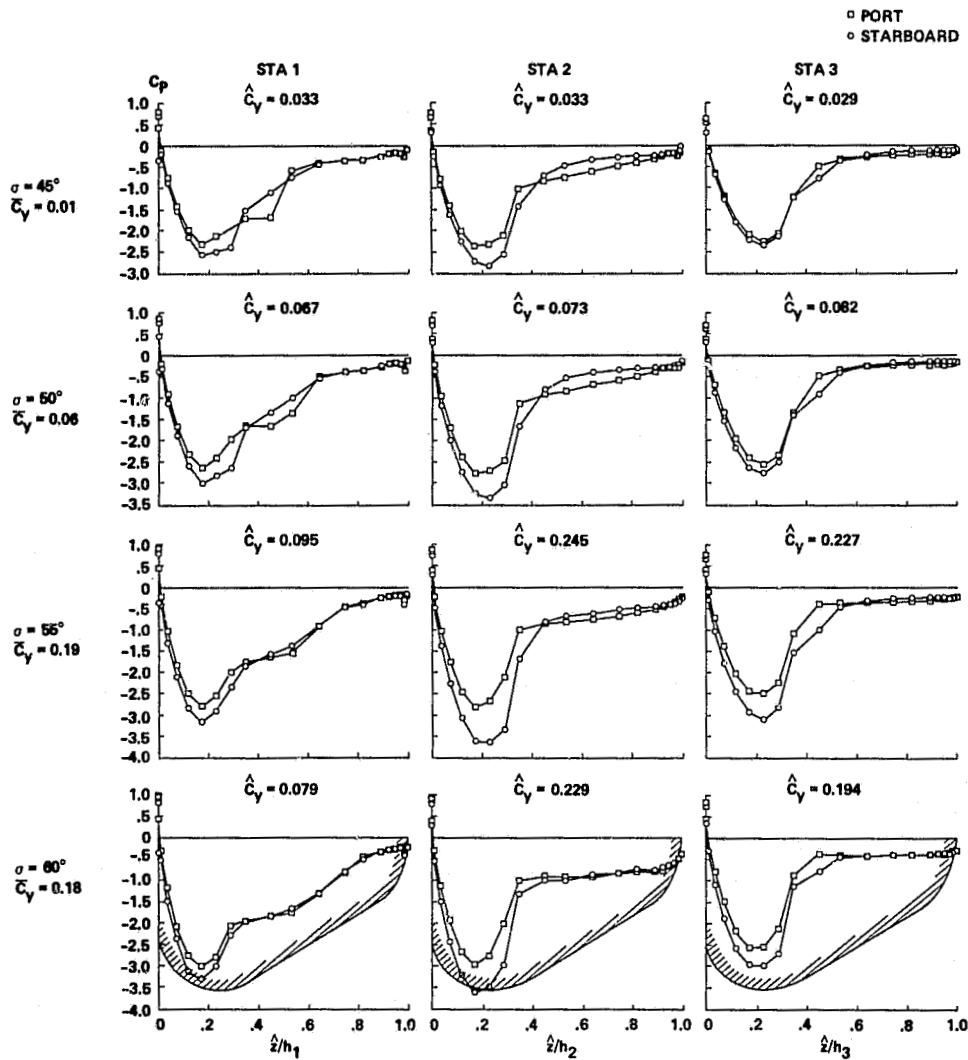
ORIGINAL PAGE IS
OF POOR QUALITY



(b) $\sigma = 70^\circ, 75^\circ, 80^\circ, 85^\circ$, and 90° .

Figure 25.- Concluded.

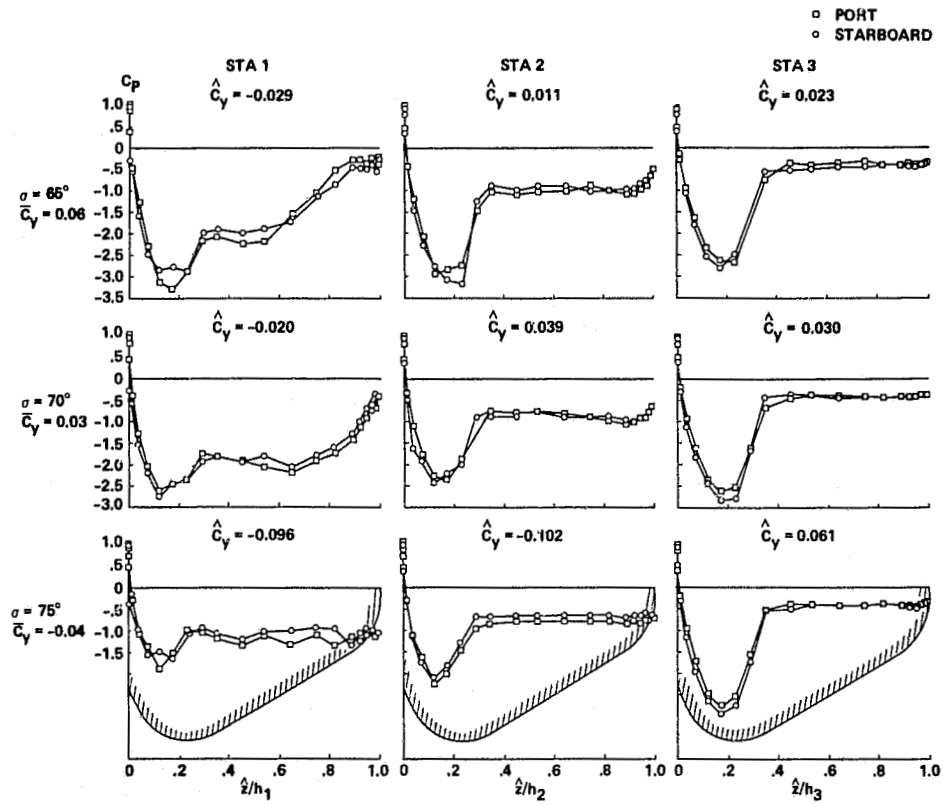
ORIGINAL PAGE IS
OF POOR QUALITY.



(a) $\sigma = 45^\circ, 50^\circ, 55^\circ$, and 60° .

Figure 26.- Pressure distributions for blunt triangular cone at various angles of attack: $R_{hp} = 1.6 \times 10^6$, $\psi = 0^\circ$.

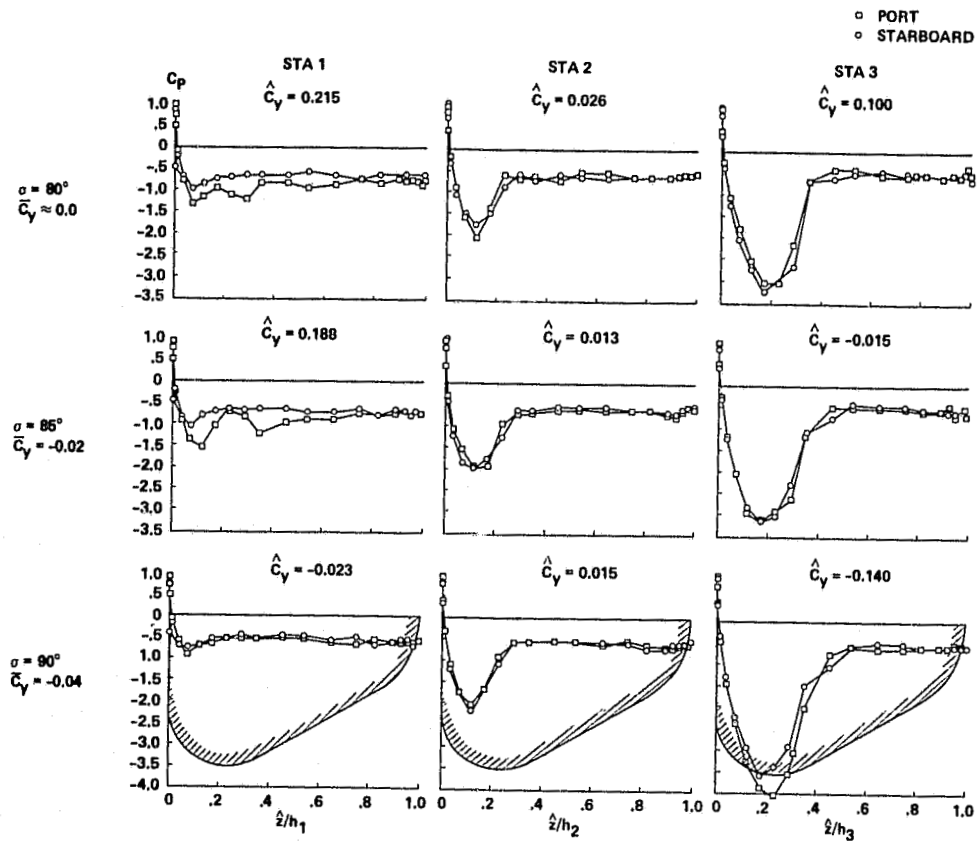
ORIGINAL PAGE IS
OF POOR QUALITY



(b) $\sigma = 65^\circ$, 70° , and 75° .

Figure 26.- Continued.

ORIGINAL PAGE 13
OF POOR QUALITY



(c) $\sigma = 80^\circ$, 85° , and 90° .

Figure 26.- Concluded.

ORIGINAL PAGE IS
OF POOR QUALITY

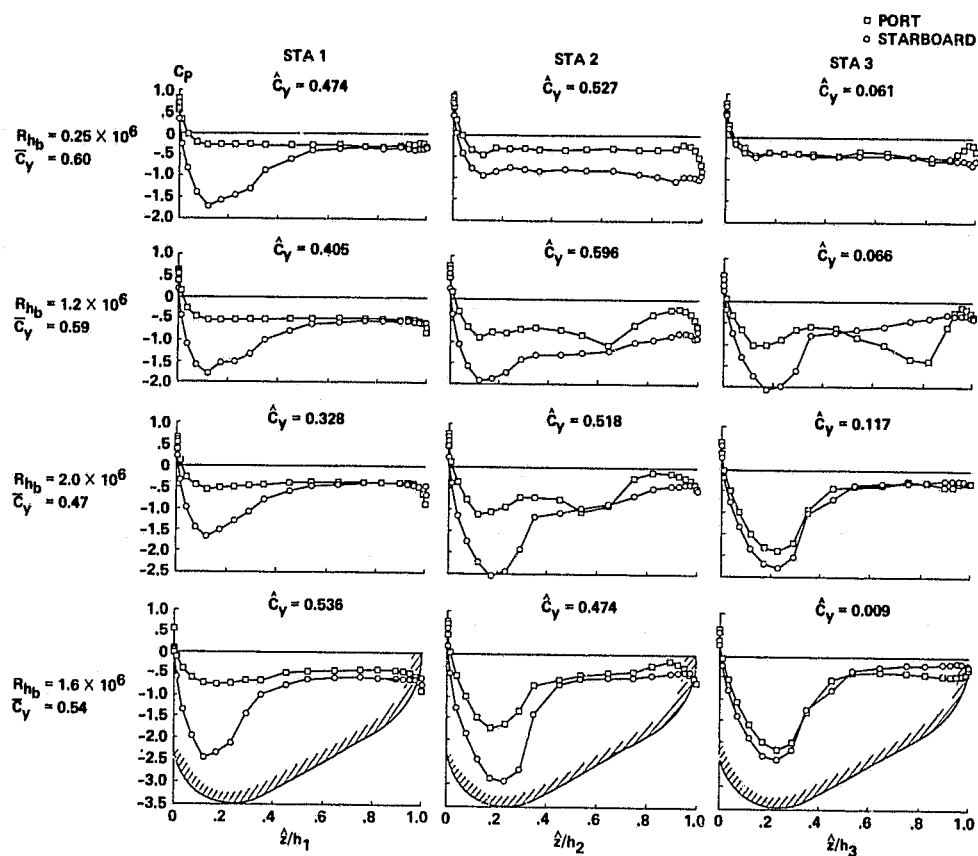


Figure 27.- Pressure distributions for sharp triangular cone at various Reynolds numbers: $\sigma = 45^\circ$, $\psi = 0^\circ$.

ORIGINAL PAGE IS
OF POOR QUALITY

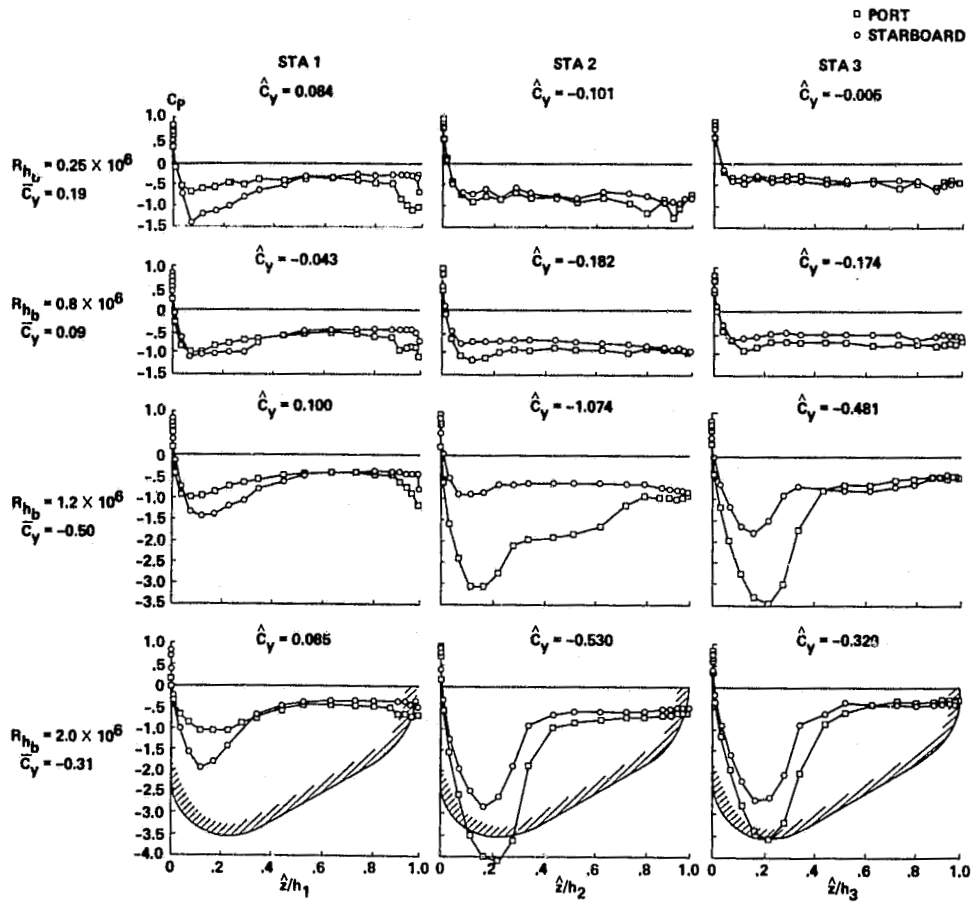


Figure 28.- Pressure distributions for sharp triangular cone at various Reynolds numbers: $\sigma = 60^\circ$, $\psi = 0^\circ$.

ORIGINAL PAGE IS
OF POOR QUALITY

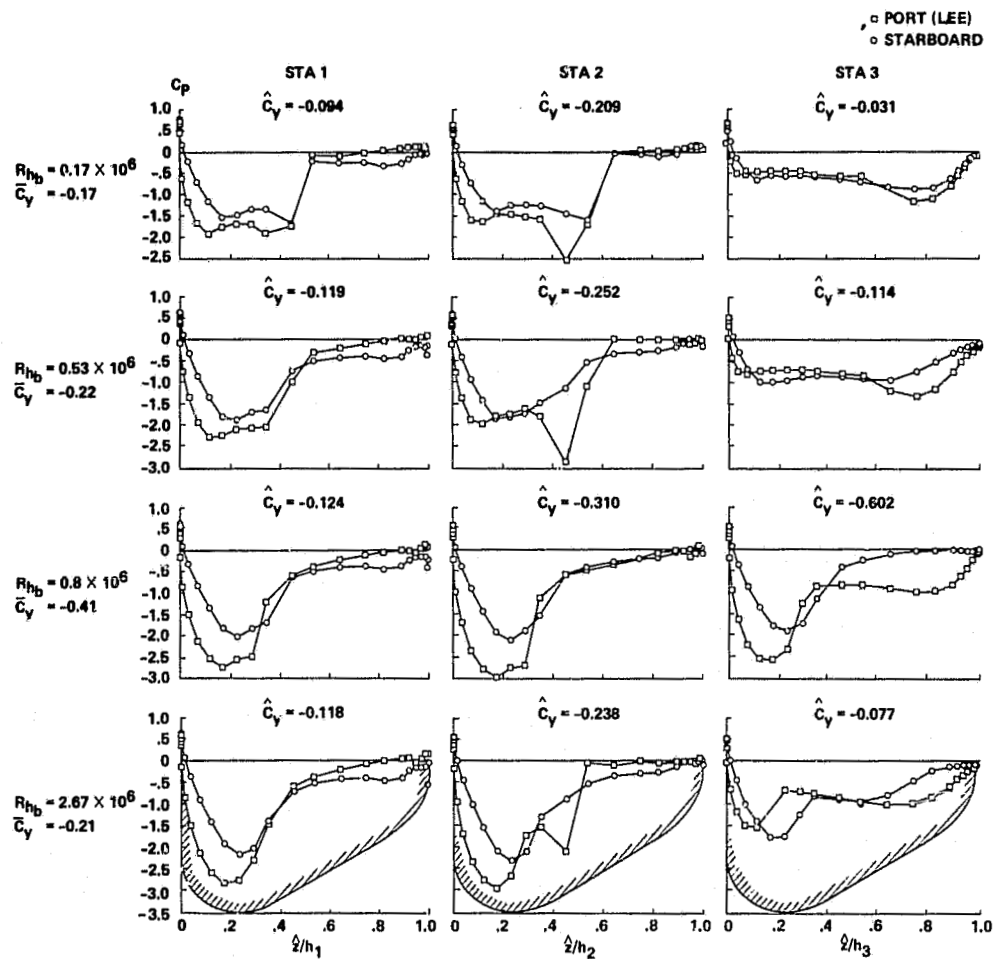


Figure 29.- Pressure distributions for triangular cylinder at various Reynolds numbers: $\sigma = 45^\circ$, $\psi = 10^\circ$.

ORIGINAL PAGE IS
OF POOR QUALITY

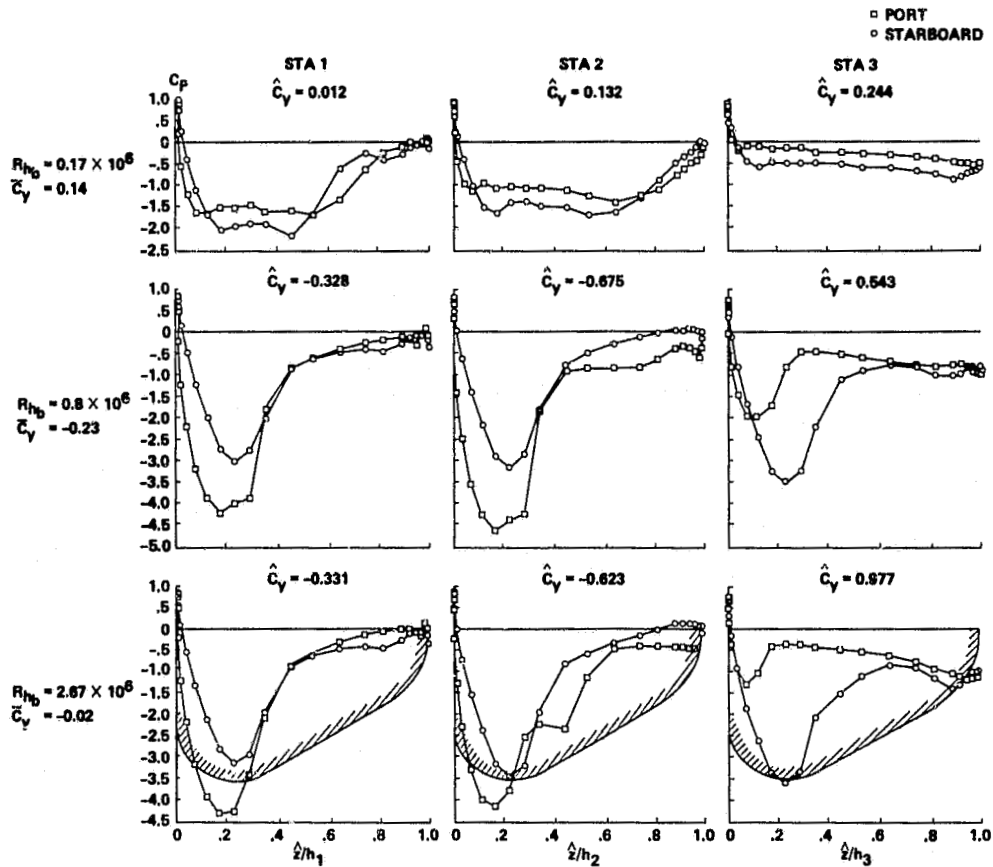


Figure 30.- Pressure distribution for triangular cylinder at various Reynolds numbers: $\sigma = 60^\circ$, $\psi = 10^\circ$.

ORIGINAL PAGE IS
OF POOR QUALITY

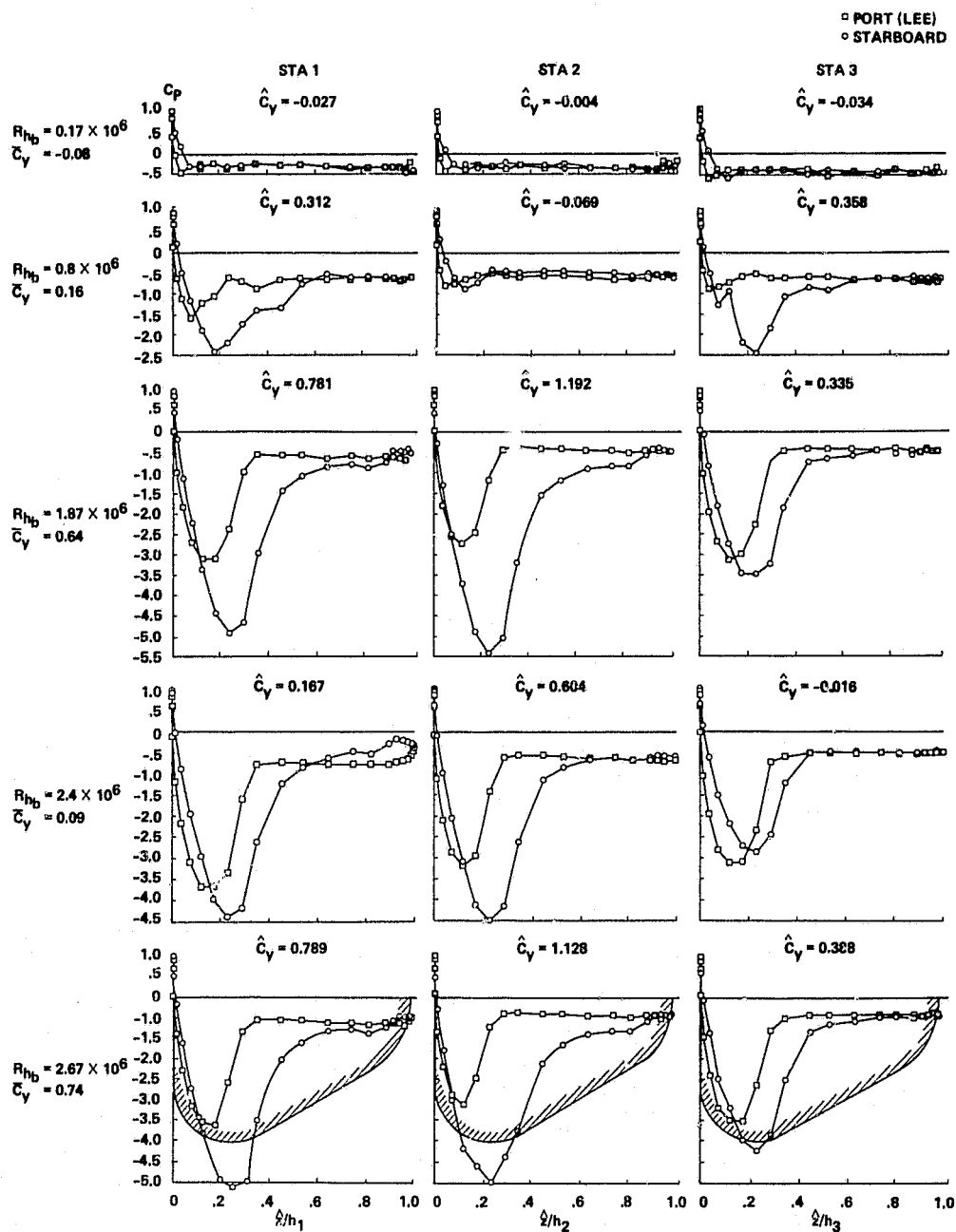


Figure 31.- Pressure distributions for triangular cylinder at various Reynolds numbers: $\sigma = 90^\circ$, $\psi = 10^\circ$.

ORIGINAL PAGE IS
OF POOR QUALITY

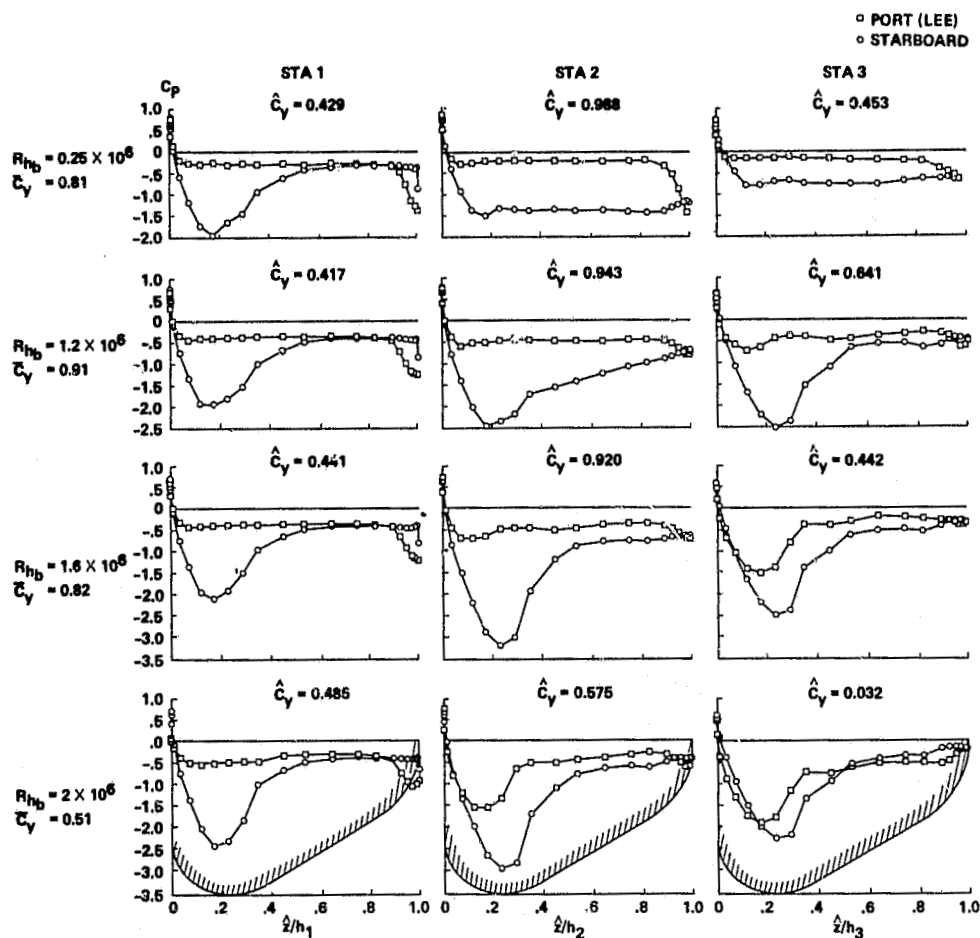


Figure 32.- Pressure distributions for sharp triangular cone at various Reynolds numbers: $\sigma = 45^\circ$, $\psi = 10^\circ$.

ORIGINAL PAGE IS
OF POOR QUALITY

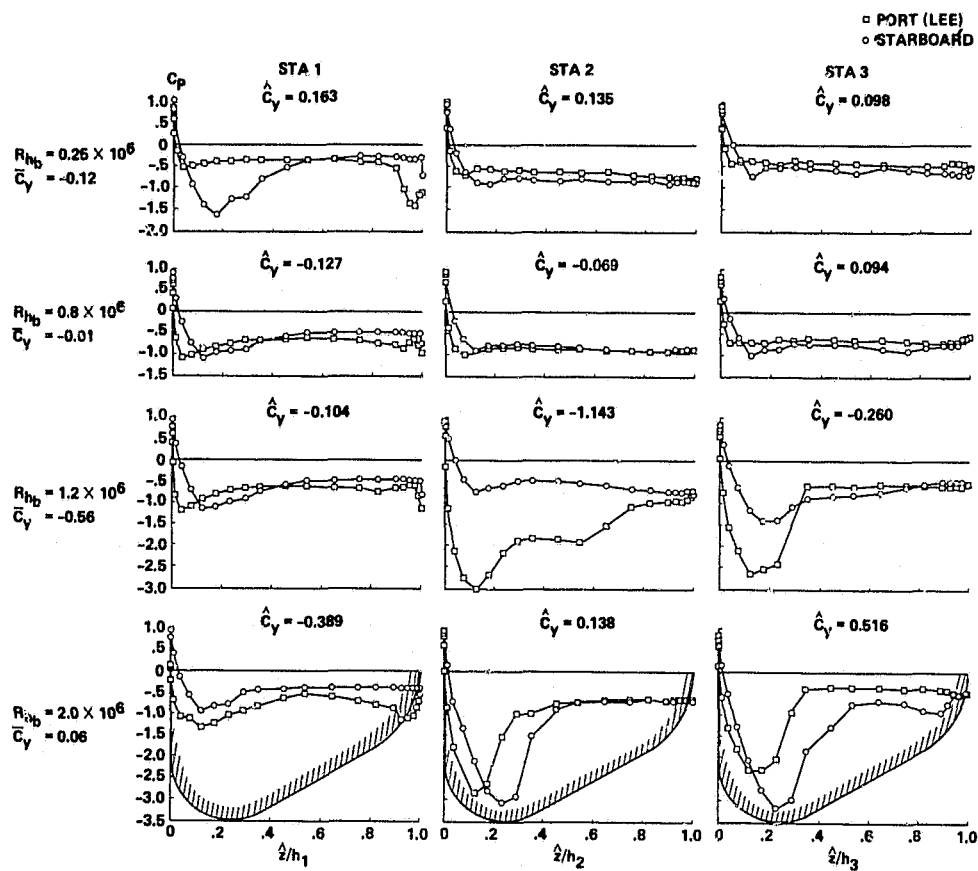


Figure 33.- Pressure distributions for sharp triangular cone at various Reynolds numbers: $\sigma = 60^\circ$, $\psi = 10^\circ$.

ORIGINAL PAGE IS
OF POOR QUALITY

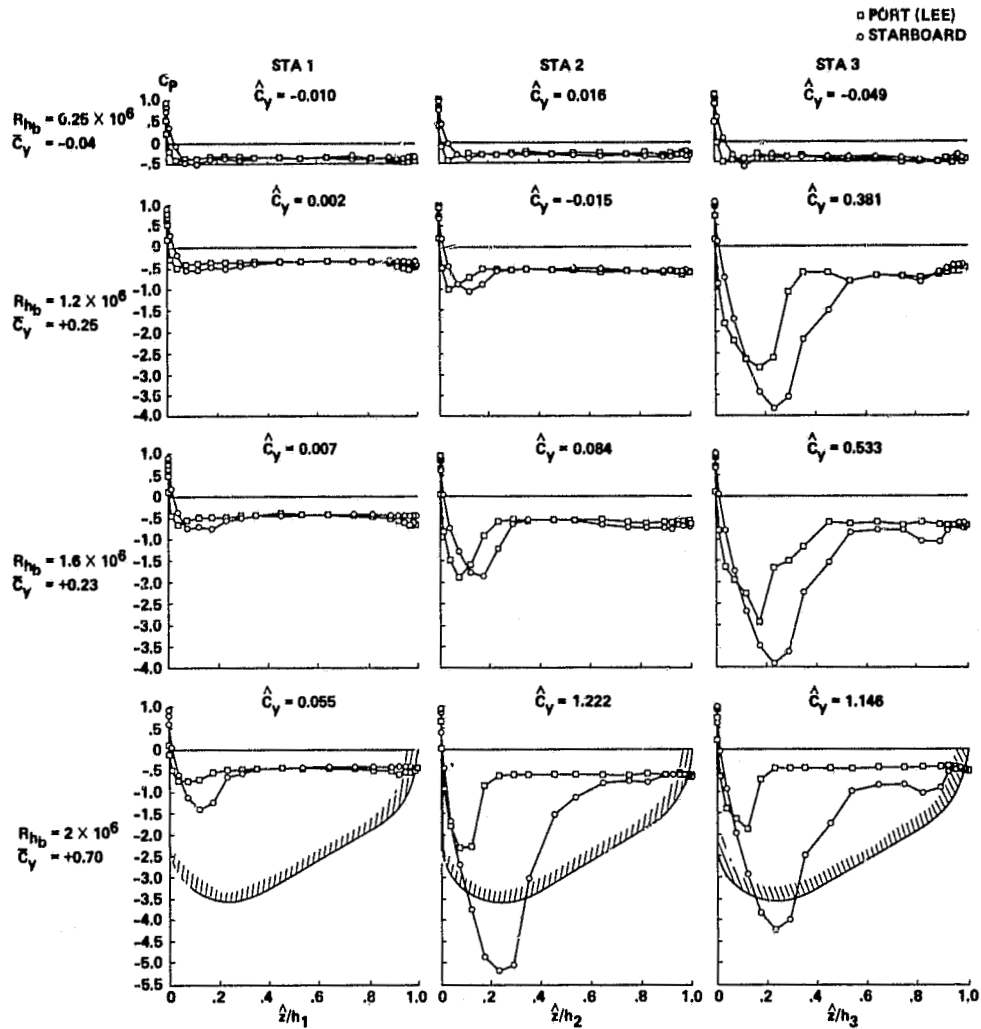


Figure 34.- Pressure distributions for sharp triangular cone at various Reynolds numbers: $\sigma = 90^\circ$, $\psi = 10^\circ$.

ORIGINAL PAGE IS
OF POOR QUALITY

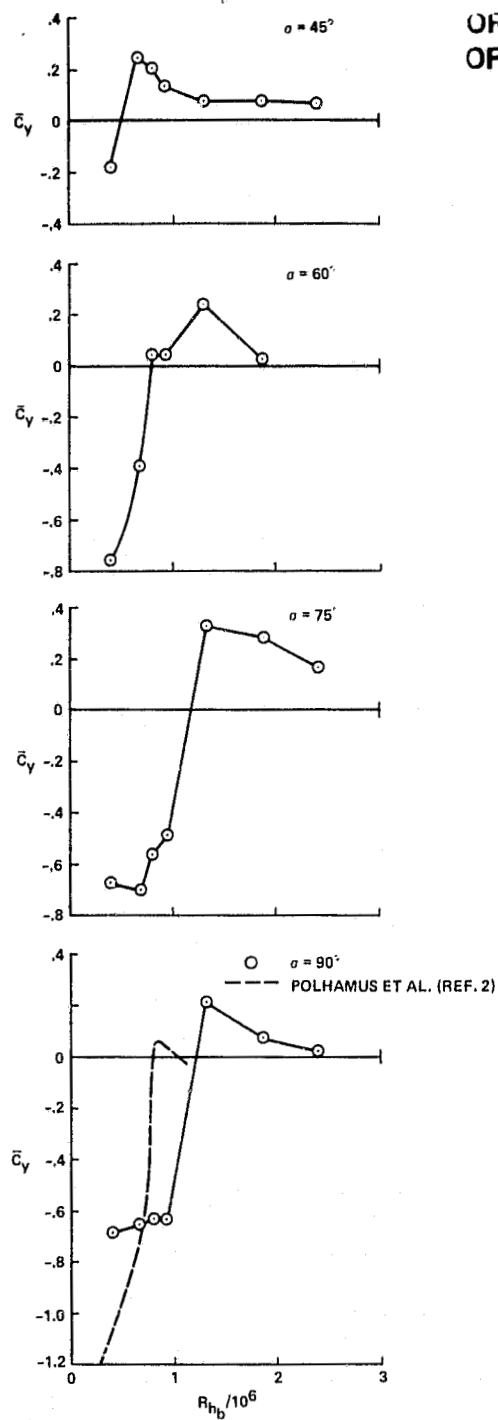


Figure 35.- Cross-flow coefficients for inverted triangular cylinder: $\psi = 10^\circ$.

ORIGINAL PAGE IS
OF POOR QUALITY

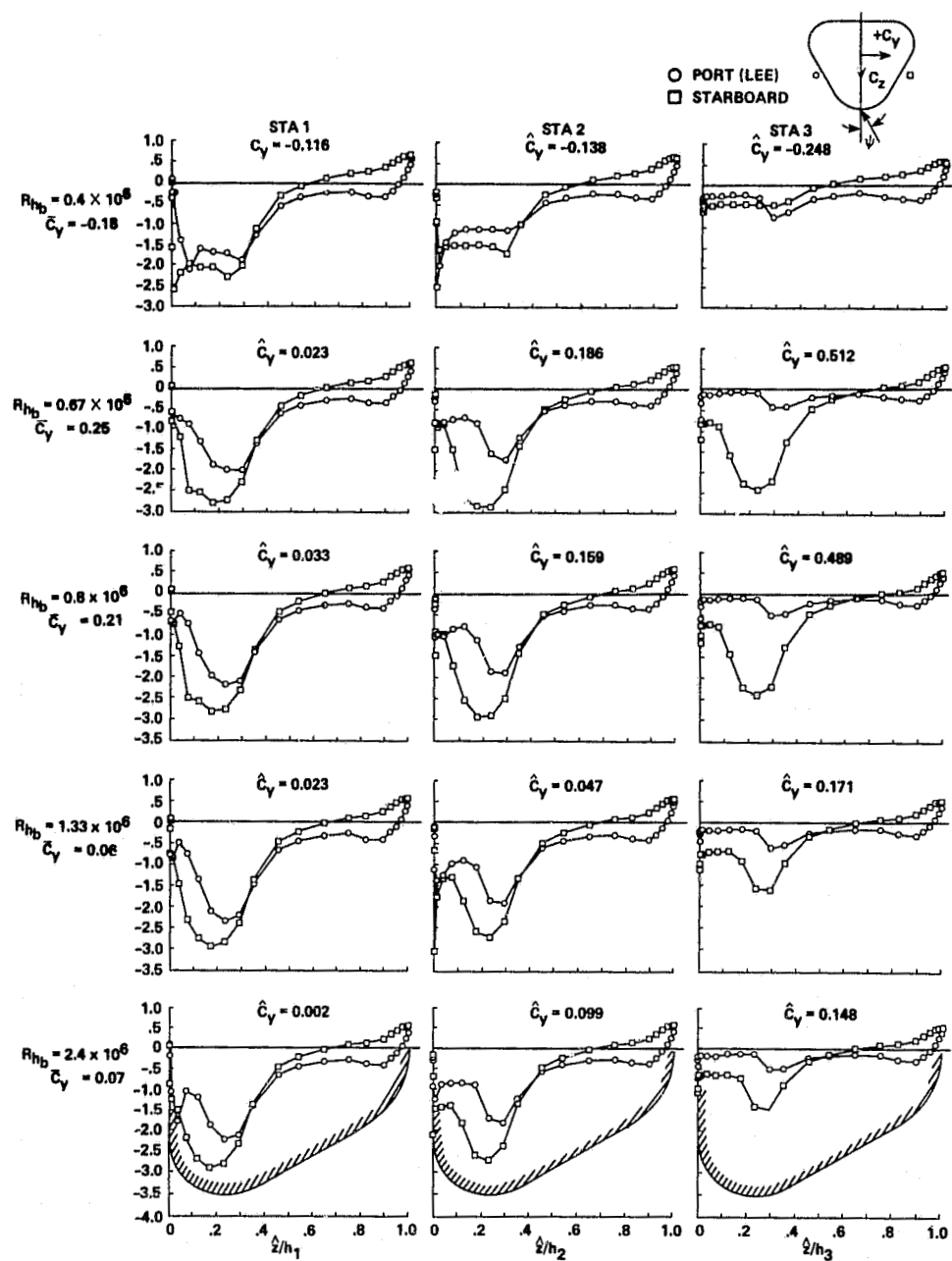


Figure 36.- Pressure distributions for the inverted triangular cylinder at various Reynolds numbers: $\sigma = 45^\circ$, $\psi = 10^\circ$.

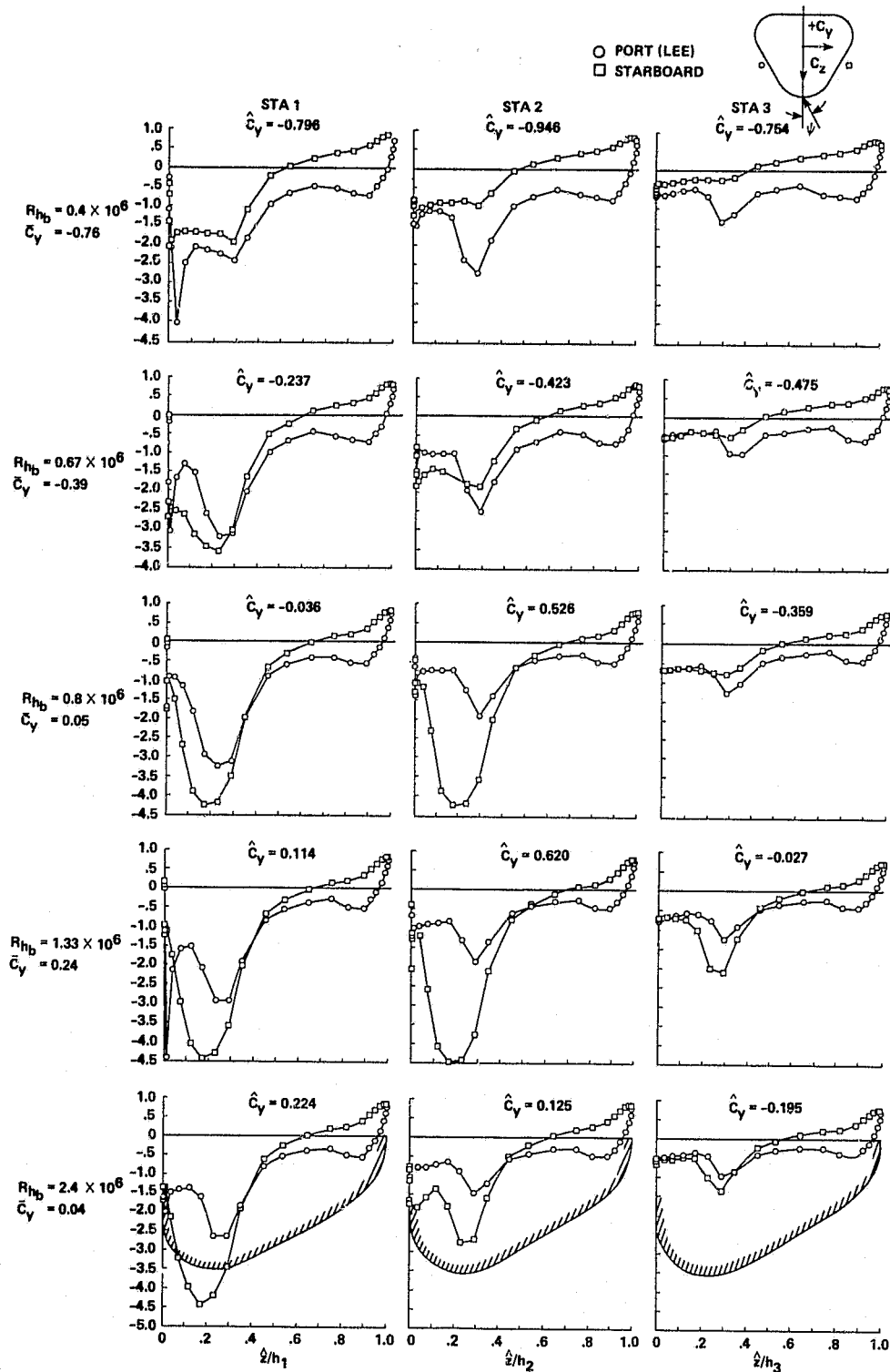


Figure 37.- Pressure distributions for the inverted triangular cylinder at various Reynolds numbers: $\sigma = 60^\circ$, $\psi = 10^\circ$.

ORIGINAL PAGE IS
OF POOR QUALITY

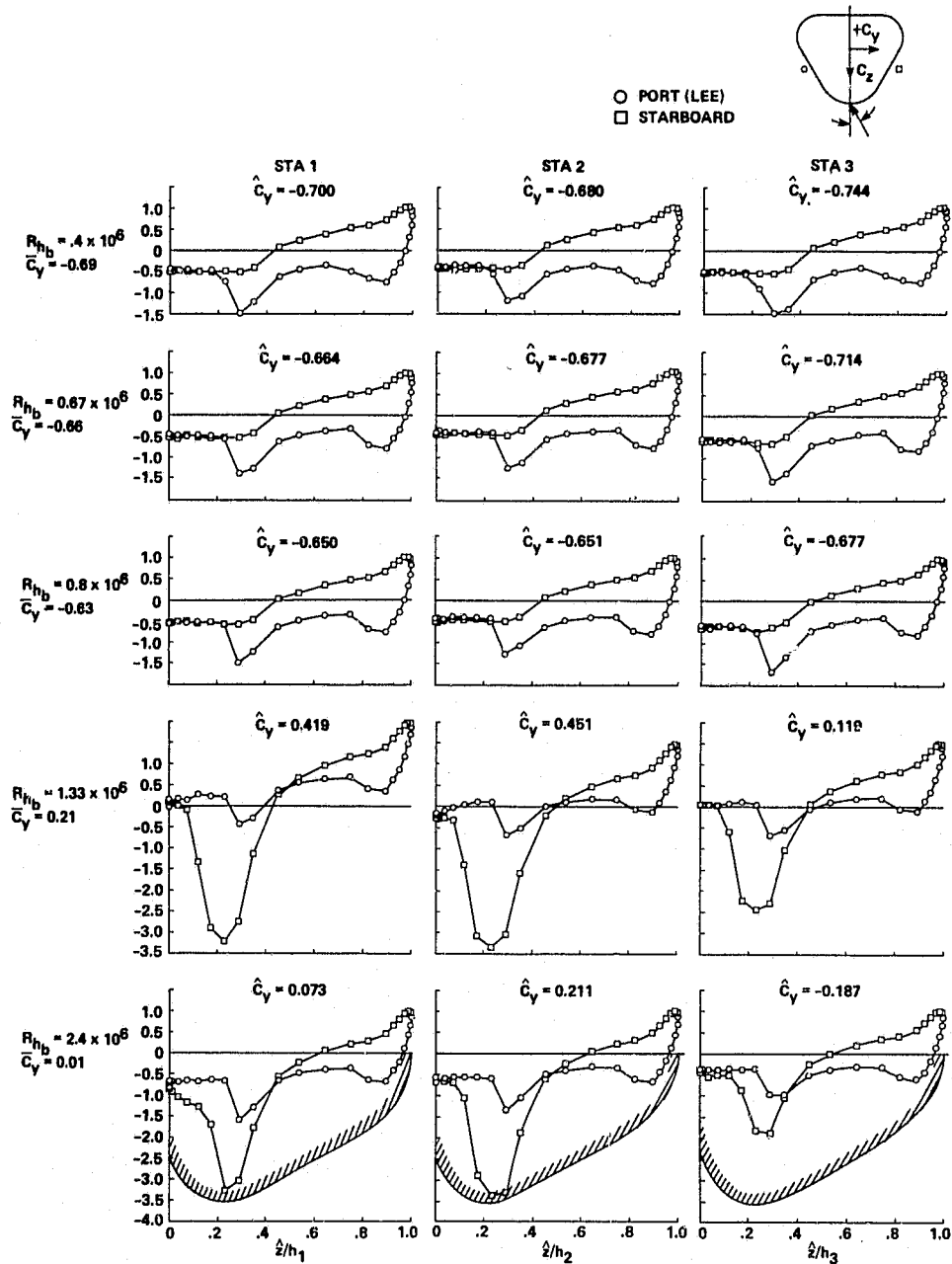


Figure 38.- Pressure distributions for the inverted cylinder at various Reynolds numbers: $\sigma = 90^\circ$, $\psi = 10^\circ$.

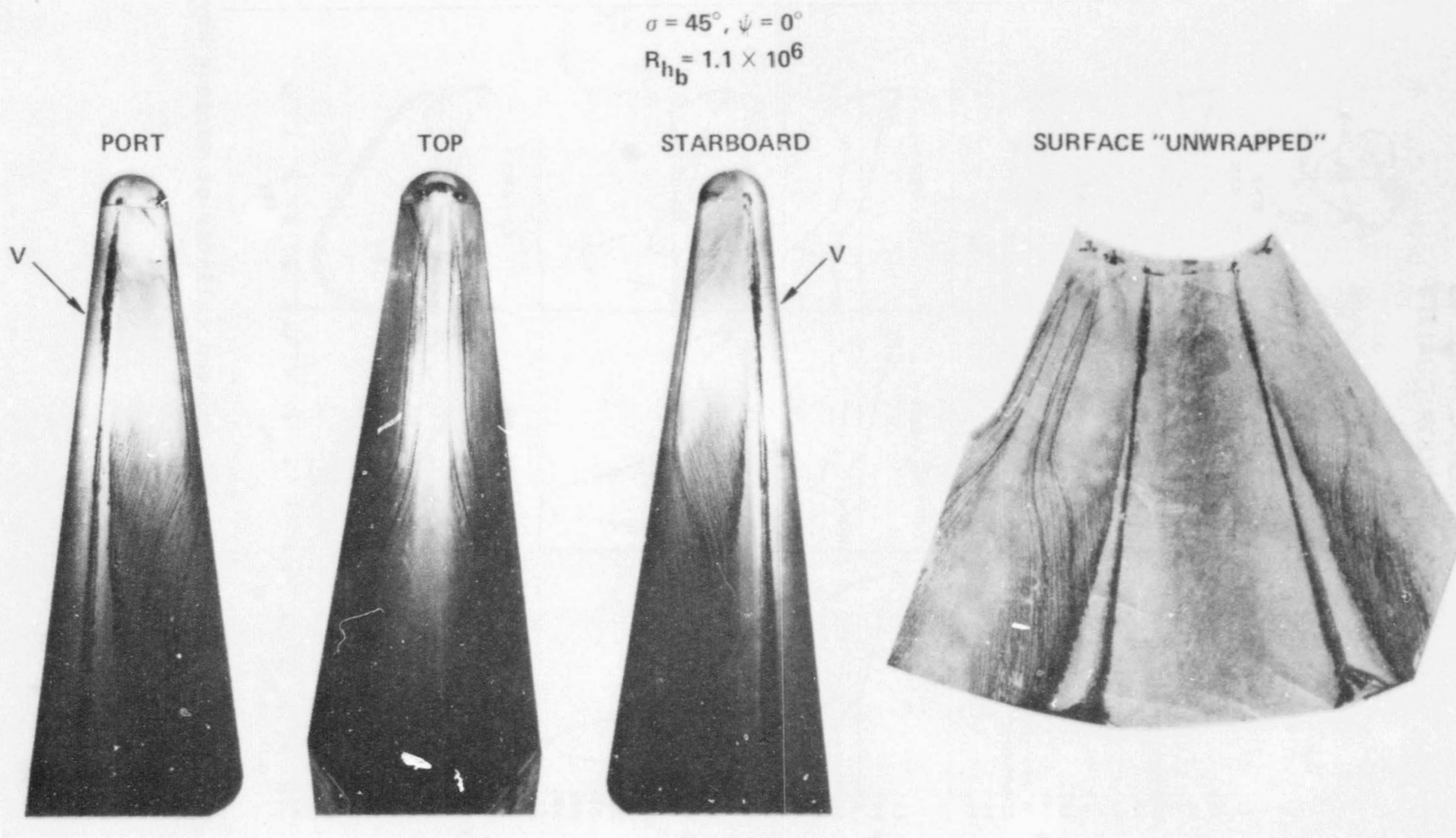


Figure 39.- Surface oil-flow on the blunt triangular cone: $\sigma = 45^\circ, \psi = 0^\circ, R_{hb} = 1.1 \times 10^6$.

$$\sigma = 45^\circ, \psi = 0^\circ$$

$$R_{hb} = 1.1 \times 10^6$$

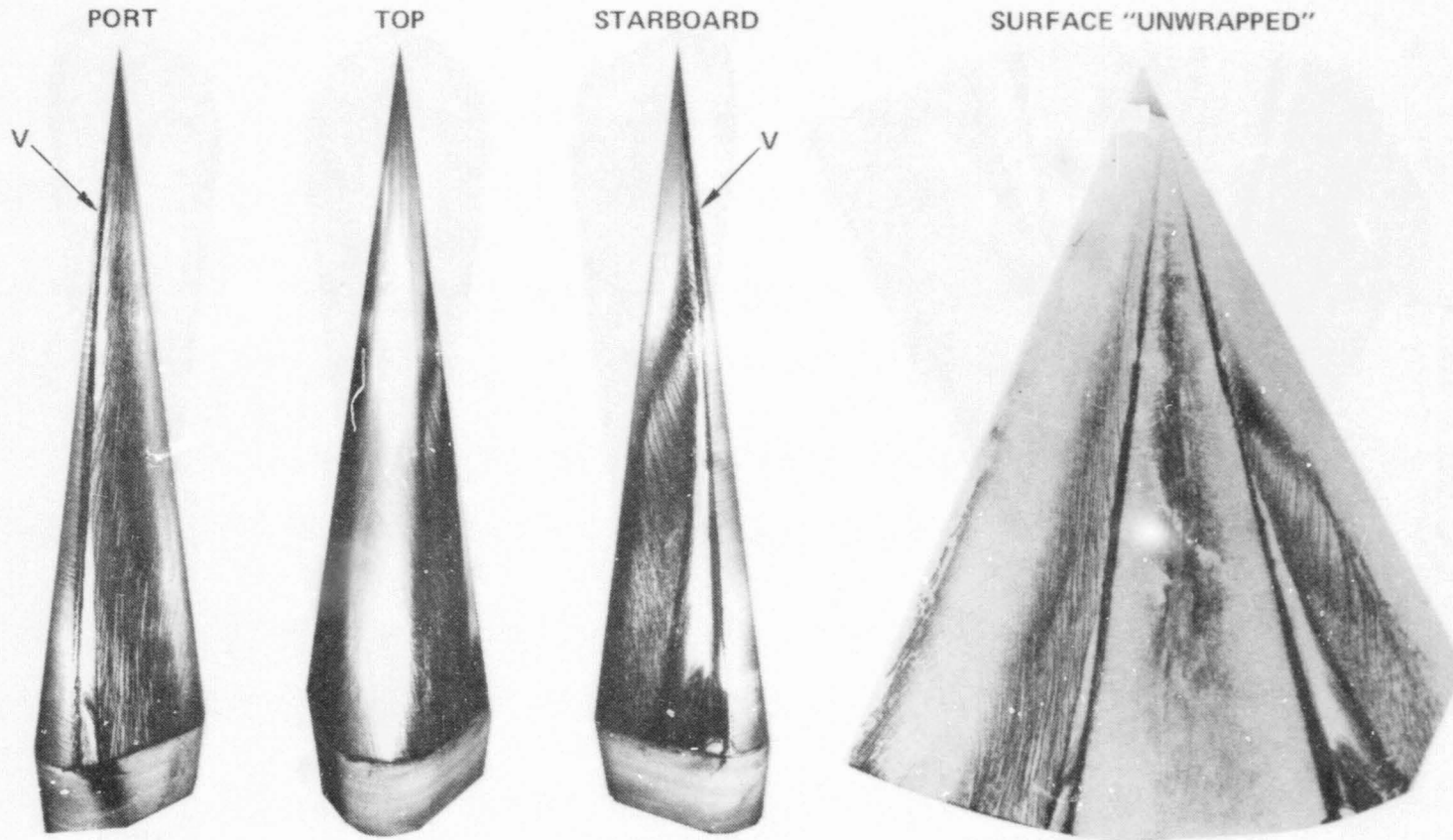


Figure 40.- surface oil-flow on the sharp triangular cone: $\sigma = 45^\circ, \psi = 0^\circ, R_{hb} = 1.1 \times 10^6$.

$$\sigma = 60^\circ, \psi = 0^\circ$$

$$R_{hb} = 1.1 \times 10^6$$

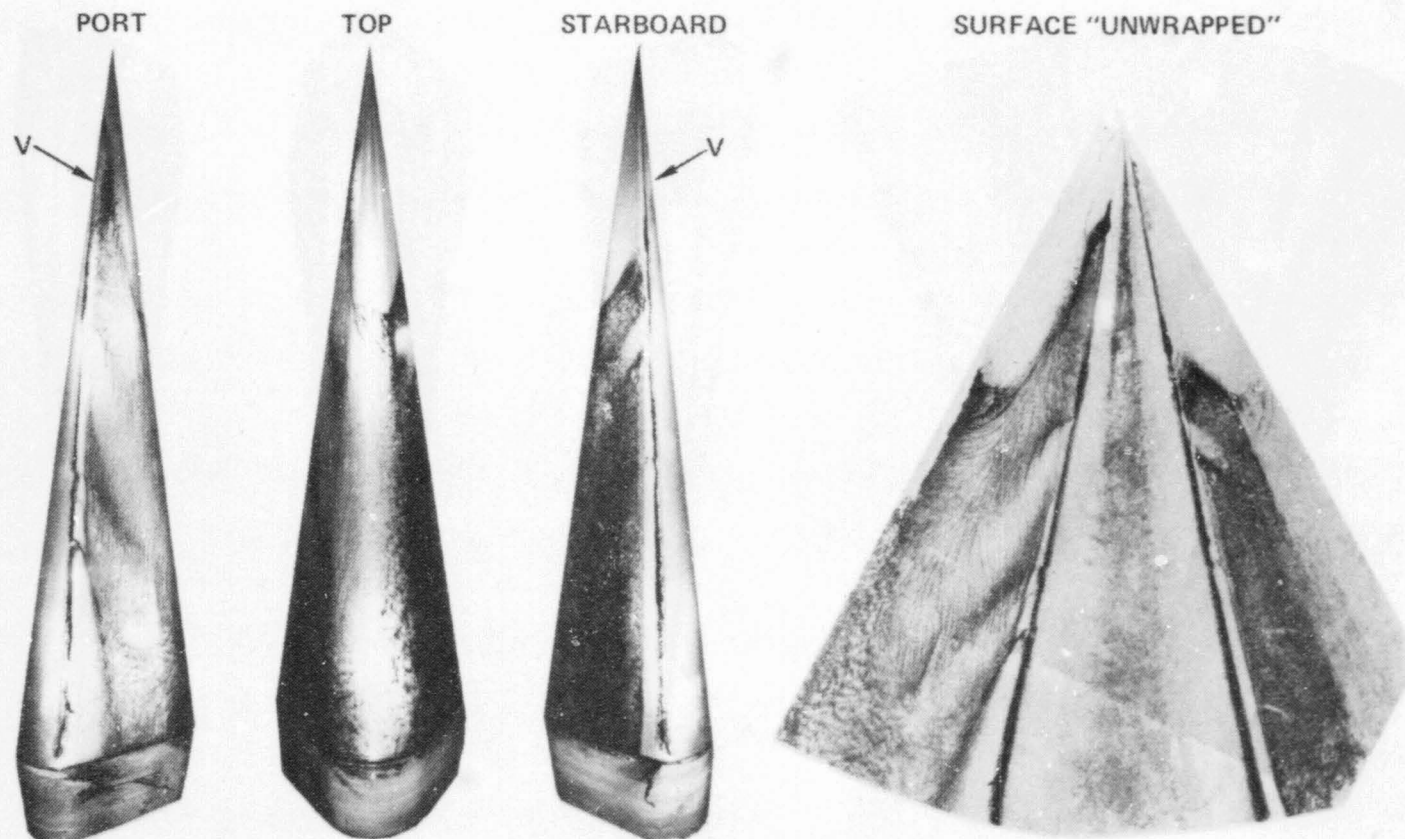


Figure 41.- Surface oil-flow on the sharp triangular cone: $\sigma = 60^\circ$, $\psi = 0^\circ$, $R_{hb} = 1.1 \times 10^6$.

ORIGINAL PAGE IS
OF POOR QUALITY